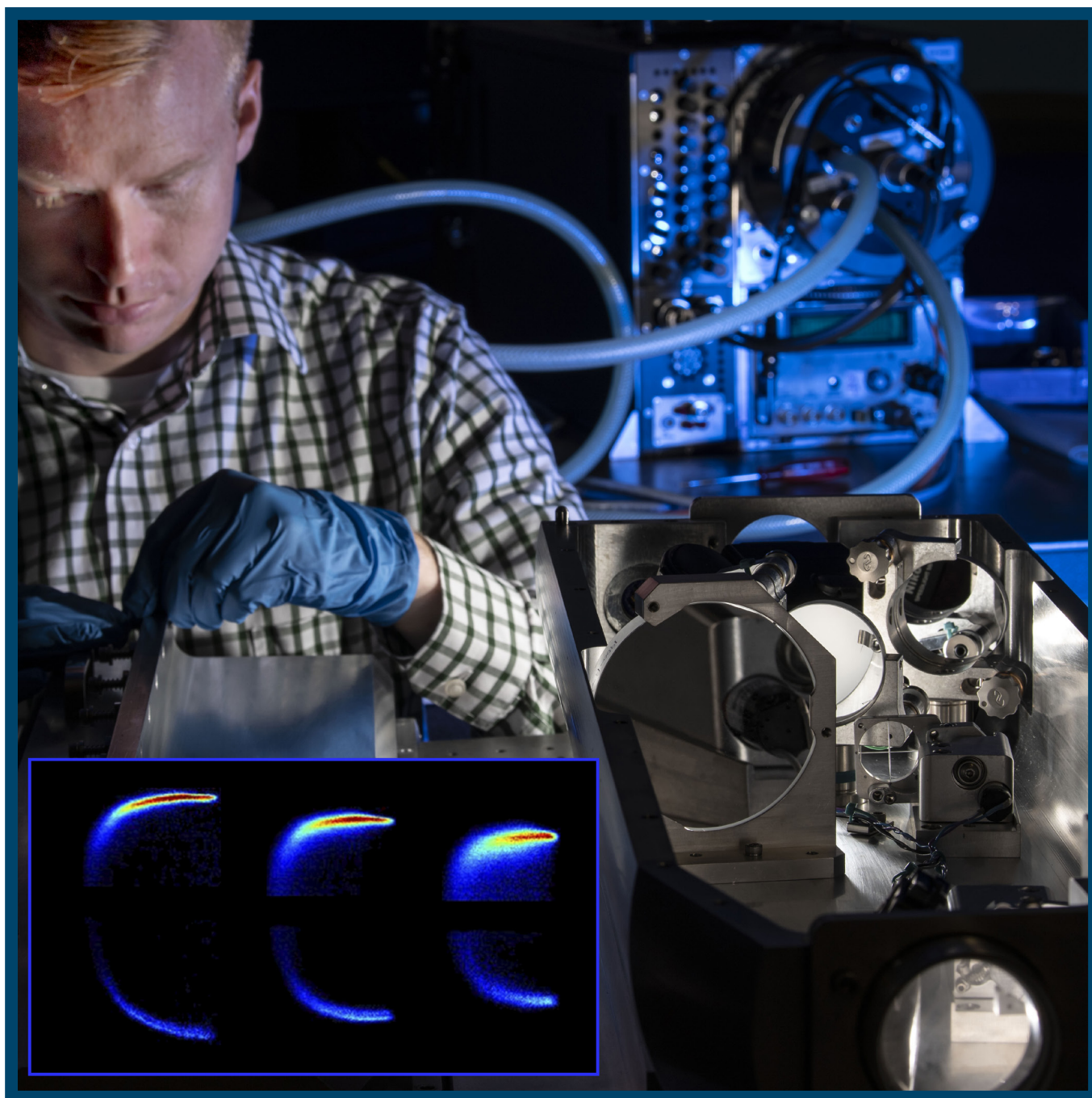


# LLE Review

## Quarterly Report



## About the Cover:

The photo on the cover shows Horton Graduate Student Fellow Robert Henchen aligning the all-reflective imaging Thomson-scattering telescope (lower right). The Schwarzschild objective (shown near the middle of the front cover) images scattered light from an OMEGA ten-inch manipulator to a Pfund objective to provide diffraction-limited imaging across all reflected wavelengths (190 nm to 700 nm). In his thesis work, the system collected light scattered from electron plasma waves, which were spectrally and temporally resolved using a ROSS streak camera (top right). The three streaked images (bottom left) show the collective Thomson-scattering spectrum from three locations in the plasma. The wavelength separation between the electron plasma wave features provides a measurement of the electron density, while their width provides a measurement of the electron temperature. In the novel work conducted by Mr. Henchen, the relative amplitudes of these spectrum were used to measure the heat flux in the plasma and to make the first direct measurements of nonlocal thermal transport.

The photograph on the right shows Mechanical Engineering graduate student Robert Henchen. Mr. Henchen is currently preparing to defend his Ph.D. thesis, "Direct Measurements of Nonlocal Heat Flux in Laser-Produced Coronal Plasmas using Thomson Scattering from Electron-Plasma Waves."



This report was prepared as an account of work conducted by the Laboratory for Laser Energetics and sponsored by New York State Energy Research and Development Authority, the University of Rochester, the U.S. Department of Energy, and other agencies. Neither the above named sponsors nor any of their employees makes any warranty, expressed or implied, or assumes any legal liability or responsibility for the accuracy, completeness, or usefulness of any information, apparatus, product, or process disclosed, or represents that its use would not infringe privately owned rights. Reference herein to any specific commercial product, process, or service by trade name, mark, manufacturer, or otherwise, does not necessarily constitute or imply its endorsement, recommendation, or favoring by the United States Government or any agency thereof or any other sponsor. Results reported in the LLE Review should not be taken as necessarily final results as they represent active research. The

views and opinions of authors expressed herein do not necessarily state or reflect those of any of the above sponsoring entities.

The work described in this volume includes current research at the Laboratory for Laser Energetics, which is supported by New York State Energy Research and Development Authority, the University of Rochester, the U.S. Department of Energy Office of Inertial Confinement Fusion under Cooperative Agreement No. DE-NA0001944, and other agencies.

For questions or comments, contact Seung-Whan Bahk, Editor, Laboratory for Laser Energetics, 250 East River Road, Rochester, NY 14623-1299, (585) 273-4023.

Worldwide-Web Home Page: <http://www.lle.rochester.edu/>

Printed in the United States of America

Available from

National Technical Information Services  
U.S. Department of Commerce  
5285 Port Royal Road  
Springfield, VA 22161  
[www.ntis.gov](http://www.ntis.gov)

# LLE Review

## Quarterly Report



### Contents

In Brief .....	iii
Observation of Nonlocal Heat Flux Using Thomson Scattering.....	125
Ray-Based Modeling of Cross-Beam Energy Transfer at Caustics .....	131
Tritium Retention in Hexavalent Chromate-Conversion-Coated Aluminum Alloy .....	138
Simulation of Grating-Compressor Misalignment Tolerances and Mitigation Strategies for Chirped-Pulse-Amplification Systems of Varying Bandwidth and Beam Size.....	143
A Rate-Doubled 10-GHz Fiducial Comb Generator for Precision Optical Timing Calibration .....	154
Investigation of Laser-Induced Damage in Hafnia/Silica Multilayer Dielectric Coatings Under 1053-nm, 600-fs to 100-ps Laser Irradiation .....	160
Publications and Conference Presentations	



## In Brief

This volume of the LLE Review, covering April–June 2018, features “Observation of Nonlocal Heat Flux Using Thomson Scattering” by R. J. Henchen, J. Katz, D. Cao, J. P. Palastro, and D. H. Froula (LLE); M. Sherlock (LLNL); and W. Rozmus (University of Alberta). This article (p. 125) reports the first direct measurement of nonlocal heat flux in laser-produced coronal plasma using Thomson scattering. An aluminum coronal plasma produced by six OMEGA beams was probed using Thomson scattering in regions of low- and high-temperature gradients. The measured Thomson-scattering spectra from electron plasma waves were fit with spectra calculated using nonlocal electron distribution functions from Vlasov–Fokker–Planck simulations. The inferred distribution functions are used to calculate the heat flux corresponding to the measurement points in the corona. The heat-flux calculations from both classical and nonlocal distributions agree well far from the target where the temperature gradient is small. However, the measured heat flux in the high-gradient region is reduced from classical theory as much as a factor of 2, indicating nonlocal effects.

Additional research highlights presented in the issue include the following:

- R. K. Follett, J. G. Shaw, V. N. Goncharov, D. H. Edgell, D. H. Froula, and J. P. Palastro (LLE) and J. F. Myatt (University of Alberta) present an improved ray-based modeling technique of cross-beam energy transfer (CBET) at caustics (p. 131). The improvement, caustic gain truncation, is based on truncating the interaction length of incident rays in each cell using the geometrical caustic boundary information. This allows caustics to be treated more accurately and improves energy conservation. The new ray-based CBET calculations show excellent agreement with laser absorption from 2-D wave-based calculations (0.3% difference) and a 3-D 60-beam OMEGA implosion (2.4% difference) without artificial multipliers.
- C. Fagan, M. Sharpe, W. T. Shmayda, W. U. Schroeder discuss the increased tritium retention in a hexavalent chromate-conversion-coated (CCC) aluminum alloy (p. 138). Both CCC and unmodified aluminum samples were exposed to DT gas for 24 h at room temperature to diagnose how these films interact with a tritium environment. After this, samples were treated with either thermal desorption or a surface-stripping technique to measure the quantity of retained tritium. The results show that chromic-acid anodizing of aluminum dramatically increases the total quantity of tritium retained compared to unmodified aluminum. Because of the physical and chemical properties of CCC, these coatings are not suitable for use in tritium environments.
- B. Webb, M. J. Guardalben, C. Dorrer, S. Bucht, and J. Bromage discuss the effect of grating compressor misalignment in a chirped-pulse–amplification laser system (p. 143). The degradation of pulse duration and focal spot size is studied by increasing the grating tip/tilt and in-plane-rotation error. The tolerance analysis was calculated using a *FRED–MATLAB* optical compressor model. The grating-alignment tolerances are investigated for varying beam size, bandwidth, grating geometry, and groove density. Mitigation strategies for the misalignment effects are discussed.

- W. Bittle describes a new rate-doubled 10-GHz fiducial comb generator for precision optical timing calibration applications (p. 154). Solid-state optical comb-pulse generators provide a convenient and accurate method to include timing fiducials. A commercially available vertical-cavity surface-emitting laser (VCSEL) at 680 nm is modulated to 5 GHz and is optically interleaved with itself to generate a 10-GHz comb. The output pulse-to-pulse jitter ratio is low. This self-contained and portable unit will be useful for many optical timing calibration needs, especially for ultrafast streak-camera temporal calibration. Both internal reference frequency generation and external syncing options are available.
- A. A. Kozlov, J. C. Lambropoulos, J. B. Oliver, B. Hoffman, and S. G. Demos identify three different types of damage-site morphology that captures thermomechanical signatures of the energy-release mechanism of laser-heated material under different damage-initiation conditions (p. 160). These are related to whether the damage is defect-driven or intrinsic, the location of the maximum electric-field intensity in the medium, and the laser pulse length. Mechanical or heat-diffusion models are adopted to describe the features of these damage sites. The test was performed on a high-reflecting dielectric coating comprised of  $\text{SiO}_2/\text{HfO}_2$  layers by varying pulsewidth from 0.6 to 100 ps. Nano- to microscale features and the depth of the damaged sites were analyzed using various imaging modalities including atomic force microscopy.

Seung-Whan Bahk  
*Editor*

# Observation of Nonlocal Heat Flux Using Thomson Scattering

In diverse fields of plasma physics including astrophysics, inertial confinement fusion, and magnetohydrodynamics, classical thermal transport<sup>1,2</sup> provides the foundation for calculating heat flux.<sup>3–7</sup> The classical theories of thermal transport by Spitzer–Härm (SH)<sup>1</sup> and Braginskii<sup>2</sup> specify the heat flux by a local expression in terms of the thermal conductivity  $\kappa$  and the electron temperature gradient (e.g.,  $\mathbf{q}_{SH} = \kappa \nabla T_e$ ). This theory breaks down in the presence of large temperature gradients,<sup>8–11</sup> turbulence,<sup>12</sup> or return current instabilities:<sup>13–16</sup> classical theory does not include nonlocal effects where energetic electrons travel distances comparable with the temperature scale length before colliding.

Local thermal-transport theories<sup>1,2</sup> follow from a perturbative solution of a kinetic equation in terms of the collision parameter  $\lambda_{ei}/L_T \ll 1$ , where  $\lambda_{ei}$  is the electron–ion (e–i) mean free path and  $L_T = |\nabla \ln(T_e)|^{-1}$  is the scale length of the temperature gradient. Nonlocal theories overcome limitations of classical theory by accounting for the range of electron–ion mean free paths associated with different electron velocities. By extending closure relations for hydrodynamic models into the kinetic regime of weak collisions, these theories<sup>17–24</sup> have established the limits of classical transport ( $\lambda_{ei}/L_T \sim 10^{-2}$ ).

In laser-produced plasmas, classical theory predicts unphysically large thermal transport. Hydrodynamic simulations of these plasmas require an *ad hoc* limiter on the heat flux to match experimental observables. Historically these limiters were set by kinetic simulations,<sup>25–27</sup> integrated experiments,<sup>10,11,28,29</sup> or more-focused Thomson-scattering measurements of the local plasma conditions (i.e., electron temperature and density).<sup>8,13,30,31</sup> More recently, the nonlocal Schurtz–Nicolai–Busquet (SNB) model<sup>23</sup> was introduced as a computationally efficient method for calculating the nonlocal heat flux in large-scale multidimensional hydrodynamic simulations. Experiments that attempt to measure nonlocal transport have been limited, however, to indirect observations.<sup>8,24,30–32</sup>

In this article, we present the first direct measurement of nonlocal heat flux. A novel implementation of collective Thom-

son scattering measured the heat flux by probing the relative spectral amplitudes of electron plasma waves (Fig. 155.1). In addition to the heat flux, the plasma-wave spectrum provided a measurement of the plasma temperature and density profiles. The profiles were used to calculate the classical SH heat flux, which was in good agreement with the measured heat flux far from the target, where the temperature scale length was

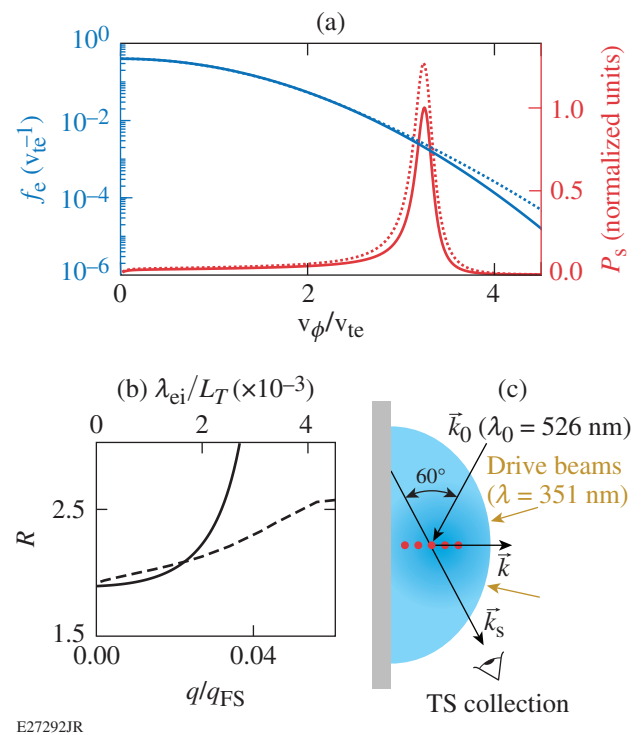


Figure 155.1 (a) Calculated Thomson-scattering (TS) features (red curves, right axis) from electron plasma waves [Eq. (1)] are shown ( $v_{\phi} = \omega/k$ ) using a Maxwellian (solid blue curve, left axis) electron distribution function and the non-Maxwellian (dotted blue curve) distribution that accounts for classical Spitzer–Härm (SH) heat flux ( $\lambda_{ei}/L_T = 2.2 \times 10^{-3}$ ,  $q/q_{FS} = 3\%$ ). (b) For a fixed normalized phase velocity, the ratio ( $R$ ) of the peak scattered power of the up- and downshifted features are shown for calculations that use classical SH (solid curve, top axis) and nonlocal (dashed curve, bottom axis) distribution functions over a range of heat flux normalized to the free-streaming flux,  $q_{FS} = n_e T_e v_{te}$ . (c) Schematic of the setup.

longer than the electron-ion mean free path of heat-carrying electrons ( $\lambda_{ei}/L_T \sim 10^{-3}$ ). For steeper gradients, the measured heat flux was up to a factor of 2 smaller than the classical values as a result of nonlocal transport. For the most nonlocal conditions, the SNB model predicted an inhibited heat flux compared with the classical values, but it still overestimated the measured heat flux by  $\sim 40\%$ . In the region where classical SH theory agrees with the measured heat flux, the SNB model overestimates the flux.

Figure 155.1(a) illustrates the effect of heat flux on the collective Thomson-scattering spectrum. Two scattering spectra, calculated with and without SH heat flux, demonstrate the sensitivity of the Thomson-scattering spectrum to the shape of the electron distribution function. The SH distribution function was derived from the lowest-order terms in the perturbative solution of the kinetic equation,  $f_{SH}(\mathbf{v}) = f_0^M(\mathbf{v}) + \cos\theta f(\mathbf{v})$ , where

$$f(\mathbf{v}) = \lambda_{ei}/L_T \sqrt{2/9\pi} (\mathbf{v}/v_{te})^4 (4 - \mathbf{v}^2/2v_{te}^2) f_0^M(\mathbf{v}),$$

$v_{te} = \sqrt{T_e/m_e}$  is the electron thermal velocity,  $f_0^M$  is a Maxwellian velocity distribution function, and  $\theta$  is the angle between electron velocity and the temperature gradient. The Thomson-scattering spectra were calculated in the high-frequency limit where the ion dynamics can be ignored:<sup>33</sup>

$$S(\mathbf{k}, \omega) = \frac{2\pi}{k} \frac{\tilde{f}_e(\omega/k)}{|\varepsilon(\mathbf{k}, \omega)|^2}, \quad (1)$$

where  $\varepsilon(\mathbf{k}, \omega)$  is the longitudinal plasma dielectric function and the probed wave vector (frequency) is the difference between the incident and scattered wave vectors (frequencies),  $\mathbf{k} = \mathbf{k}_i - \mathbf{k}_s$  ( $\omega = \omega_i - \omega_s$ ). The 1-D distribution function  $\tilde{f}_e(\mathbf{v})$  is determined by integrating the full distribution function over velocities perpendicular to the probed wave vector. At the Langmuir wave resonance defined by  $\varepsilon(\mathbf{k}, \omega) = 0$ ,  $\omega(k) = \pm\omega_L(k) + i\gamma_L(k)$ , where, in general, the Landau damping rate  $\gamma_L$  is proportional to

$$\partial \tilde{f}_e / \partial v \Big|_{v=\omega_L/k}$$

and  $\omega_L$  is approximately the resonant frequency for Langmuir fluctuations. The collisionless approximation of  $S(\mathbf{k}, \omega)$  in Eq. (1) is valid for these experiments because the scale of the probed waves ( $\sim 1/k$ ) is small compared to the electron-ion mean free path such that  $k\lambda_{ei} \gg 1$ .

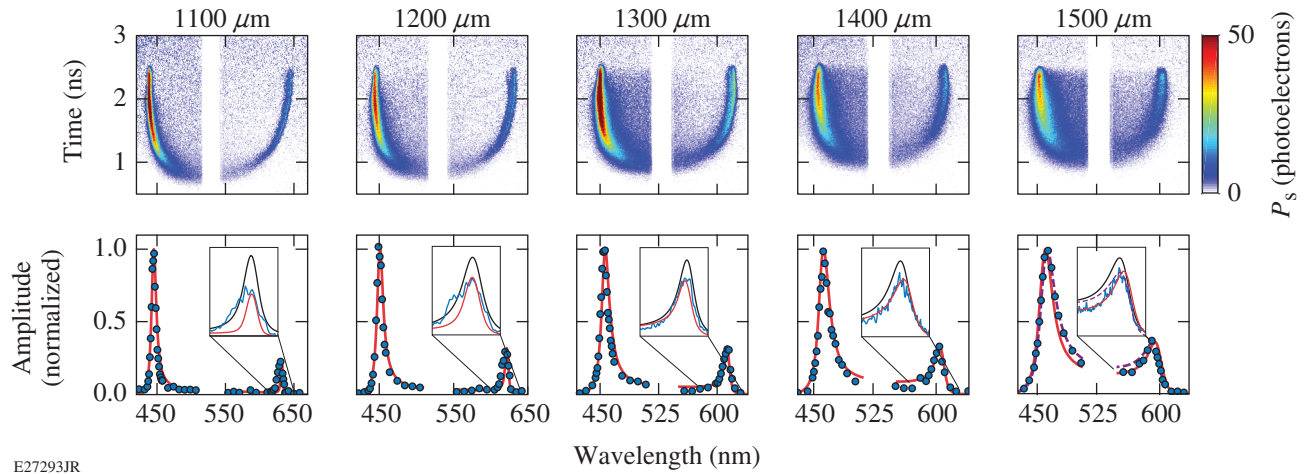
Figure 155.1(b) shows the sensitivity of the amplitude ratio of the up- and downshifted (red- and blue-shifted, respectively) scattered peaks to heat flux, where SH or nonlocal distribution functions were used to calculate the Thomson-scattering spectrum. It is evident from Eq. (1) that heat flux has two effects on the scattered power near the resonance: (1) the amplitude depends on the number of electrons at the resonance [ $\tilde{f}_e(\omega_L/k)$ ] and (2) the width is given by the slope of the electron distribution function at the resonance

$$\partial \tilde{f}_e / \partial v \Big|_{v=\omega_L/k}.$$

Therefore, to maximize the effect of heat flux on the scattered power, the scattering geometry was chosen to probe Langmuir waves propagating along the target normal where the temperature is largest,  $\mathbf{k} \parallel -\nabla T_e$ , and with phase velocities near the region of the electron distribution function with the most heat-carrying electrons,  $\omega_L/k \gtrsim 3.4v_{te}$ . For this geometry, it was demonstrated in theory<sup>34</sup> that the Langmuir fluctuations that contribute to the red-shifted peak in the Thomson-scattering spectrum experience increased Landau damping, while the oppositely propagating Langmuir waves that contribute to blue-shifted peak become less damped.

The experiment was conducted on LLE's OMEGA laser<sup>35</sup> and used six  $\lambda_{3\omega} = 351$ -nm beams to produce a blowoff plasma from a planar aluminum target. Each beam had 250 J in a 2-ns flattop pulse. Phase plates<sup>36</sup> were used to set the profile of the laser spot at the target plane to be a high-order super-Gaussian ( $n = 4.6$ ) with a full width at half maximum of 560  $\mu\text{m}$ . The six beams with the smallest angle of incidence ( $8^\circ$ ,  $29^\circ$ ,  $32^\circ$ ,  $33^\circ$ ,  $35^\circ$ , and  $40^\circ$ ) were chosen to produce the plasma [Fig. 155.1(c)]. The Thomson-scattering diagnostic<sup>37</sup> consisted of a 40-J, 2-ns-long,  $\lambda_{2\omega} = 526.5$ -nm probe beam with a best-focus diameter of  $\sim 50 \mu\text{m}$  (Ref. 38). The light scattered from a  $50\text{-}\mu\text{m} \times 50\text{-}\mu\text{m} \times 50\text{-}\mu\text{m}$  volume was imaged through a 1/3-m spectrometer onto a streak camera. The spectral dispersion was 0.411 nm/pixel  $\pm 0.4\%$ . The system had spectral and temporal resolutions of 0.5 nm  $\pm 5\%$  and 20 ps  $\pm 0.5\%$ , respectively. The scattering angle was  $60^\circ$ . The scattering volume was set to five different locations along the target normal ranging from 1.1 mm to 1.5 mm from the initial target surface. To account for the bremsstrahlung radiation collected by the Thomson-scattering system, a background was established at each location by turning off the Thomson-scattering probe beam and was subtracted from the corresponding spectrum.

Figure 155.2 shows the collective Thomson-scattering spectra measured at each of the probed locations. The data were



E27293JR

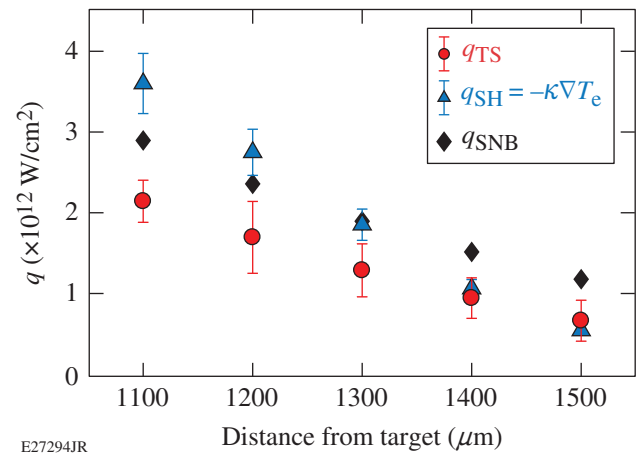
Figure 155.2

The measured collective Thomson-scattering spectra (top row) and the corresponding spectral profiles (blue dots) at 1.5 ns (bottom row). The data were fit (red) with Eq. (1) using non-Maxwellian electron distribution functions to measure heat flux. (Insets) The red-shifted features are shown with calculations (black) that used the plasma conditions from the fit but a Maxwellian electron distribution function. These spectra recover the location of the scattering features but fail to match their amplitudes. At 1.5 mm, the spectrum was fit (dashed curve) with calculations that use a distribution function consistent with classical SH theory. All spectra are normalized to the peak scattered power.

fit with a fully kinetic Thomson-scattered power spectrum<sup>33</sup> that incorporates a non-Maxwellian electron distribution function to provide a measure of the heat flux, electron temperature, and density.<sup>34</sup> To a good approximation, the relative amplitudes of the electron plasma wave features are given by heat flux, the frequency of the electron plasma wave feature by the density, and the width of the plasma wave feature by the electron temperature.

The insets in Fig. 155.2 compare scattered spectra calculated using non-Maxwellian electron distribution functions, consistent with thermal transport, with Maxwellian electron distribution functions. The excellent quality of the fits over the complete spectrum indicates the high accuracy of the shape of the distribution functions used. The significant deviation from the measured spectra that occurs when not accounting for the effects of heat flux (i.e., Maxwellian distribution functions) shows the sensitivity of the measurement. The non-Maxwellian distribution functions were calculated from a series of Fokker–Planck simulations<sup>39</sup> with varying boundary conditions but with the electron temperature and density profiles equal to the measured values.

Figure 155.3 shows the resulting heat-flux measurements at the five probed locations obtained by integrating the electron distribution functions used to fit the Thomson-scattering spectrum  $[q_{\text{TTS}} = \int (1/2)mv^2 \mathbf{v} f_e(\mathbf{v}) d^3 v]$ . The measured heat flux is compared to classical heat flux values ( $q_{\text{SH}} = -\kappa \nabla T_e$ ) determined by calculating the Spitzer thermal conductiv-



E27294JR

Figure 155.3

The heat flux (red circles) measured along the target normal is compared with classical heat flux (SH) calculations (blue triangles) and heat-flux values obtained from the simulations using the Schurtz–Nicolai–Busquet (SNB) model (black diamonds). Both the simulations and calculations were initiated with the measured electron temperatures and densities. For reference,  $\lambda_{\text{ei}}/L_T = 1.4 \times 10^{-2}$ ,  $1.4 \times 10^{-2}$ ,  $1.3 \times 10^{-2}$ ,  $1.0 \times 10^{-2}$ , and  $7 \times 10^{-3}$  at 1.1 mm, 1.2 mm, 1.3 mm, 1.4 mm, and 1.5 mm, respectively.

ity and the local temperature gradient from the measured plasma profiles (Fig. 155.4). Excellent agreement between the classical and measured heat flux is observed for the location farthest from the target surface, but for locations closer to the target surface, the measured flux is smaller than the classical values. This difference highlights the nonlocal nature of the thermal transport.

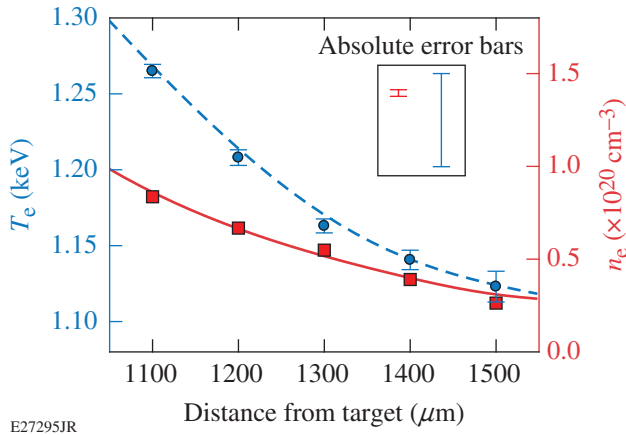


Figure 155.4

Electron temperature (blue circles, left axis) and density (red squares, right axis) measurements at  $t = 1.5$  ns. Profiles of electron temperature (dashed blue curve) and density (solid red curve) used in Fokker–Planck simulations. The relative ( $1\sigma$  statistical) error bars are shown with the temperature measurements. The absolute error bars are represented in the inset.

Figure 155.4 presents the measured electron temperature and density profiles determined from fitting the blue-shifted features with the Thomson-scattering power spectrum, assuming Maxwellian electron distribution functions (Fig. 155.2). The electron temperature decreased from  $1.27 \pm 0.04$  keV to  $1.12 \pm 0.04$  keV over  $400 \mu\text{m}$ . The electron temperature gradient at each measurement location was determined by fitting a fifth-order polynomial to the measurements. The uncertainty in the temperature gradient was calculated by varying the data within the relative error bars, which were used to calculate the errors in the classical heat flux (Fig. 155.3). Over this same distance, the electron density dropped from  $8.36 \pm 0.04 \times 10^{19} \text{ cm}^{-3}$  to  $2.63 \pm 0.01 \times 10^{19} \text{ cm}^{-3}$ . The high signal-to-noise ratio in the measured spectra resulted in excellent  $\chi^2$  statistical fits, which determined the  $1\sigma$  statistical relative error bars shown in Fig. 155.4. The absolute errors in the electron temperature and density were dominated by uncertainties in the spectral dispersion and resolution. Adding these errors in quadrature resulted in a 2% and 3% absolute error in the density and temperature, respectively.

For the measurement farthest from the target surface (1.5 mm), the Thomson-scattering spectrum calculated using the electron distribution function determined by classical SH theory, where  $\lambda_{ei}/L_T = 7 \times 10^{-3}$ , was in good agreement (Fig. 155.2). This is consistent with the agreement in the measured heat flux at this location presented in Fig. 155.3. Although the classical SH distribution function allows the amplitudes of the spectral peaks to be reproduced, the fit shows a discrepancy

in the width of the red-shifted peak, suggesting that the shape of the SH electron distribution function around the resonance is incorrect. For locations closer to the target, the electron distribution function predicted by classical theory becomes negative at velocities around the Langmuir wave resonances, and classical theory cannot be used to fit the measured spectrum. This is consistent with the measured heat flux being significantly less than the classical values (Fig. 155.3). At these locations  $\lambda_{ei}/L_T > 10^{-3}$ , which confirms experimentally the limit of validity previously determined by nonlocal theories.<sup>17–22</sup>

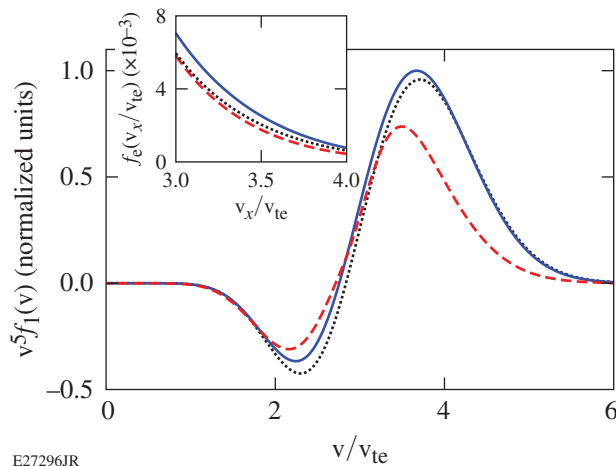
To determine the electron distribution functions consistent with nonlocal transport, the K2 Vlasov–Fokker–Planck code<sup>39</sup> was used. K2 uses a Legendre polynomial representation of the electron distribution function,  $f(t, x, \mathbf{v}) = \sum_n f_n(t, x, \mathbf{v}) P_n(\theta)$ , where  $x$  is the direction along the target normal. K2 solves for the self-consistent electric field and includes the effects of electron–ion scattering and electron–electron collisions. To capture the fine detail in the distribution functions at high velocities, close to the Langmuir wave resonances, polynomials up to and including  $f_8$  were required. In all calculations, the plasma profiles were initially set to the measurements (Fig. 155.4) and the temperature at the boundary of the simulation closest to the target ( $\sim 500 \mu\text{m}$ ) was varied between 1.2 keV and 2 keV. Since the transport is nonlocal, the choice of boundary condition is important to determine heat flow at the edge of the measurement region (i.e., 1.1 mm) but has a small effect at the other measurement positions.

Once the initial conditions were set, the K2 code evolved the distribution function in time and, after a few collision times, reached steady state. Over this time, a small amount of heating/cooling was applied to the electrons to help maintain the temperature profile close to the measured (i.e., initial) values. This approximately accounted for the small amount of ongoing thermal compression/expansion in the coronal region. Since the hydrodynamic motion is slow compared to the electron thermal transport, it was ignored. For each boundary condition, the electron distribution functions at each measurement position were used to calculate Thomson-scattering spectra. The boundary condition (1.8 keV) that generated the Thomson-scattering spectra with the best match across all locations was used to determine the measured heat flux. The resulting electron distribution functions were used in Eq. (1) to calculate the spectra shown in Fig. 155.2.

The measured heat flux was compared to calculations that used the multigroup nonlocal SNB model (Fig. 155.3), initialized with the measured electron temperature and density

profiles (Fig. 155.4). In the nonlocal region, where classical SH theory overestimates the flux, the SNB model calculates a flux that is about halfway between the classical and measured values. In the region where classical transport is valid (1.5 mm), the SNB model overestimates the flux by 75%. Furthermore, in the nonlocal transport regions, the electron distribution functions were negative around the electron plasma wave resonance, which made it impossible to fit the measured Thomson-scattering spectrum.

Figure 155.5 shows the flux contribution of electrons for each of the models at 1.2 mm from the target surface. According to the K2 model, the reduction in heat flux relative to the classical model at this location occurs as a result of a reduction in the flux of electrons with  $v \gtrsim 3.4 v_{te}$ . Furthermore, the peak heat flow occurs at a lower velocity ( $v_{K2} \approx 3.5 v_{te}$ ) relative to the classical result ( $v_{SH} \approx 3.7 v_{te}$ ). The SNB model slightly inhibits the flux but still overpredicts the heat flow. The heat flux at this location is 60% of the classical value.



E27296JR

Figure 155.5

The velocity-dependent contribution of heat flux at 1200  $\mu\text{m}$  for calculations using the Fokker–Planck (dashed red curve), classical (dotted blue curve), and SNB (solid black curve) models. The inset shows the corresponding electron distribution functions.

In summary, Thomson scattering was used to measure the heat flux directly from the amplitudes of the Langmuir fluctuations and indirectly through the electron temperature and density profiles ( $q_{SH} = \kappa \nabla T_e$ ). The measured heat flux agreed with classical SH values when  $\lambda_{ei}/L_T < 10^{-3}$ , but in the opposite limit ( $\lambda_{ei}/L_T > 10^{-3}$ ), the differences were as large as a factor of 2. The multigroup nonlocal SNB model overpredicted the flux in all regions, which demonstrates the need to include

physics often missing from computationally expedient nonlocal models, most notably high-order polynomials for properly resolving velocity space, the self-consistent electric field, and a Fokker–Planck collision operator.

#### ACKNOWLEDGMENT

This work was supported by the U.S. Department of Energy under Cooperative Agreement No. DE-NA0001944, the University of Rochester, and the New York State Energy Research and Development Authority. M. Sherlock's contribution to this work was performed under the auspices of the U.S. Department of Energy by LLNL under Contract DE-AC52-07NA27344.

#### REFERENCES

1. L. Spitzer, Jr. and R. Härm, *Phys. Rev.* **89**, 977 (1953).
2. S. I. Braginskii, *J. Exptl. Theoret. Phys. (U.S.S.R.)* **33**, 459 (1957).
3. G. Zimmerman *et al.*, *J. Opt. Soc. Am.* **68**, 549 (1978).
4. M. M. Marinak *et al.*, *Phys. Plasmas* **3**, 2070 (1996).
5. B. Fryxell *et al.*, *Astrophys. J. Suppl. Ser.* **131**, 273 (2000).
6. A. J. Cunningham *et al.*, *Astrophys. J. Suppl. Ser.* **182**, 519 (2009).
7. B. Van der Holst *et al.*, *Astrophys. J. Suppl. Ser.* **194**, 23 (2011).
8. G. Gregori, S. H. Glenzer, J. Knight, C. Niemann, D. Price, D. H. Froula, M. J. Edwards, R. P. J. Town, A. Brantov, W. Rozmus, and V. Yu. Bychenkov, *Phys. Rev. Lett.* **92**, 205006 (2004).
9. R. D. Petrasso, J. A. Frenje, C. K. Li, F. H. Séguin, J. R. Rygg, B. E. Schwartz, S. Kurebayashi, P. B. Radha, C. Stoeckl, J. M. Soures, J. Delettrez, V. Yu. Glebov, D. D. Meyerhofer, and T. C. Sangster, *Phys. Rev. Lett.* **90**, 095002 (2003).
10. J. A. Tarvin *et al.*, *Phys. Rev. Lett.* **51**, 1355 (1983).
11. T. J. Goldsack *et al.*, *Opt. Commun.* **42**, 55 (1982).
12. B. B. Kadomtsev and O. P. Pogutse, in *Reviews of Plasma Physics*, edited by M. A. Leontovich (Consultants Bureau, New York, 1970), Vol. 5, Chap. 2, pp. 249–400.
13. M. S. White, J. D. Kilkeny, and A. E. Dangor, *Phys. Rev. Lett.* **35**, 524 (1975).
14. V. Yu. Bychenkov, V. P. Silin, and S. A. Uryupin, *Phys. Rep.* **164**, 119 (1988).
15. S. H. Glenzer *et al.*, *Phys. Rev. Lett.* **88**, 235002 (2002).
16. D. R. Gray and J. D. Kilkeny, *Plasma Phys.* **22**, 81 (1980).
17. A. R. Bell, R. G. Evans, and D. J. Nicholas, *Phys. Rev. Lett.* **46**, 243 (1981).
18. J. P. Matte and J. Virmont, *Phys. Rev. Lett.* **49**, 1936 (1982).

19. A. R. Bell, *Phys. Fluids* **26**, 279 (1983).
20. J. F. Luciani, P. Mora, and J. Virmont, *Phys. Rev. Lett.* **51**, 1664 (1983).
21. J. R. Albritton, E. A. Williams, and I. B. Bernstein, *Phys. Rev. Lett.* **57**, 1887 (1986).
22. V. Yu *et al.*, *Phys. Rev. Lett.* **75**, 4405 (1995).
23. G. P. Schurtz, Ph. D. Nicolaï, and M. Busquet, *Phys. Plasmas* **7**, 4238 (2000).
24. V. N. Goncharov, O. V. Gotchev, E. Vianello, T. R. Boehly, J. P. Knauer, P. W. McKenty, P. B. Radha, S. P. Regan, T. C. Sangster, S. Skupsky, V. A. Smalyuk, R. Betti, R. L. McCrory, D. D. Meyerhofer, and C. Cherfils-Clérrouin, *Phys. Plasmas* **13**, 012702 (2006).
25. R. C. Malone, R. L. McCrory, and R. L. Morse, *Phys. Rev. Lett.* **34**, 721 (1975).
26. G. Murtaza, A. M. Mirza, and M. S. Qaisar, *Phys. Scr.* **47**, 811 (1993).
27. J. R. Albritton, *Phys. Rev. Lett.* **50**, 2078 (1983).
28. D. T. Michel, A. K. Davis, V. N. Goncharov, T. C. Sangster, S. X. Hu, I. V. Igumenshchev, D. D. Meyerhofer, W. Seka, and D. H. Froula, *Phys. Rev. Lett.* **114**, 155002 (2015).
29. W. C. Mead, E. M. Campbell, W. L. Kruer, R. E. Turner, C. W. Hatcher, D. S. Bailey, P. H. Y. Lee, J. Foster, K. G. Tirsell, B. Pruett, N. C. Holmes, J. T. Trainor, G. L. Stradling, B. F. Lasinski, C. E. Max, and F. Ze, *Phys. Fluids B* **27**, 1301 (1984).
30. S. H. Glenzer *et al.*, *Phys. Rev. Lett.* **82**, 97 (1999).
31. D. H. Froula, J. S. Ross, L. Divol, N. Meezan, A. J. MacKinnon, R. Wallace, and S. H. Glenzer, *Phys. Plasmas* **13**, 052704 (2006).
32. J. Hawreliak *et al.*, *J. Phys. B: At. Mol. Opt. Phys.* **37**, 1541 (2004).
33. D. H. Froula, S. H. Glenzer, N. C. Luhmann, Jr., and J. Sheffield, *Plasma Scattering of Electromagnetic Radiation: Theory and Measurement Techniques*, 2nd ed. (Academic Press, Amsterdam, 2011).
34. W. Rozmus *et al.*, *Phys. Plasma* **23**, 012707 (2016).
35. T. R. Boehly, D. L. Brown, R. S. Craxton, R. L. Keck, J. P. Knauer, J. H. Kelly, T. J. Kessler, S. A. Kumpan, S. J. Loucks, S. A. Letzring, F. J. Marshall, R. L. McCrory, S. F. B. Morse, W. Seka, J. M. Soures, and C. P. Verdon, *Opt. Commun.* **133**, 495 (1997).
36. T. J. Kessler, Y. Lin, J. J. Armstrong, and B. Velazquez, *Proc. SPIE* **1870**, 95 (1993).
37. J. Katz, R. Boni, C. Sorce, R. Follett, M. J. Shoup III, and D. H. Froula, *Rev. Sci. Instrum.* **83**, 10E349 (2012).
38. A. J. Mackinnon, S. Shiromizu, G. Antonini, J. Auerbach, K. Haney, D. H. Froula, J. Moody, G. Gregori, C. Constantin, C. Sorce, L. Divol, R. L. Griffith, S. Glenzer, J. Satariano, P. K. Whitman, S. N. Locke, E. L. Miller, R. Huff, K. Thorp, W. Armstrong, W. Bahr, W. Seka, G. Pien, J. Mathers, S. Morse, S. Loucks, and S. Stagnitto, *Rev. Sci. Instrum.* **75**, 3906 (2004).
39. M. Sherlock, J. P. Brodrick, and C. P. Ridgers, *Phys. Plasmas* **24**, 082706 (2017).

---

# Ray-Based Modeling of Cross-Beam Energy Transfer at Caustics

In laser-based inertial confinement fusion (ICF), a millimeter-scale cryogenic capsule of deuterium–tritium fuel with a thin outer ablator is imploded either directly by laser illumination or indirectly by x rays emitted from a laser-heated, high-Z hohlraum.<sup>1,2</sup> In both approaches, multiple laser beams overlap in a plasma and their low-frequency beat waves can drive ion-acoustic waves. By means of a process known as cross-beam energy transfer (CBET), the ion-acoustic waves mediate the transfer of energy between beams, significantly impacting the deposition of laser energy.<sup>3</sup>

Direct-drive ICF experiments on the OMEGA laser<sup>4</sup> have shown a 10% to 20% reduction in laser absorption because of CBET.<sup>5</sup> Indirect-drive ICF experiments at the National Ignition Facility (NIF) have exploited CBET to control implosion symmetry by tuning the wavelength separation between laser beams.<sup>6,7</sup> The scale of these experiments, in terms of preparation time, complexity, and cost, necessitate the use of radiation-hydrodynamic simulations with CBET models for the rapid design, tuning, and optimization of implosions.<sup>8</sup>

As a result of the computational expense of wave-based calculations, the CBET models used in radiation-hydrodynamic codes are exclusively based on ray tracing; even then, 3-D implementations can be prohibitive. Furthermore, existing CBET models require artificial multipliers to obtain quantitative agreement with experiments.<sup>7,9–12</sup> This is, in part, due to a major challenge of ray tracing: the reconstruction of the field amplitude diverges at caustics. While sophisticated techniques exist for approximating the full solution to the electromagnetic wave equation in the vicinity of caustics,<sup>13</sup> there is no consensus as to how caustics should be treated in ray-based CBET models.

The use of artificial multipliers is particularly problematic in the complex radiation-hydrodynamic codes used to simulate ICF implosions because they model the interaction between many different physical processes, and an artificial multiplier in one physics model can mask deficiencies and inhibit progress in seemingly unrelated areas. Similarly, it is important

to validate reduced models like ray-based CBET calculations against more-complete calculations so that when discrepancies do arise, there is some level of confidence as to whether the discrepancy is caused by missing physics or an inaccurate solution to the original problem.

In this article, we present a ray-based CBET algorithm that opens up the possibility for full-scale 3-D CBET modeling in radiation-hydrodynamic codes without the need for artificial multipliers. The key insight is that the energy transfer between beams should be truncated past the caustic of the pump beam. Ray-based CBET calculations with caustic gain truncation (CGT) show excellent agreement with laser absorption from both 2-D wave-based calculations and a 3-D 60-beam OMEGA implosion. A large difference between results obtained with and without CGT (in terms of both accuracy and energy conservation) indicates the importance of including a careful treatment of caustics in ray-based CBET calculations.

Ray-based CBET modeling relies on the assumption that the energy exchange between two lasers can be approximated locally using the homogeneous gain, and that the interaction between all rays in a given region of space can be treated independently, pairwise. Additionally, the large separation between the hydrodynamic and acoustic/electromagnetic time scales allows for steady-state CBET calculations using the instantaneous hydrodynamic conditions.

The general approach to ray-based CBET modeling follows four steps: (1) calculate trajectories for all rays in each laser beam, (2) discretize the ray trajectories along their paths, (3) determine all possible pairwise interactions, and (4) solve the resulting system of equations for the energies along the ray paths. Here it is assumed that steps (1) and (2) have already been completed. In terms of the absolute square of the enveloped electric field, the differential change of the  $i$ th ray (the seed ray) at the  $j$ th location along its path resulting from an interaction with the  $k$ th ray (the pump ray) at the  $l$ th location along its path for parallel-polarized beams in a homogeneous plasma is (in cgs units)<sup>3</sup>

$$\frac{d|E_{ij}|^2}{ds} = -\frac{|E_{ij}|^2}{L_a^{ij}} + \frac{g_{ijkl}}{L_s^{ijkl}} \frac{|E_{ij}|^2}{\sqrt{\varepsilon}} \frac{|E_{kl}|^2}{|E_{k0}|^2}, \quad (1)$$

where  $\varepsilon = 1 - n_e/n_c$ ,  $n_e$  is the electron density,

$$n_c = m_e \omega_{ij}^2 / (4\pi e^2)$$

is the critical density for light with frequency  $\omega_{ij}$  (and wave vector  $\mathbf{k}_{ij}$ ),  $m_e$  is the electron mass,  $-e$  is the electron charge,

$$(L_s^{ijkl})^{-1} = \frac{e^2 |E_{k0}|^2}{4m_e c \omega_{ij} k_B T_e (1 + 3T_e/ZT_e)} \frac{n_e}{n_c} \frac{\omega_s}{\nu_{ia}} P(\eta_{ijkl}),$$

$$P(\eta) = \frac{(\nu_{ia}/\omega_s)^2 \eta}{(\eta^2 - 1)^2 + (\nu_{ia}/\omega_s)^2 \eta^2},$$

$$\eta_{ijkl} = \frac{\omega_{kl} - \omega_{ij} - (\mathbf{k}_{kl} - \mathbf{k}_{ij}) \cdot \mathbf{u}}{\omega_s},$$

$\nu_{ia}$  is the ion-acoustic wave energy-damping rate,  $\omega_s$  is the acoustic frequency,  $T_e$  ( $T_i$ ) is the electron (ion) temperature,  $Z$  is the ionization state,  $k_B$  is Boltzmann's constant, and  $\mathbf{u}$  is the plasma flow velocity.  $L_a^{ij} = c\sqrt{\varepsilon} n_c / (\nu_{ei} n_e)$  is the laser absorption length,<sup>14</sup> where

$$\nu_{ei} = 4\sqrt{2\pi} e^4 Z^2 n_i \Lambda_{ei} / (3\sqrt{m_e} T_e^{3/2});$$

$\Lambda_{ei}$  is the Coulomb logarithm;<sup>15</sup>  $|E_{k0}| = \sqrt{8\pi I_{k0}/c}$  is the magnitude of the incident (vacuum) field of the  $k$ th ray; and  $I_{k0}$  is the corresponding intensity.

The function  $g_{ijkl}$  is introduced to account for the fact that there may not be a valid interaction between the two rays. Two rays will interact if they (1) intersect in configuration space and (2) are on distinct "sheets," where each sheet corresponds to a region of ray phase space that has a single-valued projection onto the configuration space [the divisions between sheets are at caustics (shown later in Fig. 155.8)].<sup>13</sup> Accordingly,  $g_{ijkl} = 1$  if both of these conditions are satisfied and 0 otherwise. If the ray paths are discretized on a grid, being at the same location in configuration space is equivalent to being in the same grid cell.

Equation (1) can be discretized along ray trajectories in an inhomogeneous plasma if it is written in terms of ray energy, which is conserved along ray trajectories in the absence of CBET and absorption. In the geometric optics limit,  $|E_{ij}|^2 / |E_{i0}|^2 = W_{ij} (dS_{i0}/dS_{ij}) / \sqrt{\varepsilon}$ , where  $W_{ij}$  is the ray energy normalized to the incident energy ( $W_{i0} = 1$ ) and  $dS_{i0}/dS_{ij}$  is the ratio of the initial to current cross-sectional area of the  $i$ th ray, which is tracked by tracing bundles of rays.<sup>16</sup> This approximation for the fields diverges at caustics where either  $\varepsilon \rightarrow 0$  or  $dS_{ij}/dS_{i0} \rightarrow 0$ . A simple way to correct for this is to treat the density profile as being locally linear. The field of a plane wave incident on a linear density gradient ( $n_e/n_c = x/L$ ) has an analytic solution (Airy function) with a peak field

$$\left( |E_{ij}|^2 / |E_{i0}|^2 \right)_{\max} = \xi_{ij} (n_e/n_c)_{i,\max}^{1/2}$$

(Ref. 14), where  $(n_e/n_c)_{i,\max}$  is the maximum density along the path of the  $i$ th ray,  $\xi_{ij} = 0.9(\omega_{ij}L/c)^{1/3}$ , and  $L = L_* n_c / n_*$  ( $n_*$  and  $L_*$  are the density and density scale length at the caustic). Applying this as a limit to the peak field amplitude, Eq. (1) becomes

$$\frac{dW_{ij}}{ds} = -\frac{W_{ij}}{L_a^{ij}} + g_{ijkl} \frac{W_{ij} W_{kl}}{\sqrt{\varepsilon} L_s^{ijkl}} \min \left[ \frac{1}{\sqrt{\varepsilon}} \frac{dS_{k0}}{dS_{kl}}, \xi_{kl} \left( \frac{n_e}{n_c} \right)_{\max}^{1/2} \right]. \quad (2)$$

Equation (2) is the differential change in energy caused by a single pairwise interaction. In general, each ray can interact with every other sheet at every point along its path. Discretizing Eq. (2) along the ray paths and summing over all possible interactions gives

$$\frac{W_{i,j+1}}{W_{ij}} = \exp \left( -\frac{s_{ij}}{L_a^{ij}} + \frac{s_{ij}}{\sqrt{\varepsilon_{\text{eff}}}} \sum_{\mathcal{S}} \sum_{kl \in \mathcal{S}} \frac{W_{kl} g_{ijkl} \Delta S_{kl}}{\sum_{np \in \mathcal{S}} g_{ijnp}} \right), \quad (3)$$

where

$$\frac{1}{\sqrt{\varepsilon_{\text{eff}}}} = \min \left( \frac{1}{\sqrt{\varepsilon}}, 2\sqrt{\frac{L}{s_{ij}}} \right),$$

$$\Delta S_{kl} = \min \left[ \frac{1}{\sqrt{\varepsilon}} \frac{dS_{k0}}{dS_{kl}}, \xi_{kl} \left( \frac{n_e}{n_c} \right)_{\max}^{1/2} \right],$$

and  $s_{ij}$  is the length of the ray-path section from  $j$  to  $j + 1$  for ray  $i$ .  $\varepsilon_{\text{eff}}$  is introduced to keep the discretized equation from diverging when  $\varepsilon \rightarrow 0$ , which originates from the vanishing group velocity of the seed beam for near-normal-incidence rays. The path integral is finite, so we use the analytic result for normal-incidence rays in a linear density gradient,

$$\int_{L-s}^L dx / \sqrt{1-x/L} = 2\sqrt{sL}.$$

The first sum in Eq. (3) is over sheets  $\mathcal{S}$ , and the second sum is over all of the ray-path locations belonging to sheet  $\mathcal{S}$ . The summand corresponds to the expected interaction strength from all of the rays in the current grid cell on the current pump-beam sheet. In practice, it is more efficient if just one nonzero term from each sheet is used (chosen randomly). This has essentially no impact on the solution because all of the terms in the sums over  $k, l$  are equal in the limit  $s_{ij} \rightarrow 0$ .

Equation (3) is typically solved using fixed-point iteration. To improve the rate of convergence,<sup>16</sup> we substitute  $\tilde{W}_{ij} \equiv W_{ij}/W_{i,j-1}$  and obtain the ray-based CBET equation

$$\tilde{W}_{i,j+1} = \exp\left(-A_{ij} + \sum_{\mathcal{S}} \sum_{kl \in \mathcal{S}} G_{ijkl} \prod_{m=1}^l \tilde{W}_{km}\right), \quad (4)$$

where

$$G_{ijkl} = \frac{s_{ij} g_{ijkl} \Delta S_{kl}}{\sqrt{\varepsilon_{\text{eff}}} L_s^{ijkl} \sum_{np \in \mathcal{S}} g_{ijnp}} \quad (5)$$

and  $A_{ij} = s_{ij}/L_a^{ij}$ . Equation (4) is written in the form that is used to solve for  $\tilde{W}_{ij}$  because the  $A_{ij}$  and  $G_{ijkl}$  can be precalculated before starting the iterations. After solving for  $\tilde{W}_{ij}$ , the normalized ray energies are given by  $\tilde{W}_{ij} = \prod_{k=1}^j \tilde{W}_{ik}$ . Here the rays were discretized on a Cartesian grid except for the special case of rays changing sheets in a grid cell, where an additional split in the ray path is introduced at the sheet boundary. The limitations of this model that require the introduction of CGT are best illustrated by first introducing a prototypical example of CBET in the presence of fold caustics.

Figure 155.6 compares the electric fields from 2-D (a) ray- and (b) wave-based calculations of CBET between two beams in an azimuthally symmetric plasma. The wave-based calculations were performed using *LPSE* (laser-plasma simulation environment).<sup>16,17</sup> The ray-based solution was obtained by solving Eq. (4) and then taking the coherent sum of the fields from the four ray sheets (two from each beam).<sup>13</sup> The plasma conditions were similar to what would be encountered in an OMEGA implosion except they have been scaled down by a factor of 4. The laser intensities were  $2 \times 10^{15}$  W/cm<sup>2</sup> (0.351- $\mu$ m light), which was chosen such that CBET would have a significant impact on the laser-energy deposition. The *LPSE* grid resolution was 50 cells/ $\mu$ m. The fact that the results from the two calculations are difficult to distinguish by eye is a testament to the fact that the geometric optics approximation is valid

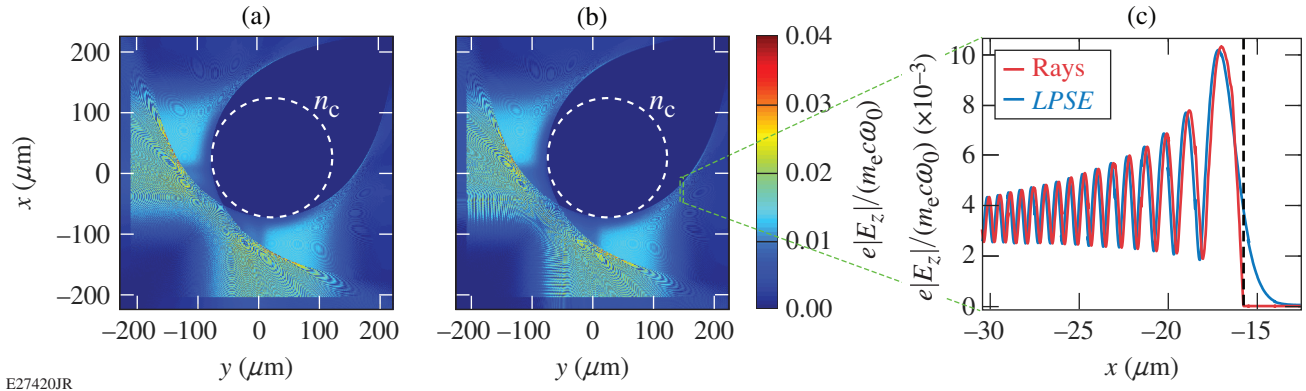
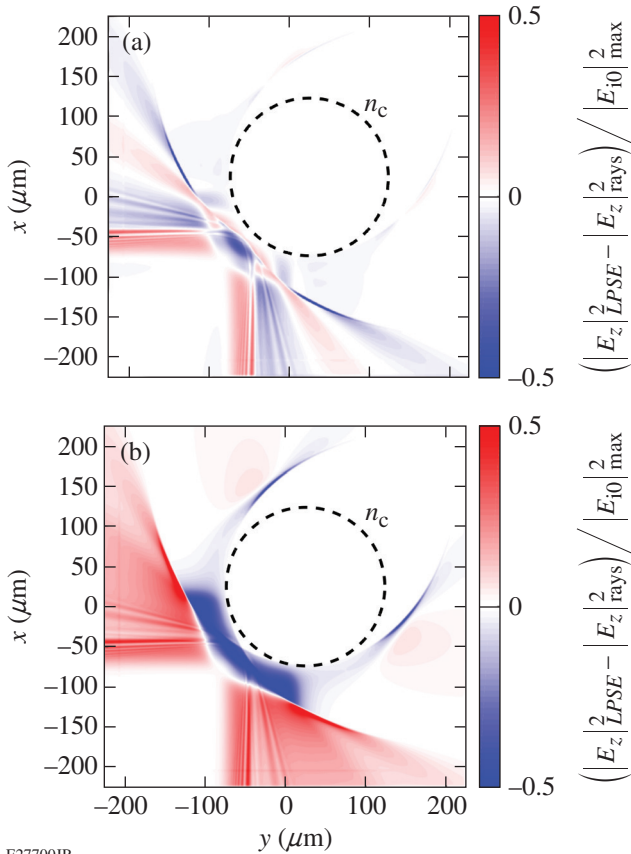


Figure 155.6

(a) Ray- and (b) wave-based simulations of the magnitude of the enveloped electric fields for two beams (injected from the bottom and left) interacting in an azimuthally symmetric plasma. The critical surface is indicated by a dashed line. (c) Lineouts of the fields from *LPSE* (blue) and rays (red). To compare the unperturbed fields, the lineouts are from calculations where CBET was turned off. The location of the caustic is denoted by a vertical dashed black line (where the field amplitude in the ray-based calculation drops to zero).

nearly everywhere in the long-scale-length plasmas encountered in ICF. The difference in field energy between the two calculations is shown in Fig. 155.7(a). Note that while there are significant differences between the two CBET calculations, the ray-based calculation over- and underpredicts the field energy in the scattering region in similar proportion. The differences between the fields are probably due in part to the fact that the laser propagation can be affected by the ponderomotively driven density perturbations in *LPSE* but not in the ray-based calculation. To put Fig. 155.7(a) in context, Fig. 155.7(b) shows the same comparison with CBET turned off in the ray model. This causes the ray-based calculation to dramatically underpredict the amount of scattered light.

Figure 155.6(c) shows a lineout of the fields from the two solutions at one of the caustics in calculations where CBET was turned off ( $G_{ijkl} = 0$ ). The fact that the agreement between



E27700JR

Figure 155.7

The difference in field energy in the ray- and wave-based calculations for (a) CBET turned on and (b) CBET turned off in the ray-based calculation. A Gaussian filter with a  $1\text{-}\mu\text{m}$  standard deviation has been applied to smooth out differences resulting from phase mismatches in regions with high-frequency interference.

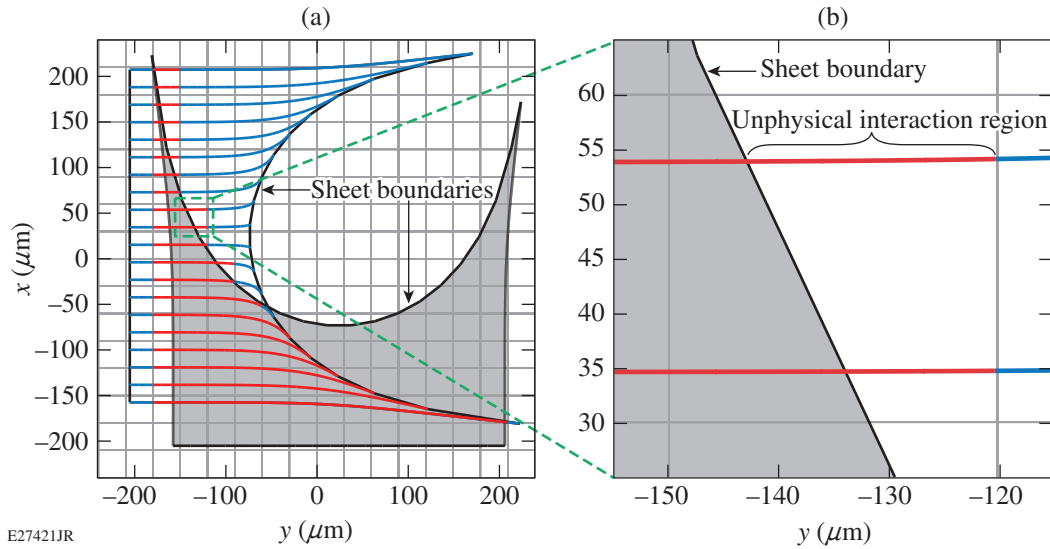
the solutions is excellent right up to the edge of the ray sheet (vertical dashed black line) suggests that the simple approximation used to calculate the fields at the caustic does not have a significant impact on the accuracy of the global solution. The depicted lineouts were taken relatively far from the center of the caustic to give a stringent test of the ray-based solution; the accuracy of the approximation degrades for increasingly oblique rays.

The limitation of Eq. (4) is depicted in Fig. 155.8, which shows the first sheet of each beam (one shaded gray and one as rays with a black outline) and the Cartesian grid that was used to discretize the ray trajectories. The rays in the beam coming from the left should interact only with the beam coming from the bottom when they are inside the gray region because the field of the beam coming from the bottom vanishes outside that region. Because of the discretization, however, the rays interact wherever they are colored red. In the CGT algorithm, the CBET interaction length in Eq. (5) is allowed to depend on the pump ray such that the gain of a seed ray is limited to only the portion of the grid cell where it is inside the corresponding pump-beam sheet. Accordingly, we introduce a new path length  $s_{ijkl}$ , which depends on the indices of the pump ray and appears only in the CBET term but is equal to  $s_{ij}$  in grid cells where the beam corresponding to the  $k$ th ray does not have a caustic,

$$G_{ijkl} = \frac{s_{ijkl} g_{ijkl} \Delta S_{kl}}{\sqrt{\epsilon_{\text{eff}}} L_s^{ijkl} \sum_{np \in \mathcal{S}} g_{ijnp}}. \quad (6)$$

The  $s_{ijkl}$  is determined by finding the intersections between the seed rays and the sheet boundaries of the pump beams. In 2-D, the sheet boundaries are polygons; in 3-D, the sheet boundaries are closed surfaces that are stored on a triangle mesh. Despite the fact that the CGT correction is spatially localized to the caustic region, it has a large impact on the global solution because of the highly nonlinear nature of Eq. (4). Note that although a Cartesian grid was used here, Eq. (4) does not make any assumptions about the grid, and essentially any gridding scheme will suffer from the same issue (except for an unstructured grid constructed from the sheet boundaries).

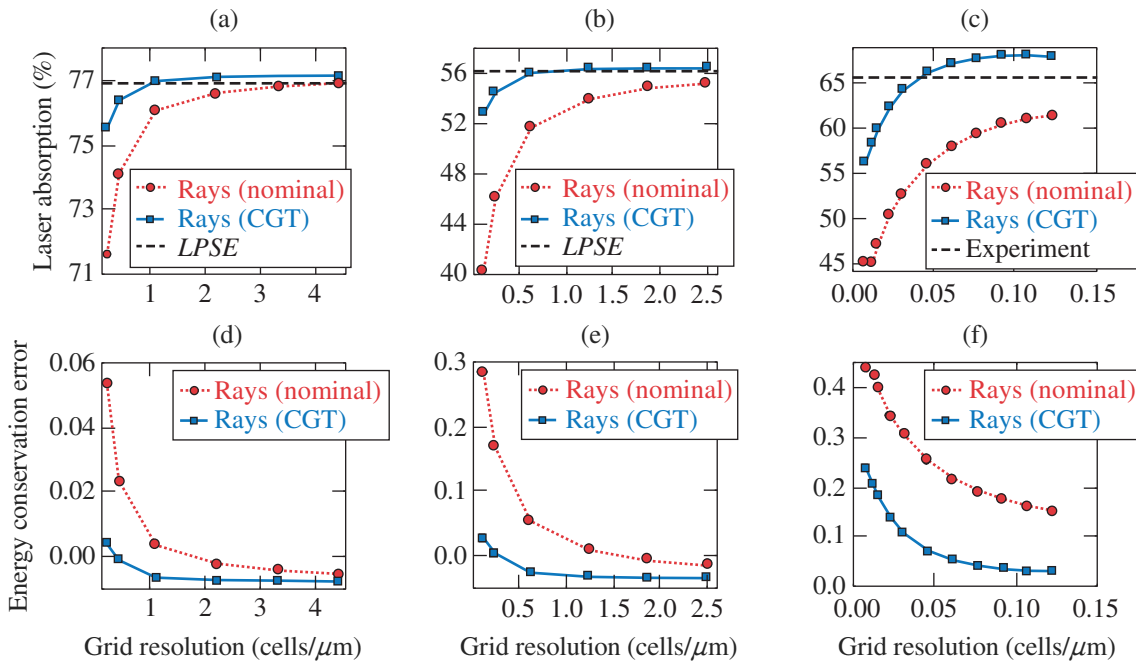
Figures 155.9(a) and 155.9(b) show the laser absorption as a function of the CBET grid resolution using the nominal and CGT ray-based CBET algorithms to two-beam (cf. Fig. 155.6) and 16-beam *LPSE* calculations, respectively. The 16-beam calculations used the same plasma conditions as the two-beam calculations with the beams injected uniformly at  $22.5^\circ$  increments with



E27421JR

Figure 155.8

(a) The first sheet of the two beams for the configuration shown in Fig. 155.6 overlaid on the Cartesian grid; (b) a close-up of one of the grid cells. The red area of the ray trajectories show where the rays would interact with the beam coming from the bottom without the caustic gain truncation (CGT) correction. Note that finite sheets are shown for illustrative purposes; only the parabolic edge corresponds to a caustic. The other edges of the sheet are chosen such that the intensity is vanishingly small (for the sides) or outside the interaction region (for the injector).



E27422JR

Figure 155.9

[(a)–(c)] The laser absorption and [(d)–(f)] energy conservation error for the nominal (red circles) and CGT (blue squares) ray-trace algorithms as functions of grid resolution for [(a),(d)] 2-D two-beam calculations; [(b),(e)] 2-D 16-beam calculations; and [(c),(f)] 3-D 60-beam calculations. The 2-D calculations are compared to LPSE results and the 3-D calculations are compared to OMEGA results (dashed black lines).

intensities of  $4 \times 10^{14}$  W/cm<sup>2</sup>. Both simulations had a significant reduction in laser absorption because of CBET (the absorption without CBET was 96%), and at the highest grid resolutions, the ray-based results were within 0.3% of the LPSE results. The nominal and CGT ray-based algorithms converge to the same result in the limit of infinite resolution because the size of the grid cells where the error is introduced in the nominal calculations vanishes. Convergence is achieved much more rapidly using the CGT algorithm, particularly in the 16-beam case (because there are many more caustics). The highest-resolution calculation with the nominal algorithm had an accuracy comparable to the CGT algorithm with an order-of-magnitude-less resolution. The computational cost of solving Eq. (4) is proportional to the number of grid cells, so an order-of-magnitude reduction in resolution represents a large computational savings: a factor of 100 in 2-D and a factor of 1000 in 3-D.

Figure 155.9(c) shows the results of 3-D CBET calculations of the instantaneous laser absorption during the main drive of a 60-beam OMEGA implosion with peak single-beam intensities of  $8.8 \times 10^{13}$  W/cm<sup>2</sup>. The plasma profiles were taken from the 1-D radiation-hydrodynamic code *LILAC*.<sup>18</sup> The 3-D calculations included several corrections that are typically included in radiation-hydrodynamic codes (the Langdon effect,<sup>19</sup> the Dewandre effect,<sup>20</sup> and polarization smoothing<sup>16,21</sup>).

As suggested by the difference between the two-beam and 16-beam results in 2-D, the difference between the CGT and nominal algorithms is even more striking in the 3-D 60-beam results. At the highest resolution ( $4 \times 10^6$  grid cells,  $7 \times 10^6$  rays, and  $9 \times 10^9$  interactions) that was achievable because of memory constraints, the nominal algorithm was still far from converging with the CGT result. The difference in laser absorption between the CGT calculation at the highest resolution and the experiment was 2.4%.

Figures 155.9(d)–155.9(f) show the energy conservation error in the ray-based solvers (defined as the difference between the incident energy and the sum of the absorbed and scattered energies normalized to the incident energy). It is critical to consider energy conservation when assessing a ray-based CBET algorithm because the underlying discretized equations do not explicitly conserve energy. Away from caustics, they conserve energy in the limit of infinite resolution, but in the presence of caustics, even the converged solutions are nonconserving. The energy conservation error is corrected for in an *ad hoc* manner in radiation-hydrodynamic codes, but there is no consensus as to how such corrections should be implemented. Regardless of

the technique, ray-based CBET results should not be expected to be any more accurate than their uncorrected conservation error because any correction produces a result that is no longer a solution to the original equation. For example, the difference between the nominal ray-trace absorption and the measurement is only 4.2% in the highest-resolution 3-D calculations, but this result is of little value because 15.2% of the energy is unaccounted for and correcting for that could have a large impact on the result. With the CGT algorithm, the conservation error is only 3.4%, which suggests that whatever correction is made to enforce energy conservation will produce a result that is still relatively faithful to Eq. (4).

In summary, a new algorithm was presented for ray-based CBET calculations in the presence of caustics. The CGT algorithm significantly improves accuracy and energy conservation in ray-based CBET calculations and shows excellent agreement with 2-D two- and 16-beam wave-based calculations and a 60-beam OMEGA implosion without the use of artificial multipliers. The increasing discrepancy between the nominal and CGT ray-based CBET algorithms with an increasing number of laser beams emphasizes the importance of a careful treatment of caustics in many-beam laser configurations.

#### ACKNOWLEDGMENT

This material is based upon work supported by the Department of Energy National Nuclear Security Administration under Award No. DE-NA0001944, the University of Rochester, and the New York State Energy Research and Development Authority. The support of the DOE does not constitute an endorsement by the DOE of the views expressed in this article.

#### REFERENCES

1. J. Nuckolls *et al.*, *Nature* **239**, 139 (1972).
2. R. S. Craxton, K. S. Anderson, T. R. Boehly, V. N. Goncharov, D. R. Harding, J. P. Knauer, R. L. McCrory, P. W. McKenty, D. D. Meyerhofer, J. F. Myatt, A. J. Schmitt, J. D. Sethian, R. W. Short, S. Skupsky, W. Theobald, W. L. Kruer, K. Tanaka, R. Betti, T. J. B. Collins, J. A. Delettrez, S. X. Hu, J. A. Marozas, A. V. Maximov, D. T. Michel, P. B. Radha, S. P. Regan, T. C. Sangster, W. Seka, A. A. Solodov, J. M. Soures, C. Stoeckl, and J. D. Zuegel, *Phys. Plasmas* **22**, 110501 (2015).
3. C. J. Randall, J. R. Albritton, and J. J. Thomson, *Phys. Fluids* **24**, 1474 (1981).
4. T. R. Boehly, R. S. Craxton, T. H. Hinterman, J. H. Kelly, T. J. Kessler, S. A. Kumpan, S. A. Letzring, R. L. McCrory, S. F. B. Morse, W. Seka, S. Skupsky, J. M. Soures, and C. P. Verdon, *Rev. Sci. Instrum.* **66**, 508 (1995).
5. I. V. Igumenshchev, W. Seka, D. H. Edgell, D. T. Michel, D. H. Froula, V. N. Goncharov, R. S. Craxton, L. Divol, R. Epstein, R. Follett, J. H.

- Kelly, T. Z. Kosc, A. V. Maximov, R. L. McCrory, D. D. Meyerhofer, P. Michel, J. F. Myatt, T. C. Sangster, A. Shvydky, S. Skupsky, and C. Stoeckl, *Phys. Plasmas* **19**, 056314 (2012).
6. P. Michel *et al.*, *Phys. Plasmas* **16**, 042702 (2009).
  7. P. Michel *et al.*, *Phys. Plasmas* **17**, 056305 (2010).
  8. V. N. Goncharov, T. C. Sangster, R. Betti, T. R. Boehly, M. J. Bonino, T. J. B. Collins, R. S. Craxton, J. A. Delettrez, D. H. Edgell, R. Epstein, R. K. Follett, C. J. Forrest, D. H. Froula, V. Yu. Glebov, D. R. Harding, R. J. Henchen, S. X. Hu, I. V. Igumenshchev, R. Janezic, J. H. Kelly, T. J. Kessler, T. Z. Kosc, S. J. Loucks, J. A. Marozas, F. J. Marshall, A. V. Maximov, R. L. McCrory, P. W. McKenty, D. D. Meyerhofer, D. T. Michel, J. F. Myatt, R. Nora, P. B. Radha, S. P. Regan, W. Seka, W. T. Shmayda, R. W. Short, A. Shvydky, S. Skupsky, C. Stoeckl, B. Yaakobi, J. A. Frenje, M. Gatu-Johnson, R. D. Petrasso, and D. T. Casey, *Phys. Plasmas* **21**, 056315 (2014).
  9. J. A. Marozas, M. Hohenberger, M. J. Rosenberg, D. Turnbull, T. J. B. Collins, P. B. Radha, P. W. McKenty, J. D. Zuegel, F. J. Marshall, S. P. Regan, T. C. Sangster, W. Seka, E. M. Campbell, V. N. Goncharov, M. W. Bowers, J.-M. G. Di Nicola, G. Erbert, B. J. MacGowan, L. J. Pelz, and S. T. Yang, *Phys. Rev. Lett.* **120**, 085001 (2018).
  10. I. V. Igumenshchev, D. H. Edgell, V. N. Goncharov, J. A. Delettrez, A. V. Maximov, J. F. Myatt, W. Seka, A. Shvydky, S. Skupsky, and C. Stoeckl, *Phys. Plasmas* **17**, 122708 (2010).
  11. D. H. Edgell, R. K. Follett, I. V. Igumenshchev, J. F. Myatt, J. G. Shaw, and D. H. Froula, *Phys. Plasmas* **24**, 062706 (2017).
  12. A. K. Davis, D. Cao, D. T. Michel, M. Hohenberger, D. H. Edgell, R. Epstein, V. N. Goncharov, S. X. Hu, I. V. Igumenshchev, J. A. Marozas, A. V. Maximov, J. F. Myatt, P. B. Radha, S. P. Regan, T. C. Sangster, and D. H. Froula, *Phys. Plasmas* **23**, 056306 (2016).
  13. E. R. Tracy *et al.*, *Ray Tracing and Beyond: Phase Space Methods in Plasma Wave Theory* (Cambridge University, Cambridge, England, 2014).
  14. W. L. Kruer, *The Physics of Laser Plasma Interactions, Frontiers in Physics*, Vol. 73, edited by D. Pines (Addison-Wesley, Redwood City, CA, 1988).
  15. J. D. Huba, *NRL Plasma Formulary*, Naval Research Laboratory, Washington, DC, Report NRL/PU/6790-94-265 (1994).
  16. R. K. Follett, D. H. Edgell, D. H. Froula, V. N. Goncharov, I. V. Igumenshchev, J. G. Shaw, and J. F. Myatt, *Phys. Plasma* **24**, 103128 (2017).
  17. J. F. Myatt, R. K. Follett, J. G. Shaw, D. H. Edgell, D. H. Froula, I. V. Igumenshchev, and V. N. Goncharov, *Phys. Plasmas* **24**, 056308 (2017).
  18. J. Delettrez, R. Epstein, M. C. Richardson, P. A. Jaanimagi, and B. L. Henke, *Phys. Rev. A* **36**, 3926 (1987).
  19. A. B. Langdon, *Phys. Rev. Lett.* **44**, 575 (1980).
  20. T. Dewandre, J. R. Albritton, and E. A. Williams, *Phys. Fluids* **24**, 528 (1981).
  21. P. Michel *et al.*, *Phys. Plasmas* **20**, 056308 (2013).

# Tritium Retention in Hexavalent Chromate-Conversion-Coated Aluminum Alloy

## Introduction

Aluminum is used as a material for the OMEGA target chamber walls and for diagnostics that are in close proximity to the target chamber because of the small number of impurities contained in the lattice and the short lifetime of any neutron-activated isotopes. This material selection mitigates the radiological factors that stem from DT neutron activation but does not account for tritium interactions with the metal. It is well established that tritium will migrate from the gas phase into the metal bulk. Previous work has shown that surface modifications of materials have a tremendous impact on the total quantity of tritium retained by the sample.<sup>1-4</sup>

Hexavalent chromium-conversion coatings increase the corrosion resistance of aluminum alloy by forming a layer of Cr(III) hydroxide.<sup>5,6</sup> This passive layer can increase the lifetime of the aluminum piece by inhibiting corrosion. The mechanism of chromate-conversion coating (CCC) on an aluminum alloy is proposed to proceed by a sol-gel route.<sup>5,7</sup> In the sol-gel mechanism, a coupled redox reaction occurs that oxidizes aluminum metal and activates the hexavalent chromium-coating material by reducing the chromium. The aqueous solution containing both trivalent chromium and trivalent aluminum species will further react through hydrolysis to form a network of chromium hydride as shown in Fig. 155.10.

Upon drying, these polymeric hydrated films of chromium hydroxide collapse to form a cracked, broken network of chromium hydroxide on the surface of the material. These chromium layers act as a barrier to corrosion of the underlying aluminum substrate; however, there have been no studies to investigate how these films interact with a tritium environment.

## Experimental Setups and Procedures

Samples of dimensions  $5.1 \times 1.9 \times 0.3 \text{ cm}^3$  were cut from a common plate of aluminum 6061. Approximately 0.86 mm of the surface was machined away to eliminate any surface inclusions that can arise from manufacturing. Samples that did not receive any further surface modifications were degreased first with acetone, followed by water, and finally isopropyl alcohol to dry the samples; these samples are referred to as “unmodified.” Conversely, a set of samples had the surface modified by the commercial CCC described above. Materials characterization was performed to understand the chemical and microstructure of the unmodified and CCC films.

An x-ray photoelectron spectroscopy (XPS) analysis of the CCC films on aluminum supports the sol-gel formation of chromium hydroxide on the surface. All spectra were recorded after a 10-min argon-ion gun etch (5 keV) to remove any adven-

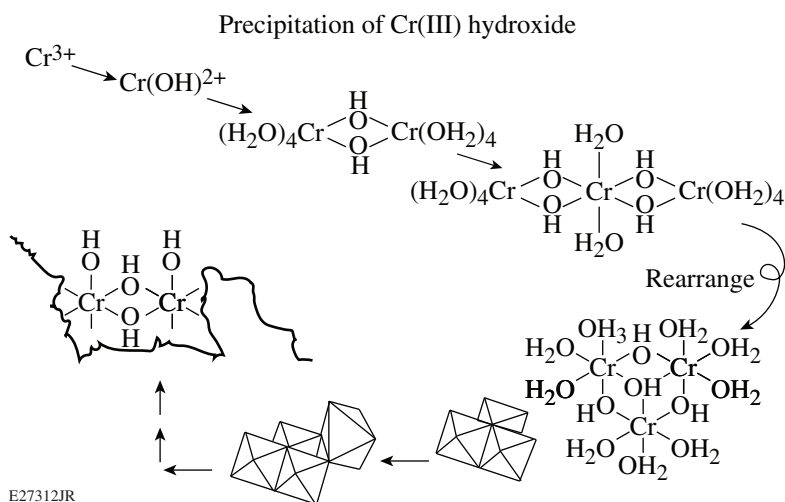
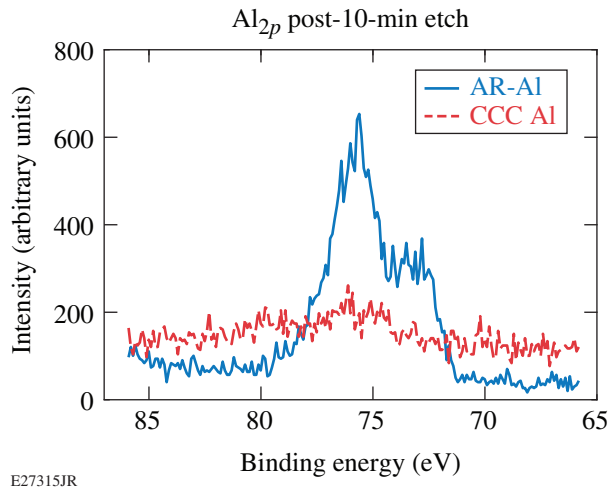


Figure 155.10  
Schematic representation of chromium hydroxide [Cr(III)] precipitation and subsequent binding to the target substrate. (Reprinted with permission from The Electrochemical Society.<sup>7</sup>)

E27312JR

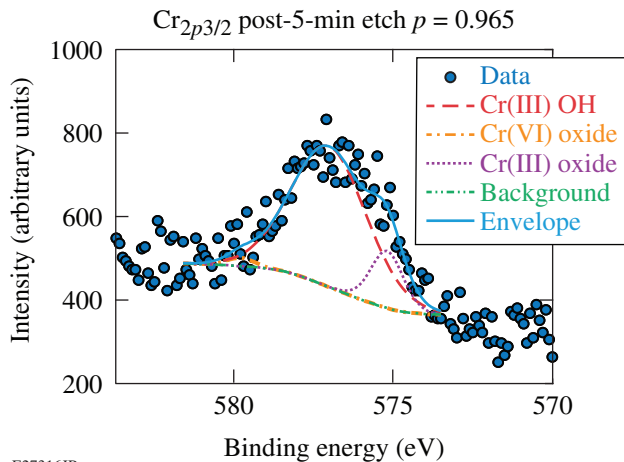
titious carbon species on the surface. Figure 155.11 shows the  $Al_{2p}$  spectrum for both the unmodified aluminum and the CCC aluminum samples. The data suggest that complete coverage was achieved on the CCC films, indicated by the lack of aluminum binding states present on the surface of the sample. The  $Cr_{2p3/2}$  spectrum of the CCC films on aluminum, shown in Fig. 155.12, revealed several chromium species in the layer.



E27315JR

Figure 155.11

X-ray photoelectron spectroscopy (XPS) spectra of unmodified aluminum [Ar-Al] (blue) and chromate-conversion-coating (CCC) [CCC Al] films on aluminum (red). No appreciable amounts of aluminum are present in the CCC films, indicating complete conversion.



E27316JR

Figure 155.12

$Cr_{2p3/2}$  spectrum of the CCC films on aluminum. Raw data (circles) and fits (colored lines) indicate the binding states found on the surfaces. The decomposition of the photoelectron peak indicates several chromium species present on the surface of the CCC aluminum. The  $p$  value for the envelope fit was determined to be 0.965.

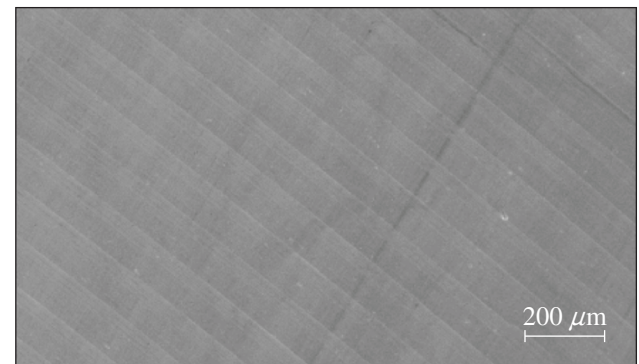
Using the peak fitting software CasaXPS, a fitting routine was used to decompose the  $Cr_{2p3/2}$  photoelectron peak. The results of the fitting routine are shown in Table 155.I.

Table 155.I:  $Cr_{2p3/2}$  fit results obtained from the fitting routine using CasaXPS.

Species	Area (%)	Mean Energy (eV)
Cr(III) OH	88.7	577.1
Cr(III) oxide	14.5	579.8
Cr(IV) oxide	1.76	575.2

The results of the  $Cr_{2p3/2}$  fit also support the sol-gel formation because of the large quantities of chromium hydroxide present in the CCC film along with small amounts of Cr(III) oxide and Cr(VI) oxide.

The CCC film process on aluminum significantly altered the microstructure compared to unmodified samples. The scanning electron microscope (SEM) micrograph for unmodified aluminum is shown in Fig. 155.13. The only extraordinary features stem from the machining process and are apparent at the 200- $\mu$ m scale. No smaller features were visible. These films contain large quantities of fractures and cracks likely caused by the collapse of the polymeric network during air drying of the films.



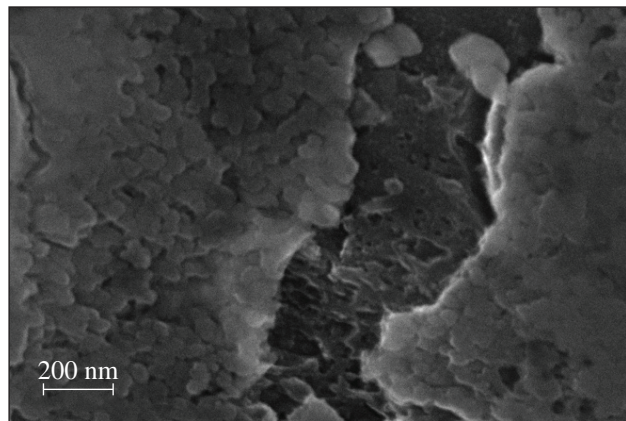
E27708JR

Figure 155.13

Scanning electron microscopy (SEM) micrograph of unmodified aluminum, where machine markings are apparent at the 200- $\mu$ m scale with 20-kV accelerating voltage, 17.5-mm working distance, and 23 $\times$  magnification.

A detailed view of the CCC aluminum sample is shown in Fig. 155.14. The highly grained structure is quite apparent at higher magnification. The grain size of the chromium

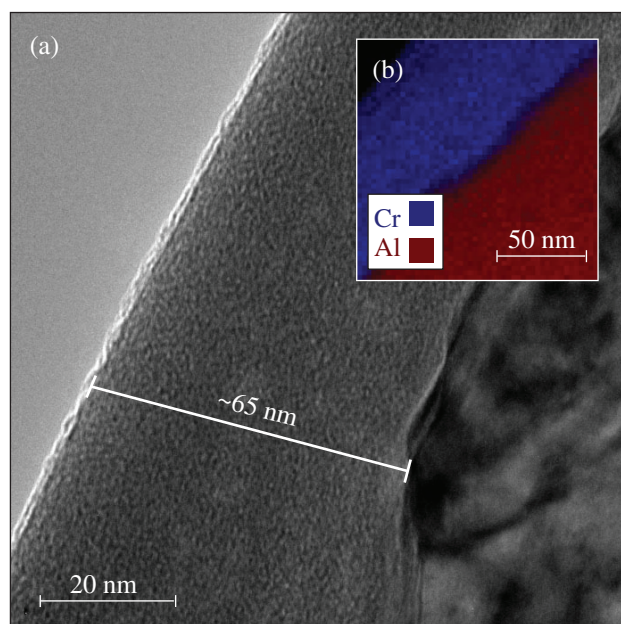
hydroxide is of the order of 50 to 100 nm, while the dislocation fracture is  $\sim 300$  nm. To obtain a better understanding of the microstructure, a cross-section sample was prepared for transmission electron microscopy (TEM) analysis. The results in Fig. 155.15 show that the CCC layer is, on average, 65 nm



E27709JR

Figure 155.14

A detailed view of a pit present in the CCC film on aluminum. The scale bar indicates a 200-nm scale with 20-kV accelerating voltage, 5.8-mm working distance, and 59.13 $\times$  magnification. The highly grained structure of the CCC films on aluminum is apparent at this scale.



E27357JR

Figure 155.15

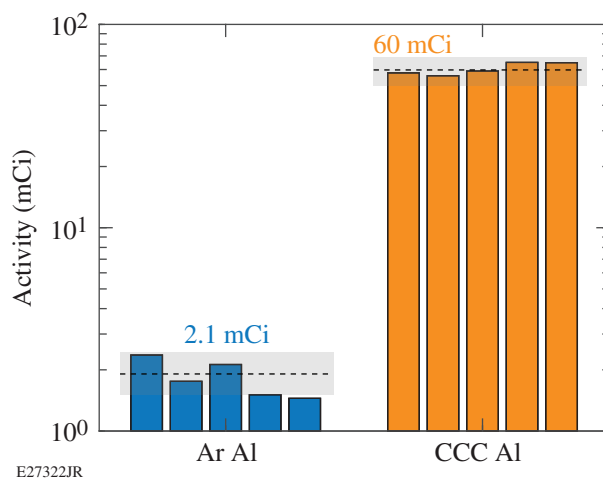
TEM cross section of the CCC film on aluminum on a 20-nm scale. The porous nature can be inferred from highly grained film. Inset: STEM x-ray map of the CCC film, where both chromium (blue) and aluminum (red) species are shown.

thick. This was visually apparent and also confirmed with the scanning transmission electron microscopy (STEM) x-ray map shown in Fig. 155.15.

The chemistry and microstructure of the CCC samples indicate a stark difference between the unmodified and modified aluminum samples; however, the impact these differences have on tritium retention is unconfirmed. To determine the impact, samples were charged with tritium by exposure to a deuterium-tritium (DT) gas mixture at 25°C for 24 h. After exposure, the samples were stored in separate metal containers under a dry helium atmosphere until retrieved for an experiment.

### Results and Discussion

The tritium-charged samples were subjected to one of two treatments: thermal desorption or a surface-stripping wash. In the first treatment, samples were subjected to temperature-programmed thermal desorption (TPD) to thermally remove and measure the total quantity of tritium retained by the metal sample. Tritium was collected as tritiated water in bubblers attached to the furnace. The activity was measured by scintillation counting using a PerkinElmer Tri-Carb 2910 TR liquid scintillation counter. The results of the TPD experiments for both the unmodified and CCC samples are shown in Fig. 155.16.



E27322JR

Figure 155.16

Total activity measured with temperature-programmed thermal desorption (TPD) on a semi-log plot. Each bar represents an individual sample; the bars are grouped by surface finish unmodified aluminum (blue) and CCC Al (orange). The mean of each group is shown as a dashed line, with the error plotted between the shaded regions.

The TPD results indicate that, on average, the unmodified aluminum samples retained a total of 2.1 mCi. While the total activity in the aluminum samples was lower than expected, the CCC aluminum retained 60 mCi. This large difference reveals that the CCC samples retained 30× more tritium than the unmodified counterpart. This increase cannot be explained by a purely diffusive argument and most likely stems from the large quantities of hydrated chromium hydroxide and the surface defects observed with XPS and SEM/TEM, respectively.

In the second treatment, samples were washed in 75 mL of a 15% surfactant solution for 5 min. In this solution, tritium on and in the near surface of the metal is expected to be removed from the metal. The activity in the resulting solution was measured using liquid scintillation counting to give the total quantity of surface/near-surface tritium removed during the wash. The results of the surface washes are shown in Fig. 155.17.

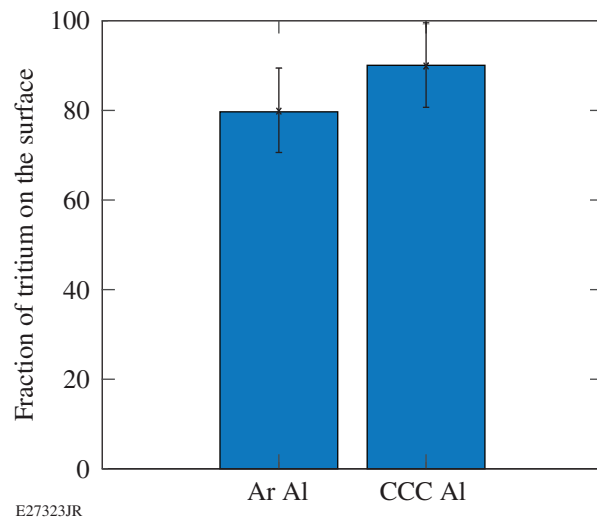


Figure 155.17 The fraction of tritium residing on the surface of the unmodified aluminum (Ar Al) and the CCC aluminum (CCC Al) samples. The resulting surface concentrations of 0.8 Ci/cm<sup>3</sup> and 0.4 Ci/cm<sup>3</sup> were found for unmodified aluminum and CCC aluminum, respectively.

It was found that >75% of the tritium resides on and in the surface of both unmodified aluminum and CCC aluminum. Taking the total quantity removed in thermal desorption and subtracting the quantity of tritium found on and in the near surface, the partitioning of tritium between the surface and bulk of both unmodified aluminum and the CCC samples is shown in Table 155.II.

Table 155.II: Partitioning of tritium between surface and bulk of unmodified aluminum and CCC aluminum. All values are reported as mCi of tritium.

Sample	Surface	Bulk	Total
Unmodified Al	1.7	0.4	2.1
CCC Al	53	7	60

Under the exposure conditions and using the literature diffusivity of aluminum<sup>2</sup> at a room temperature of 7.95 × 10<sup>-12</sup> m<sup>2</sup>s<sup>-1</sup>, an unmodified aluminum sample is expected to reach equilibrium with a tritium inventory of 2.5 mCi. The measured tritium inventory is sevenfold shy of the expected equilibrium value, hinting that the concentration profile in the samples has not reached an equilibrium state. Additionally, for these experimental conditions, the Fourier number ( $\phi$ ) suggests that the system is in the transition regime, where a time-dependent analysis is acceptable. The Fourier number is given in Eq. (1), where  $x$  is the thickness of the sample,  $D$  is the diffusivity, and  $t$  is time:

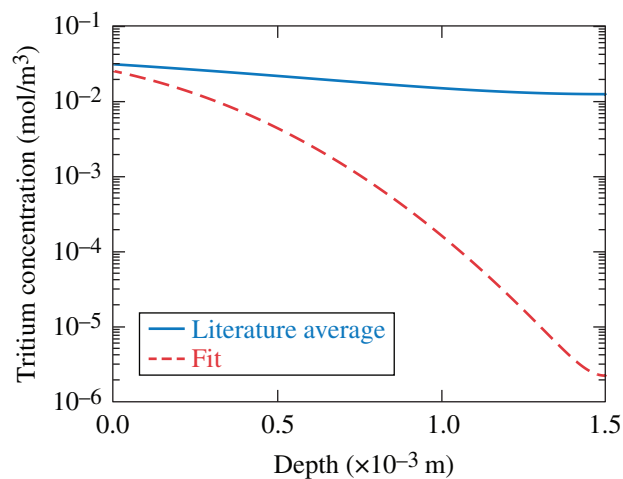
$$\phi = \frac{x^2}{Dt}. \quad (1)$$

Using the literature diffusivity and solubility values,<sup>2</sup> the concentration profile for the unmodified aluminum samples is obtained from the solution to the semi-infinite diffusion equation.<sup>8</sup> The concentration profile  $c(x,t)$  is given by

$$c(x,t) = c_0 + (c_\infty - c_0) \operatorname{erf}\left(\frac{x}{\sqrt{4Dt}}\right), \quad (2)$$

where  $c_0$  is the solubility ( $S$ ) in the near surface of the material,  $D$  is the diffusivity, and  $t$  is the time the diffusion process takes place. This equation was solved using the published values for  $D$  and  $S$  to yield the blue concentration profile shown in Fig. 155.17. The integral of this profile through the depth of the sample yields 2.5 mCi of total tritium in the bulk.

The concentration profile was also determined using the inventory obtained in the thermal desorption experiment. In this calculation, the  $D \times S$  product was varied until the integral of the concentration profile matched the experimental values. The result of this calculation is also shown in Fig. 155.18. The  $D \times S$  product for the fit needed to be lowered by a factor of 0.15 to match the measured bulk tritium inventory. It is noteworthy that the modified diffusivity–solubility product for the fit is still within the range of reported literature values.



E27383JR

Figure 155.18

The concentration profiles for the literature  $D$  and  $S$  values (blue) and the fit values (red) for aluminum 6061 on a double log plot. The  $D \times S$  product for the fit was lowered by a factor of 0.15. The integral of the blue and red curves yields 2.5 mCi and 2.1 mCi, respectively.

### Conclusions

Chromate-conversion coatings significantly alter the chemistry and microstructure of aluminum alloy by fully converting the aluminum surface to a cracked hydrated chromium hydroxide layer. Also, the CCC films allow for enhanced tritium uptake compared to unmodified aluminum. Most of the tritium retained in the CCC samples resides on the surface, indicating the importance of the surface in the tritium adsorption process and subsequent retention. The high quantities of tritium in all areas of the CCC samples indicated these films are not suited for applications where exposure to tritium is possible.

### ACKNOWLEDGMENT

This material is based upon work supported by the Department of Energy National Nuclear Security Administration under Award Number DE-NA0001944, the University of Rochester, and the New York State Energy Research and Development Authority. The support of DOE does not constitute an endorsement by DOE of the views expressed here.

### REFERENCES

1. C. Fagan, M. Sharpe, W. T. Shmayda, and W. U. Schröder, *Fusion Sci. Technol.* **71**, 275 (2017).
2. M. Sharpe, W. T. Shmayda, and W. U. Schröder, *Fusion Sci. Technol.* **70**, 97 (2016).
3. T. Hirabayashi, M. Saeki, and E. Tachikawa, *J. Nucl. Mater.* **127**, 187 (1985).
4. R.-D. Penzhorn *et al.*, *Fusion Sci. Technol.* **64**, 45 (2013).
5. J. H. Osborne, *Prog. Org. Coat.* **41**, 280 (2001).
6. P. L. Hagans and C. M. Haas, in *ASM Handbook*, edited by C. M. Cotell, J. A. Sprague, and F. A. Smidt, Jr. (ASM International, Materials Park, OH, 1994), Vol. 5, pp. 405–411.
7. M. W. Kendig and R. G. Buchheit, *Corrosion* **59**, 379 (2003).
8. J. Crank, *The Mathematics of Diffusion* (Oxford University Press, Oxford, 1979).

---

# Simulation of Grating-Compressor Misalignment Tolerances and Mitigation Strategies for Chirped-Pulse-Amplification Systems of Varying Bandwidth and Beam Size

## Introduction

For more than 30 years, chirped-pulse amplification (CPA) has made it possible to amplify picosecond and femtosecond pulses to high energy by circumventing the damage threshold limitations of direct amplification via pulse stretching and compression.<sup>1</sup> CPA has found wide application in a variety of laser amplifier technologies including fiber, solid-state, gas, excimer, mixed-bulk glasses, and optical parametric amplifiers. These technologies are integrated into CPA systems ranging in peak powers from gigawatt (GW) (Ref. 2) to petawatt (PW) (Ref. 3). The peak power of a CPA system is constrained to some degree by the choice of amplifier technology. The pulse duration is limited by the bandwidth of the medium, and the size/geometry of the medium can impose limits on energy scaling.

Diffraction gratings are by far the most common elements used to stretch and compress pulses because of their substantial angular dispersion, where pulse-stretching factors typically range from 1000 to 100,000. These gratings typically function in pairs, where the first diffraction grating spreads the bandwidth in space and the second grating cancels the angular dispersion of the first, consequently introducing group-delay dispersion (GDD) from the wavelength-dependent variation of path length. If the second grating is not perfectly parallel to the first grating, the residual angular dispersion can cause errors in pulse compression and focusability, impacting the spatiotemporal shape of the pulse and reducing the overall focused intensity.

The three primary effects of angular dispersion are increased beam divergence affecting the minimum focused spot size, tilt of the pulse front, and errors in chirp or spectral dispersion affecting the pulse duration.<sup>4</sup> These and other more-subtle effects complicate the calculation of grating-alignment tolerances for many systems,<sup>5–7</sup> where individualized time-intensive simulations are required to determine alignment sensitivity for a particular CPA system. Depending on system specifications and desired performance, grating-alignment tolerances may necessitate the use of high-performance or specialized mounting hardware for stability and alignment precision. An understanding of how grating-alignment tolerances

scale with CPA parameters such as bandwidth and beam size can provide early determination of whether intensive simulation or specialized mounting hardware may be required for a particular system, which may affect project budget, resources, or time line.

In this work, compressor grating-alignment sensitivity is compared for CPA systems ranging in Fourier transform-limited (FTL) pulse duration from 10 fs to 1 ps and for beam sizes from 10 mm to 300 mm. Grating-tilt-alignment tolerances are defined and simulated for varying compressor groove density from 900 to 2000 gr/mm and for all possible incident angles. To our knowledge, this is the first time that grating-alignment tolerances have been specified plainly over such a broad range of parameters. These tolerances serve as guidelines to indicate which combinations of bandwidth, beam size, groove density, and incident angle are most sensitive to misalignment. Techniques for compensating grating-misalignment errors are simulated, and limitations are identified for broad bandwidth, affecting intensity and temporal contrast.

## Effects of Grating Misalignment on Pulse Compression

Each grating in a stretcher or compressor must be aligned in three dimensions: tilt, tip, and in-plane rotation (IPR) (Fig. 155.19). Generally, the incident and diffracted rays have a component in the plane of diffraction and the plane of reflection. In a perfectly aligned compressor, where grating pairs have parallel surfaces and grooves, the incident and diffracted rays lie solely in the  $x$ - $z$  plane with no component in the reflection plane ( $y$ - $z$  plane). Grating-tilt misalignment changes the incident/diffracted angles, but the plane of diffraction remains coplanar with the  $x$ - $z$  plane. Tilt error of one grating in a pair causes angular dispersion in the  $x$ - $z$  plane at the compressor output. Tip and IPR misalignment produces a nonzero component in the reflection plane and effectively rotates the plane of diffraction with respect to the plane of incidence. Rotation of the diffraction plane creates a component of residual angular dispersion, which is perpendicular to the  $x$ - $z$  plane. Angular dispersion produced by any misalignments has a temporal and spatial effect on the compressor output.

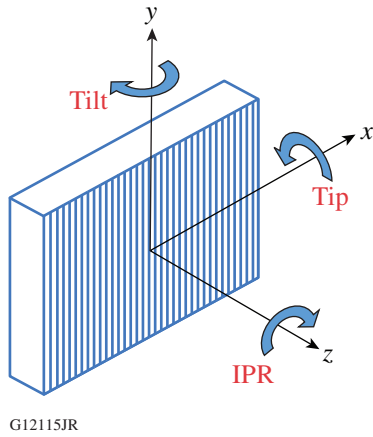


Figure 155.19  
Definition of grating-alignment parameters and axes. IPR: in-plane rotation.

In the time domain, angular dispersion from a misaligned grating compressor causes a tilt of the pulse front or an inhomogeneous wave so that one edge of the beam is delayed with respect to the other.<sup>8</sup> If the beam is sampled locally, the pulse duration will appear short; however, the spatially integrated pulse duration and the duration of illumination at the focal plane are much longer because of the pulse-front delay.<sup>6</sup> In addition, grating misalignment changes the path length of each wavelength component so that the total system GDD is no longer minimized. This GDD mismatch can also vary spatially across the beam, degrading the spatiotemporal quality of the compressed pulse.

In the spatial domain, residual angular dispersion from a misaligned grating pair affects focusability because of increasing beam divergence. This causes an elongation of the minimum spot size in the direction of the angular dispersion error. Tilt error exhibits spot elongation purely in the horizontal ( $x$ - $z$ ) plane, while tip and IPR add a vertical elongation from slight rotation of the diffraction plane out of the horizontal plane.

Other effects to consider are finite beam size, lateral frequency shift, higher-order dispersion, and grating astigmatism.<sup>5,9</sup> Many models neglect the effect of beam divergence or free-space diffraction, but these effects are not trivial for large bandwidths, small waists, and beam collimation errors. Diverging rays from free-space diffraction take a slightly different path through a grating pair and can contribute to spatial variations in chirp across the beam. For large bandwidth, the beam waist, and therefore the divergence angle, is wavelength dependent, further complicating calculation of these effects.

For the case of narrow bandwidth and for a compressor beam size that is much larger than the spatial extent of the pulse

duration, there is a convenient, simple analytical expression that describes broadening of the pulse duration at the focal plane resulting from pulse-front tilt (PFT):<sup>8,10</sup>

$$\Delta\tau = D \frac{N\lambda_0}{c} \frac{\tan(\beta_0)}{\cos(\alpha)} \epsilon_x, \quad (1)$$

$$\tau = \sqrt{\tau_0^2 + (u\Delta\tau)^2}. \quad (2)$$

The equation for pulse duration increase  $\Delta\tau$  is linear with compressor beam size  $D$  and grating tilt error  $\epsilon_x$ , where  $N$  is the grating groove density,  $\alpha$  is the incident angle, and  $\beta_0$  is the diffracted angle for the center wavelength  $\lambda_0$ . The total pulse duration at focus  $\tau$  is the root square sum of the FTL pulse duration  $\tau_0$  and PFT broadening  $\Delta\tau$ , where  $u$  is the conversion factor from  $1/e^2$  to full-width-at-half-maximum (FWHM) duration.

Simulations in *FRED*, a beam propagation software by Photon Engineering<sup>11</sup> (solid lines in Fig. 155.20), closely match the analytical expression [Eq. (2)] for PFT with a 300-mm

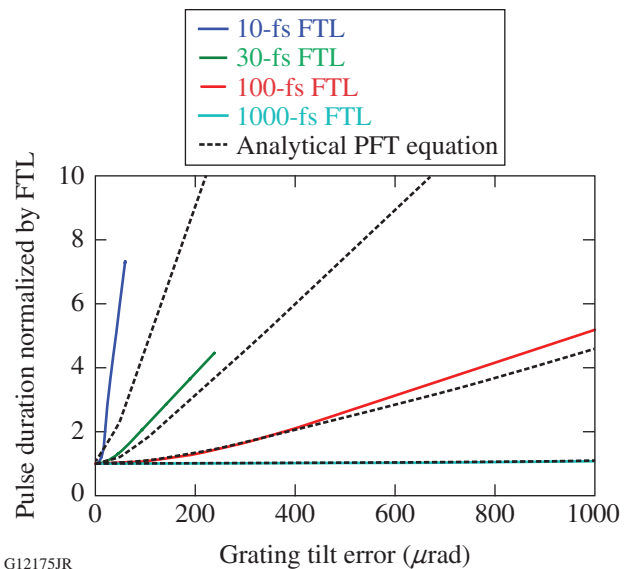


Figure 155.20  
The solid lines are simulations of the pulse-duration increase because of grating tilt for several different Fourier transform–limited (FTL) pulse durations (i.e., bandwidth) in a 300-mm-diam compressor beam. The dashed lines follow the analytical solution [Eq. (1)] for pulse-duration increase caused by pulse-front tilt (PFT), valid for narrow bandwidth and cases where beam size is much larger than the spatial extent of the pulse duration.<sup>8</sup> Simulations here are for 900-nm center wavelength, 1285-gr/mm grating groove density, 51° incident angle, and 300-mm compressor beam diameter.

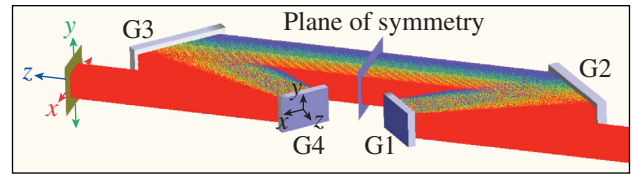
compressor beam size in the case of a 1000-fs pulse duration. For larger bandwidth (i.e., shorter FTL pulse duration) and grating-tilt error, however, the accuracy of Eq. (2) degrades. Large-bandwidth compressors must also consider the effect of spectral chirp and other higher-order effects that are wavelength dependent.

The combination of multiple space–time effects make calculation problematic, and in many cases complex simulations utilizing ray-tracing or beam propagation software are required. Calculations are more accurate when modeling software takes into account relative contributions from multiple space–time effects as well as free-space diffraction.<sup>5</sup> One goal of this work, discussed in **Scaling of Compressor Alignment Tolerances for CPA Systems with Bandwidth, Energy, and Compressor Geometry** (p. 146), is to define the limits where a higher level of analysis is required.

### Simulation of Grating Compressor Sensitivity for a 0.5-PW OPCPA System

To illustrate the relative alignment sensitivity between tilt, tip, and IPR for a four-grating compressor (Fig. 155.21), a *FRED*–*MATLAB* model<sup>12</sup> is used to simulate alignment sensitivity for the 0.5-PW MTW OPAL (Multi-Terawatt optical parametric amplifier line), 15-fs optical parametric CPA (OPCPA) system.<sup>13</sup> Originally this simulation code was developed for compressor simulations on OMEGA EP.<sup>14</sup>

The compressor model (Fig. 155.21) propagates Gaussian beamlets through gratings and other optics, recording the spatial ( $x, y$ ) and spectral ( $\omega$ ) amplitude and phase in a 3-D



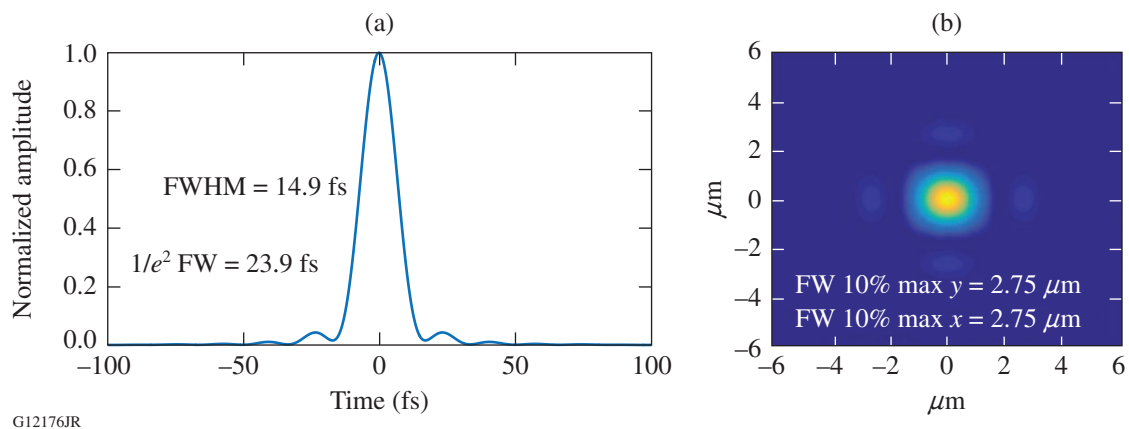
E26970JR

Figure 155.21

*FRED* model of a four-grating (G1–G4) pulse compressor. Optionally, a single grating pair can be used by placing a vertical roof mirror at the plane of symmetry.

complex matrix. Next, a *MATLAB*<sup>15</sup> postprocessor computes the integrated near-field and far-field beam profiles and pulse durations from this 3-D matrix (Fig. 155.22). The previous steps are repeated for a range of grating misalignments. Tolerances for pulse duration and/or focused spot size can be determined from alignment sensitivity plots (Fig. 155.23).

The pulse duration increases most dramatically with tilt error from the second and third gratings (Fig. 155.23). Because the beam and spectrum are spread across this grating, there is a larger amount of induced GDD error with misalignment compared to the first (and fourth) grating. Assuming that misalignments occur slowly over time (i.e., no significant high-frequency pointing errors from vibration), the grating distance can be adjusted to compensate for some of the extra GDD error so that the alignment sensitivity of the second (and third) grating nearly matches the first (and fourth) grating. Compensation of grating misalignment will be discussed in **Mitigation Strategies for the Effects of Grating Misalignment in Pulse Compressors and Their Limitations** (p. 150). The alignment



G12176JR

Figure 155.22

Results of a simulation using the *FRED* beam-propagation model and *MATLAB* postprocessor: (a) the spatially integrated far-field pulse duration and (b) the temporally integrated focused spot size.

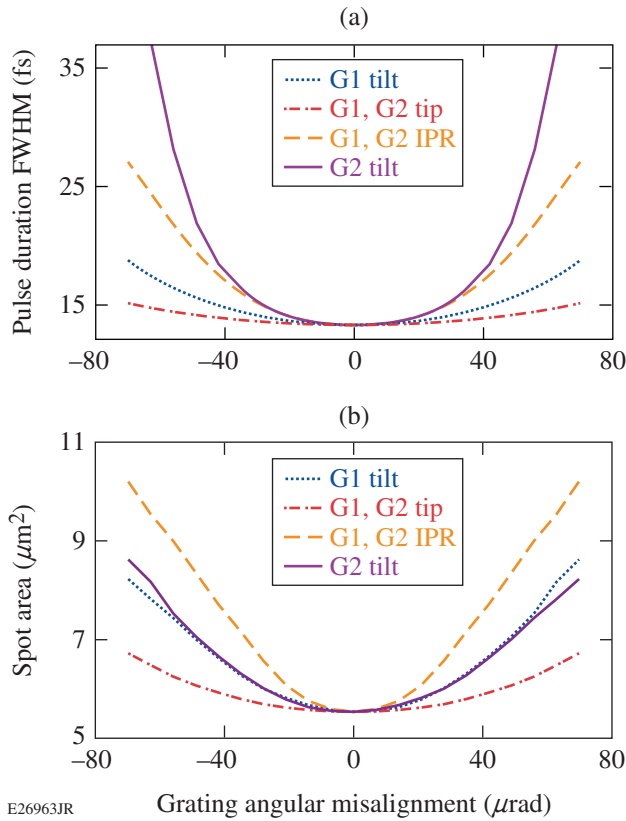


Figure 155.23 Simulated far-field (a) pulse duration FWHM and (b) spot area full-width (FW) 10% of max for the 0.5-PW Multi-Terawatt optical parametric amplifier line (MTW OPAL) optical parametric chirped-pulse–amplification (OPCPA) system at LLE.<sup>13</sup> Only one type of error (tilt, tip, or IPR) is applied at a time to each grating, while the grating separation remains fixed. MTW OPAL output specifications: 15-fs pulses centered at 900 nm, 90-mm compressor beam diameter, 50° grating incident angle, and 1285 gr/mm.

sensitivity of both tip and the IPR is similar in magnitude to tilt but their relative sensitivity is strongly dependent on the compressor parameters and will be presented in greater detail.

**Scaling of Compressor Alignment Tolerances for CPA Systems with Bandwidth, Energy, and Compressor Geometry**

1. Bandwidth and Energy Scaling of Grating-Tilt Tolerances  
 CPA systems can be generally classified in terms of peak power. While grating-alignment sensitivity is not directly influenced by peak power, energy and pulse duration can be transformed into parameters that directly affect the grating-alignment sensitivity.

The FTL pulse duration is inversely proportional to the bandwidth of a CPA system, where increasing bandwidth expands the spread of angular dispersion, increasing pulse duration and

focused spot size. The compressor beam size is another parameter that is known to have a direct effect on grating-alignment sensitivity.<sup>8</sup> The beam size in a compressor is regulated by the laser-induced damage threshold (0.2 to 0.3 J/cm<sup>2</sup> for gold<sup>16</sup> and 1 to 2 J/cm<sup>2</sup> for dielectric<sup>17</sup>) and therefore can be loosely transformed into energy.

The parameters of bandwidth and beam size provide a framework with which to describe grating-alignment sensitivity and tolerances. Common CPA system amplifier technologies are mapped into this space (Fig. 155.24) in order to approximate alignment tolerances generally for these classes of systems [Fig. 155.25(a)].

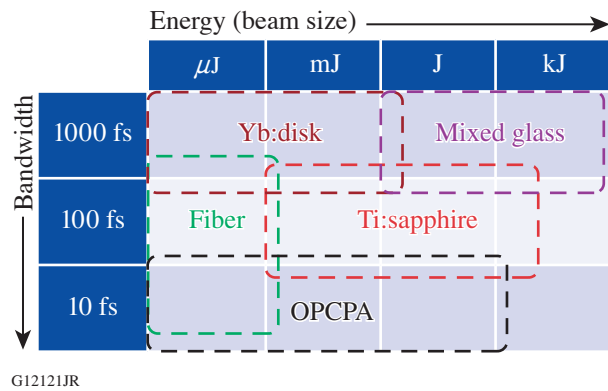


Figure 155.24 Framework for mapping several mainstream chirped-pulse–amplification (CPA) technologies in terms of bandwidth and compressor beam size.

The *FRED–MATLAB* model described earlier was adapted for altering beam sizes and pulse bandwidths in order to simulate how grating-tilt–alignment tolerances scale with compressor beam size and transform-limited pulse duration. Other compressor parameters such as the 900-nm center wavelength, 50° grating incident angle, groove density of 1285 mm<sup>-1</sup>, and 1.2-m grating separation (GDD of ~6 × 10<sup>6</sup> fs<sup>2</sup>) remain constant. The compressor beam size is varied from 10 mm to 300 mm and the FTL pulse duration is varied from 10 fs to 1 ps [Fig. 155.25(b)]. While only tilt tolerances are specified from this study, relative tip and IPR tolerances can be predicted and will be discussed in **Mitigation Strategies for the Effects of Grating Misalignment in Pulse Compressors and Their Limitations** (p. 150).

A somewhat arbitrary tolerance is defined for a  $\sqrt{2}$  factor drop in intensity compared to a FTL duration and diffraction-limited (DL) spot area:

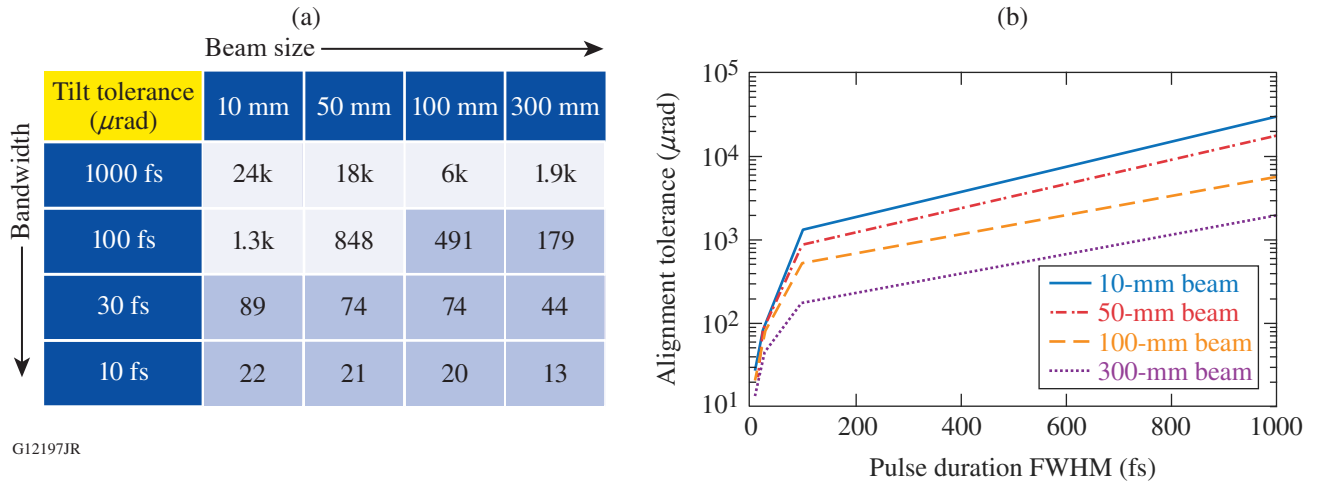


Figure 155.25

(a) Second grating-tilt-alignment tolerances for FTL pulse duration and compressor beam size (matching Fig. 155.24); the light-blue shaded region shows tilt-alignment tolerances  $<500 \mu\text{rad}$ . (b) Plot of the same tilt-alignment tolerances with pulse duration for multiple beam sizes in a four-grating compressor with a 900-nm center wavelength and 1285-gr/mm gratings separated by 1.2 m. Tolerances are based on an intensity reduction by a factor of  $\sqrt{2}$  as a result of space-time pulse aberrations.

$$I_{\text{tolerance}} = \frac{I_{\text{max}}}{\sqrt{2}}. \quad (3)$$

Since intensity is inversely proportional to pulse duration and spot area, the tolerance is reached when the normalized product of pulse duration and spot area is equal to  $\sqrt{2}$ :

$$\frac{\tau}{\tau_{\text{FTL}}} \cdot \frac{A}{A_{\text{DL}}} = \sqrt{2}. \quad (4)$$

This tolerance definition takes into account increases in both pulse duration and spot size for applications where intensity on target is critical.

Since grating-alignment tolerances are highly dependent on bandwidth and compressor beam size, tolerances can be specified in this framework and broadly applied to various CPA system classes (Figs. 155.24 and 155.25). Tolerance estimations provide useful information about feasibility and effort level or resources required for compressor design and construction.

## 2. Grating Groove Density and Incident Angle Scaling of Grating-Tilt Tolerances

In addition to bandwidth and compressor beam size, grating-alignment tolerances will depend on other parameters, such as grating groove density, grating separation, wavelength, incident/diffracted angles, and application requirements (e.g., pulse duration, spot size, or intensity).

After selecting a tolerance from Fig. 155.25 for a particular bandwidth and beam size, it is important to determine how this tolerance scales with groove density and incident angle for a particular compressor geometry. When designing a compressor, there are various suitable combinations of incident/diffracted angle and grating groove densities, which can be selected based on desired dispersion profiles, size constraints, alignment sensitivity, diffraction efficiency, etc. Incident and diffracted angle ranges for each groove density option are limited by the physical size of beams (including the spread of the bandwidth in space), real diffraction angles from the grating equation, grating-size constraints, and grating separation (i.e., magnitude of GDD required for compression of the stretched pulse).

For example, the angle between the incident and diffracted beams near Littrow is limited for real beams by

$$\alpha > \beta_r + \sin^{-1} \left[ \frac{D \cos \beta_r}{G} \right] \quad \text{for } \alpha > \theta_{\text{Littrow}}, \quad (5)$$

$$\alpha < \beta_b - \sin^{-1} \left[ \frac{D \cos \beta_b}{G} \right] \quad \text{for } \alpha < \theta_{\text{Littrow}}, \quad (6)$$

where  $\alpha$  is the incident angle,  $\beta_{r/b}$  is the diffracted angle for the wavelengths at the red and blue edges of the bandwidth,  $D$  is the compressor  $1/e^2$  beam diameter,  $G$  is the perpendicular grating separation, and  $\theta_{\text{Littrow}}$  is the angle at which the dif-

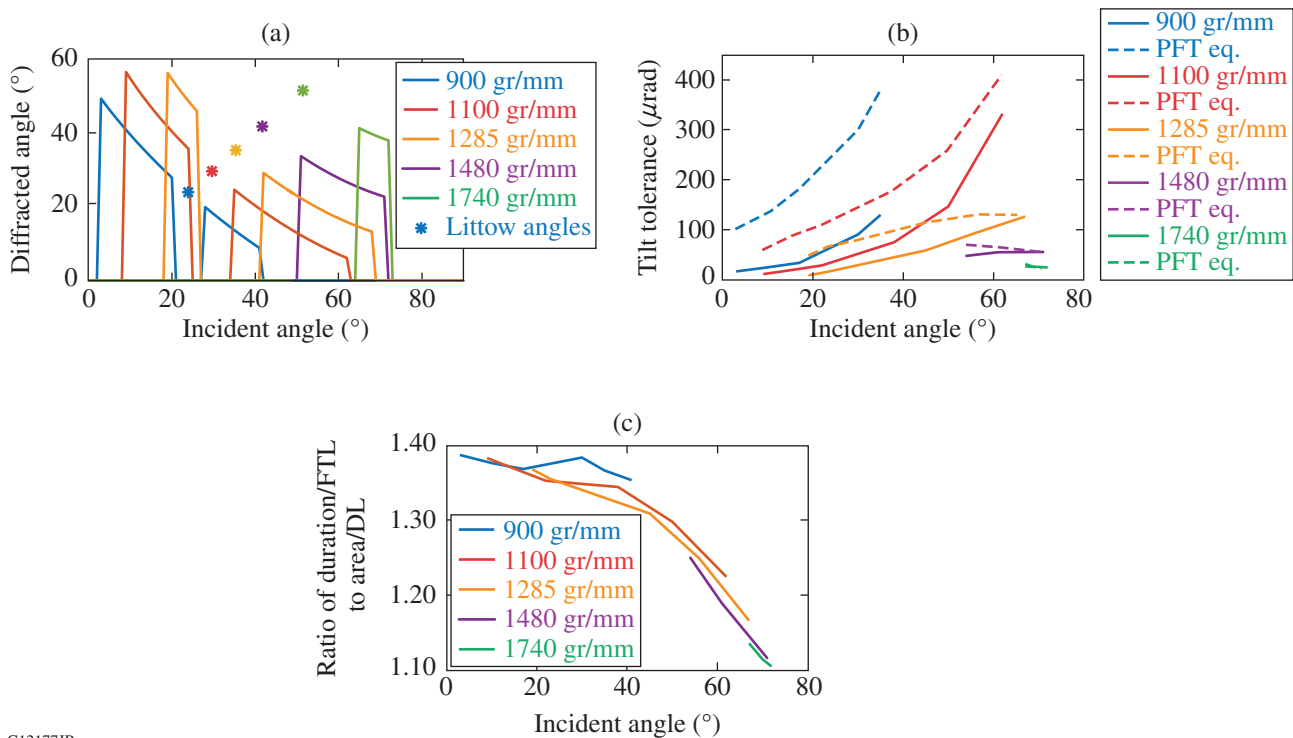
fracted angle for the center wavelength and the incident angle are equal.

Figure 155.26(a) shows all possible diffraction and incident angles for several common groove densities based on a 100-mm compressor beam size with a 180-nm “full-width” bandwidth (30-fs FTL), assuming a GDD of  $6 \times 10^6 \text{ fs}^2$  and a maximum grating width of 600 mm.

Grating-tilt tolerances [defined by Eq. (4)] were simulated for a four-grating compressor using the *FRED-MATLAB* model for 23 combinations of grating groove densities and incident angles [spread over the ranges shown in Fig. 155.26(a)] for a fixed bandwidth of 30-fs FTL and 100-mm compressor beam size. The simulated tilt tolerances for the second grating [solid lines in Fig. 155.26(b)] are compared to estimated tolerances based on Eq. (1) for PFT [dashed lines in Fig. 155.26(b)]. The

differences between the PFT approximation tolerances and the simulated tolerances in Fig. 155.26(b) are primarily caused by the temporal chirp effect from the 30-fs FTL bandwidth since the PFT approximation does not include the local pulse broadening from GDD, nor does it explicitly include the far-field intensity reduction from the elongated focal spot. The breakdown of the PFT approximation with increasing tilt error and bandwidth is shown earlier in Fig. 155.20.

Since the tolerances are defined by Eq. (4), the ratio of the normalized pulse duration to the normalized spot area [Fig. 155.26(c)] reveals how relative contributions from temporal or spatial aberrations impact the intensity tolerance [Eq. (3)]. In Fig. 155.26(c) the pulse-to-area ratio is close to  $\sqrt{2}$  for small incident angles, where elongation of the focal spot is nominal. For larger angles of incidence, the relative contribution of the focal-spot area to the tolerance is greater, indicating a larger



G12177JR

Figure 155.26

(a) All possible combinations of diffracted and incident angles are shown for several common grating groove densities, limited by beam size, spectrum, and grating aperture. Diffracted angles are set to zero for all nonphysical combinations near the Littrow angles (also assuming a fixed group delay dispersion of  $6 \times 10^6 \text{ fs}^2$ ) indicated by asterisks. Additionally, large incident angles and diffracted angles are set to zero in cases where beam widths on gratings are  $>600 \text{ mm}$ . (b) Twenty-three tilt-tolerance simulations were performed (solid lines) to analyze grating-tilt-tolerance trends in the range of possible incident angles and groove densities [shown in (a)]. The dashed lines show the tilt tolerance using only the pulse-front-tilt estimation [Eqs. (1) and (2)]. (c) The ratio of pulse duration normalized by the FTL and spot area normalized by the diffraction limit (DL), assuming perfect compressor alignment, is shown for varying incident angle and grating groove density to reveal the relative impact of temporal and spatial aberrations on the intensity tolerance [Eqs. (3) and (4)].

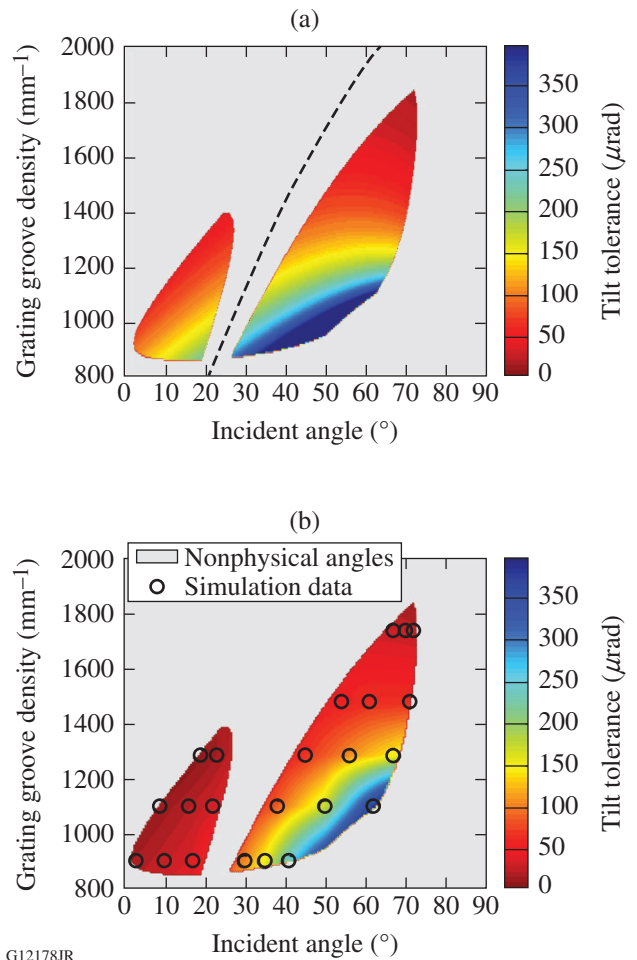
contribution from angular dispersion. This is consistent with further analysis that showed larger temporal shear (group delay) across the near-field beam with incident angle for tilt errors equal to the tolerance limit, and smaller contributions from local GDD. The local GDD was calculated by fitting the spectral phase at the beam center to a polynomial and extracting the second-order coefficient. The pulse-to-area ratio in Fig. 155.26(c) is closer to one for the largest incident angles and grating groove densities, indicating nearly equal contributions of pulse duration and area to the intensity tolerance.

To illustrate tolerance scaling with a high resolution over the full parameter space, Eqs. (1) and (2) were employed to estimate tilt tolerances for groove densities ranging from 800 to 2000 gr/mm and for all possible incident angles [Fig. 155.27(a)]. Figure 155.27(b) shows the simulated data points from Fig. 155.26(b), which have been linearly extrapolated over the entire parameter space.

The white regions in Fig. 155.27 represent nonphysical solutions from either too close a proximity to Littrow [dashed line in Fig. 155.27(a)] or beams that were too large (the grating size was somewhat arbitrarily limited to 600 mm). The dashed line highlighting the Littrow angle separates two types of compressor geometry, where the incident angle is larger than diffracted (right) and vice versa (left). In general, tolerances are much tighter for larger groove densities and smaller incident angles, where compressors with incident angles smaller than diffracted angles are most sensitive to misalignment.

Figures 155.26(b) and 155.27 show how the tilt tolerance for the second and third gratings in a four-grating compressor over a range of incident angles and groove densities are much tighter for a modest 30-fs FTL bandwidth compared to the PFT approximation for narrow bandwidth. The true tilt tolerances can be up to a factor of 4 smaller compared to the approximations from Eq. (1) at low incident angle and groove densities [left side of Fig. 155.26(b) and left island in Fig. 155.27(b)] caused by a strong chirp effect [Fig. 155.26(c)], while tolerances for large incident angle and groove density are nearly equal with the PFT approximation [right side of Fig. 155.26(b) and top of the right island in Fig. 155.27(b)]. Since the tolerances defined by the PFT equation consider only the first-order variation of group delay with beam height, but are closely matching the simulation for large incident angle and groove density, the contribution of PFT dominates in this regime [Fig. 155.26(c)].

In Figs. 155.26(b) (dashed lines) and 155.27(a), the PFT approximation shows an inflection point where the tolerance



G12178JR

Figure 155.27

Variation in the second grating's tilt tolerance with groove density and incident angle for a 30-fs FTL bandwidth and 100-mm compressor beam diameter. Gray areas represent nonphysical combinations of incident angle and groove density [the same assumptions as in Fig. 155.26(a)]. (a) This intensity map was created from Eqs. (1) and (2), considering only the effect of PFT. Two islands of operation are identified for incident angles greater and less than the Littrow angle (dashed line). (b) Simulated data from Fig. 155.26(b) are extrapolated for all incident angles and groove densities, where circles show simulated data points.

is increasing with incident angle for groove density less than  $\sim 1500$  gr/mm, but for larger groove density, the tolerance is decreasing with incident angle. A similar inflection point manifests in the simulation data [Figs. 155.26(b) and 155.27(b) right island] since the PFT and spot area contributions are stronger for larger incident angles in the right island [Fig. 155.26(c)]. Also note the slope of the tilt tolerance contour lines in Fig. 155.27(b) for groove density  $< 1500$  gr/mm is increased compared to Fig. 155.27(a) because of the strength of chirp effects on the pulse duration [Fig. 155.26(c)] for smaller incident angles, pulling down the tolerances in the left island significantly.

As a result of the complexity of effects influencing both the pulse duration and spot size, simulation is critical for larger bandwidth systems to accurately predict alignment tolerances. However, the trends shown in these generalized simulations can aid in estimating grating-alignment tolerances simply over a broad range of parameters suitable for most CPA systems and compressor designs.

### Mitigation Strategies for the Effects of Grating Misalignment in Pulse Compressors and Their Limitations

#### 1. Sources of Alignment Error

Sources of alignment error in grating compressors must be identified in order to assess strategies for mitigating pulse duration and spot-size errors. User error can improve with knowledge and practice of alignment techniques. One common alignment technique<sup>18</sup> reflects an alignment beam at normal incidence from the first grating to remove tip errors; the grating is then rotated to Littrow angle to remove IPR errors. Next, the first grating is rotated to its designated angle of incidence and the process is repeated for all consecutive gratings. The accuracy of these alignment techniques is typically limited by hardware. For example, a grating-tilt axis that is not orthogonal to the  $x$ - $z$  reference plane of the compressor, or motion of this axis (i.e., wobble) in a rotation stage, typically in the range of 10 to 50  $\mu\text{rad}$ , produces tip and IPR errors when rotating each grating from normal to Littrow during alignment. Using two

wavelengths and two Littrow angles that are close together can minimize the wobble error during alignment.<sup>19</sup> Furthermore, the tolerances or resolution of tools and diagnostics such as corner cubes, irises, or cameras may add to alignment error.

Most alignment error stems from the grating mount and associated hardware performance since thermal drift and vibrations can cause slow or fast changes in the alignment. In the most-sensitive compressors, fluctuations resulting from vibration could cause pulse-duration or focal-spot instability. When non-gimbal mounts are used for grating alignment, there is cross coupling between adjustment axes, which complicates alignment.

#### 2. Alignment Error Mitigation Strategies and Limitations

Pulse distortion as a result of grating-tilt errors is caused by a combination of pulse-front tilt and mismatched residual chirp. If these tilt errors are produced on a slow time scale, adjusting the grating separation can compensate for some of the residual chirp to mitigate the effect of pulse broadening. Additionally, finer control or arbitrary shaping of the spectral phase (applied uniformly across the beam) can further shorten the pulse duration to the limit of pulse-front tilt and other higher-order effects [Fig. 155.28(a)]. This is demonstrated via simulation by adjusting the grating separation after misalignment until the pulse duration is minimized. Arbitrary shaping of the dispersion by an acousto-optic programmable dispersive filter (AOPDF)<sup>20</sup> is

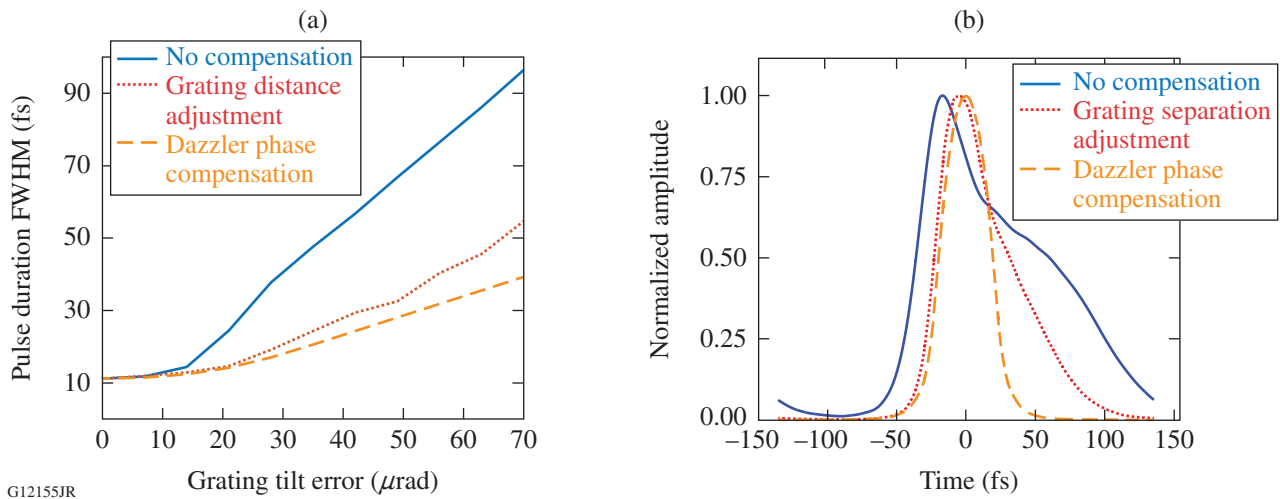


Figure 155.28

Techniques for compensation of residual chirp in the spatially integrated far-field (FF) pulse duration as a result of grating-tilt misalignment of the second grating. (a) Pulse duration is increased from 10-fs FTL with grating-tilt error; (b) shape and duration of the temporal pulse after 70  $\mu\text{rad}$  of second-grating-tilt error are minimized by grating separation optimization and arbitrary shaping of the spectral phase (applied uniformly across the beam spatial profile). Arbitrary shaping of the spectral phase can be accomplished with an acousto-optic programmable dispersive filter (AOPDF), such as a Dazzler by Fastlite.<sup>20</sup>

simulated by subtracting the spatially averaged residual spectral phase across the beam. The asymmetric pulse shapes seen in Fig. 155.28(b) signify the presence of third-order dispersion, which is considerably improved in the case of AOPDF-like control of the spectral phase.

Grating tip and IPR alignment scale in sensitivity similar to tilt alignment with bandwidth and beam size. However, the relative sensitivity between tip and IPR is heavily dependent on the diffracted angle of the center wavelength. The vertical component of angular dispersion induced by tip error in a grating compressor can be represented to the first order by

$$\frac{\partial \phi_y}{\partial \lambda} = \left| 2\epsilon_y N \tan(\beta_0) \right|, \quad (7)$$

where  $N$  is the grating groove density and  $\beta_0$  is the diffracted angle for the center wavelength.<sup>6</sup> Similarly, angular dispersion from IPR error ( $\epsilon_z$ ) in the vertical plane follows

$$\left| \frac{\partial \phi_y}{\partial \lambda} \right| = \left| 2\epsilon_z N \right|. \quad (8)$$

For systems with a narrow bandwidth, setting Eqs. (1) and (2) equal shows the ratio of IPR to tip sensitivity:

$$\left| \frac{\epsilon_z}{\epsilon_y} \right| = \left| \tan(\beta_0) \right|. \quad (9)$$

For diffracted angles of less than  $45^\circ$ , such as the MTW OPAL example in Fig. 155.23, where  $\beta_0 = 22.55^\circ$ , IPR is more sensitive than the tip. Conversely, the compressed pulse duration increases more quickly with tip error for diffracted angles greater than  $45^\circ$ .

The relation in Eq. (9) indicates that a prescribed amount of tip can compensate for IPR error and vice versa.<sup>7</sup> *FRED-MATLAB* simulations searched for the amount of tip needed to optimize the pulse duration after an array of IPR errors and found good agreement with Eq. (9) for a couple of extreme combinations of bandwidth and beam-size variation (Fig. 155.29).

For an ultrabroadband 10-fs FTL pulse, IPR errors up to  $200 \mu\text{rad}$  can be compensated with tip at the expense of a  $<25\%$  increase in pulse duration from FTL [Fig. 155.30(a)]. This increase is  $<15\%$  for a 20-fs pulse and  $<4\%$  for a 30-fs pulse. The pulse shapes in Fig. 155.30(b) have a shape simi-

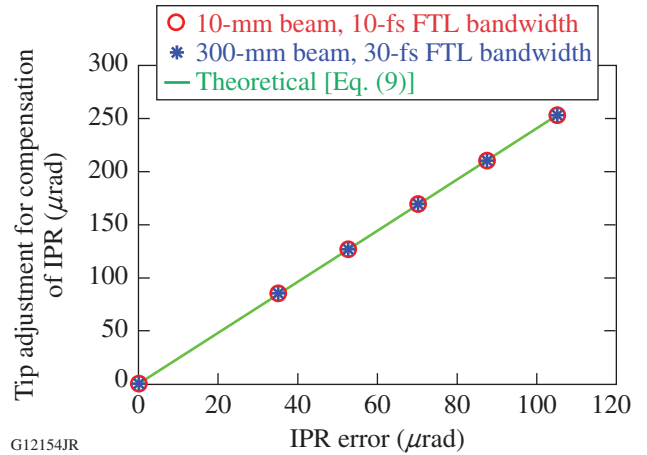


Figure 155.29

Tip angle required to compensate a given IPR error, eliminating first-order vertical angular dispersion. These simulations for two cases of bandwidth and beam size are optimized for shortest pulse duration by adjusting the tip after an IPR error is made on the same grating (markers). Optimized tip adjustments in the simulations are in good agreement with theoretical predictions from Eq. (9) (solid line).

lar to a sinc-squared function as a result of the 20th-order super-Gaussian shape of the spectrum, typical for many ultra-broadband OPCPA systems. In the 10-fs FTL case, degradation of the pulse temporal contrast is observed when compensating larger magnitudes of IPR error with tip adjustment. These pulse shapes appear to contain a residual higher-order phase that varies spatially in magnitude and sign, where residual phase cannot be subtracted out by an AOPDF as in Fig. 155.28.

Tip and IPR errors are practically indistinguishable in small amounts when observing the far-field focal spot because they both cause an increase of the spot size in the vertical direction. For small-bandwidth pulses, reducing the observed vertical dispersion in a grating compressor by partial compensation of tip error with IPR, or vice versa, may be acceptable, depending on pulse contrast requirements. In the case of an ultra-broadband pulse, however, this partial compensation may deleteriously affect pulse shape and contrast, as shown in Fig. 155.30(b). In this case, simultaneous monitoring of the pulse duration and contrast would allow proper optimization of the tip and IPR.

Symmetry can be used to relax alignment tolerances if the gratings can be made large enough to hold a second vertically displaced beam. A four-grating compressor can be folded by placing a roof mirror in the plane of symmetry (Fig. 155.21). The roof mirror vertically inverts the beam for a second pass through the same grating pair, where any vertical angular dispersion or vertical path deviations from the first pass are

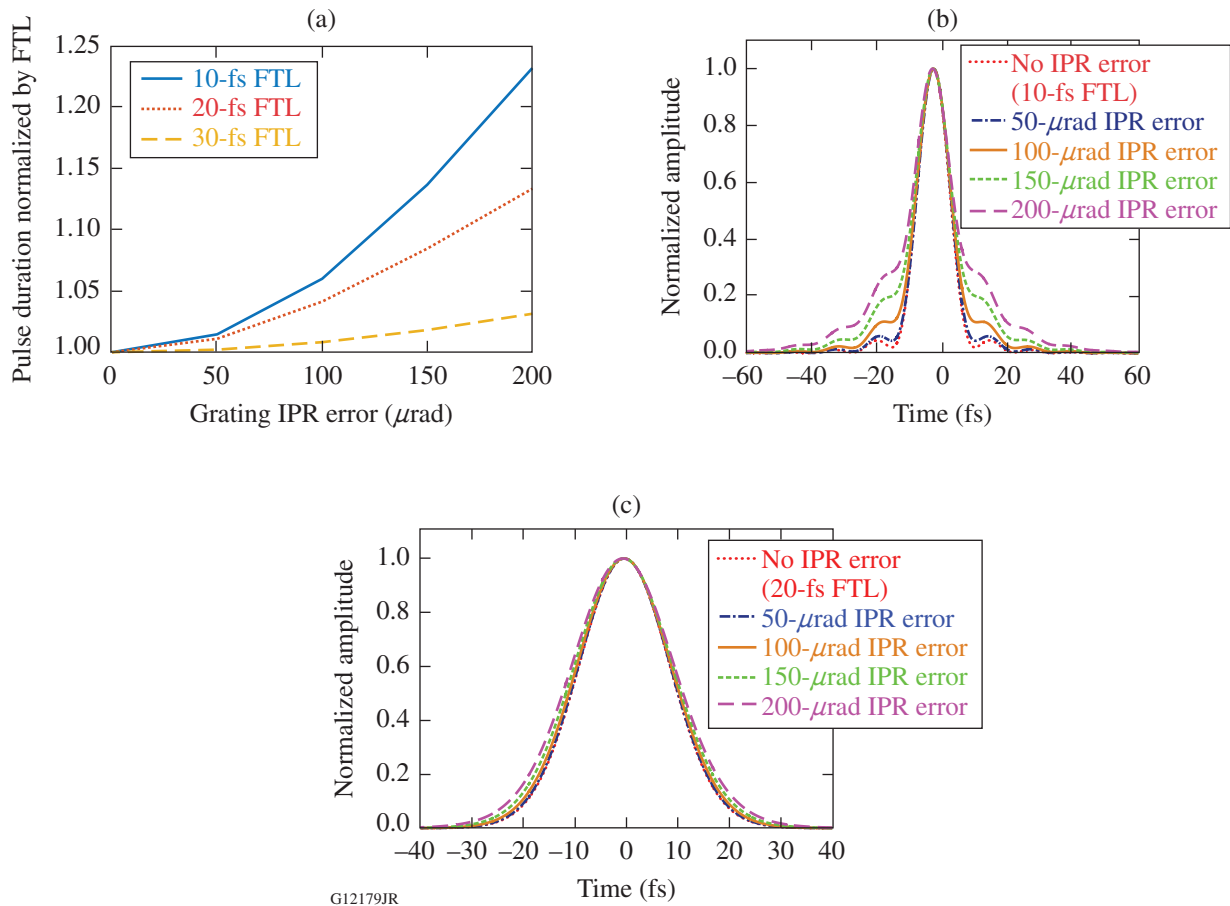


Figure 155.30

(a) Increases in FWHM pulse duration normalized by the FTL are plotted for different magnitudes of IPR error, where angular dispersion has been compensated by a proportional tip adjustment, following Eq. (9). Deformation of pulse shapes are shown for (b) a 10-fs FTL pulse (20th-order super-Gaussian spectrum) and (c) a 20-fs FTL pulse (Gaussian spectrum) for various tip-compensated IPR errors.

reversed and canceled to first order on the second pass. Simulations of tip and IPR error showed that there was no effect on the pulse duration or spot size for errors  $<1000 \mu\text{rad}$ , but pulse distortions grew to  $\sim 10\%$  for grating errors of  $2000 \mu\text{rad}$  for a 10-fs FTL bandwidth.

## Conclusions

In conclusion, the effects of grating-compressor misalignment have been reviewed and simulated in a *FRED-MATLAB* compressor model, showing the alignment sensitivity of tilt, tip, and IPR for a 0.5-PW, 15-fs OPCPA system. These simulations were expanded to estimate grating-tilt-alignment tolerances in a framework of bandwidths ranging from 1000-fs FTL to 10-fs FTL and compressor beam sizes ranging from 10 mm to 300 mm. These tolerances provide guidelines for how compressor alignment sensitivity scales with bandwidth and compressor beam size for mainstream CPA technologies and

performance levels. For compressor beam sizes above 100 mm and transform-limited pulse durations below 30 fs, alignment tolerances decrease significantly, and individualized simulation is recommended for more-accurate specification of grating mount precision and stability requirements or for application-specific tolerance definition.

Supplementary scaling of grating-alignment tolerances with all possible combinations of groove density and incident angle was simulated for a 30-fs FTL bandwidth and 100-mm beam size. Compressor geometries where the incident angle was smaller than the diffracted angle were most sensitive to misalignment, as well as compressors at any incident angle with grating groove density  $>1500 \text{ gr/mm}$ .

Sources of compressor alignment error and methods for alignment were discussed. Compensating the residual chirp

that results from grating-tilt error by adjusting the grating separation was shown to partially decrease pulse distortions in simulations. Arbitrary shaping of the spectral phase by using an AOPDF was shown to further decrease the pulse distortion caused by grating-tilt error.

Simulations showing the compensation of IPR error with tip adjustment (and vice versa) were performed for varying bandwidths and beam sizes. Temporal contrast degradation and serious pulse distortion were observed for FTL pulse durations below 20 fs and compensated IPR/tip errors larger than  $\sim 200 \mu\text{rad}$ , with no obvious effect on the focused spot size. A practical optimization method for IPR and tip alignment was discussed.

Alignment can be significantly simplified in a folded compressor comprised of a single grating pair and a vertical roof mirror since vertical components of angular dispersion are canceled to first order. Tip and IPR errors up to  $1000 \mu\text{rad}$  were simulated with no effect on the pulse duration or focused spot size. As a consequence of double passing each grating, the tilt-alignment sensitivity is increased by a factor of 2.

To our knowledge this is the first time compressor alignment tolerances have been simulated over a broad range of bandwidths, compressor beam sizes, incident angles, and grating groove densities and applied generally to all mainstream CPA technologies to illustrate tolerance scaling. Furthermore, several compressor misalignment compensation strategies were studied in *FRED-MATLAB* to identify bandwidth, temporal contrast, and error-magnitude limitations.

#### ACKNOWLEDGMENT

This material is based upon work supported by the Department of Energy National Nuclear Security Administration under Award Number DE-NA0001944, the University of Rochester, and the New York State Energy Research and Development Authority. The support of DOE does not constitute an endorsement by DOE of the views expressed in this article.

#### REFERENCES

1. D. Strickland and G. Mourou, *Opt. Commun.* **55**, 447 (1985).
2. A. Klenke *et al.*, *Opt. Lett.* **38**, 2283 (2013).
3. Z. Gan *et al.*, *Opt. Express* **25**, 5169 (2017).
4. K. Osvay and I. N. Ross, *Opt. Commun.* **105**, 271 (1994).
5. Z. Wang, Z. Xu, and Z.-Q. Zhang, *IEEE J. Quantum Electron.* **37**, 1 (2001).
6. G. Pretzler, A. Kasper, and K. J. Witte, *Appl. Phys. B* **70**, 1 (2000).
7. K. Osvay *et al.*, *IEEE J. Sel. Top. Quantum Electron.* **10**, 213 (2004).
8. C. Fiorini *et al.*, *IEEE J. Quantum Electron.* **30**, 1662 (1994).
9. O. E. Martinez, *J. Opt. Soc. Am. B* **3**, 929 (1986).
10. J.-C. Chanteloup *et al.*, *J. Opt. Soc. Am. B* **17**, 151 (2000).
11. *FRED*, Photon Engineering LLC, Tucson, AZ 85711.
12. M. Guardalben and G. Dahl, *EPCOMP*, a beam-propagation code developed at the Laboratory for Laser Energetics, University of Rochester, Rochester, NY (2004) (unpublished).
13. J. Bromage, presented at The 3rd International Symposium on High Power Laser Science and Engineering, Suzhou, China, 9–13 April 2018.
14. J. Qiao, A. Kalb, M. J. Guardalben, G. King, D. Canning, and J. H. Kelly, *Opt. Express* **15**, 9562 (2007).
15. The MathWorks Inc., Natick, MA 01760-2098.
16. P. Poole *et al.*, *Opt. Express* **21**, 26,341 (2013).
17. F. Canova *et al.*, *Opt. Express* **15**, 15324 (2007).
18. J. L. Collier *et al.*, *Central Laser Facility Annual Report 2002/2003*, 168, Rutherford Appleton Laboratory, Chilton, Didcot, Oxon, England, RAL Report No. RAP-TR-2003-018 (2003).
19. M. J. Guardalben, *Appl. Opt.* **47**, 4959 (2008).
20. F. Verluise *et al.*, *Opt. Lett.* **25**, 575 (2000).

# A Rate-Doubled 10-GHz Fiducial Comb Generator for Precision Optical Timing Calibration

## Introduction

High-energy-density plasma experiments conducted at LLE<sup>1</sup> utilize a ROSS (Rochester Optical Streak System)<sup>2</sup> streak camera as a primary recording device to time resolve subnanosecond events. These measurements include P510 streak-camera OMEGA beam diagnostics,<sup>3</sup> the velocity interferometer system for any reflector (VISAR)<sup>4</sup> to measure shock-front propagation, the neutron temporal diagnostic (NTD)<sup>5</sup> to measure the fusion-reaction-rate history of neutrons for inertial confinement fusion (ICF)<sup>6</sup> experiments, and the Thompson scattering system (TSS)<sup>7</sup> to analyze scattered light ( $\lambda = 190 \text{ nm}$  to  $850 \text{ nm}$ ) generated during target shots. Time-base calibration for the streak cameras at the  $\sim 1\%$  level is desired for these experiments. The analog electrical waveforms applied to the streak-tube deflection plates are inherently nonlinear. Variations in the sweep rate across the output phosphor screen are of the order of 10% to 15%. Experiments with measurement duration times of less than a few nanoseconds require faster fiducial comb rates than are currently available for accurate time-base calibration. This calibration standard need motivated the development of the 5-GHz comb generator and corresponding optical rate doubler presented here.

## Comb Generator Design

A 5-GHz externally optical rate-doubled fiducial comb generator was developed with four selectable comb pulse rates and a corresponding optical rate doubler to produce a 10-GHz pulse rate. This is a self-contained and portable generator that is useful for many types of optical timing calibration needs. The comb generator is shown in Fig. 155.31. The output is fiber optic coupled at a wavelength of 680 nm (visible red) with a nearly Gaussian pulse shape. The peak pulse output power is  $\sim 5 \text{ mW}$ . A low-phase-noise microwave drive source provides low pulse-to-pulse jitter. The output rate can be synchronized to an externally supplied reference standard frequency source. An internal reference frequency crystal oscillator is incorporated for stand-alone operation.

The light pulses from the comb generator are produced by a solid-state vertical-cavity, surface-emitting laser (VCSEL).



G12262JR

Figure 155.31

The 5-GHz comb generator is a portable self-contained calibration instrument.

These solid-state lasers are primarily used for high-bandwidth fiber-optic communications transmitting sources. VCSEL's have the advantages of being solid state, small, cost effective, and straightforward to couple to fiber-optic media. The increasing need for higher data rates has prompted the development and availability of VCSEL's that support higher modulation bandwidths. These higher-bandwidth VCSEL's can be directly applied in the development of fiducial comb generators when driven by a sine-wave microwave signal in place of a communication data stream. The VCSEL used for this design is rated for 10-GB/s data rates, or 5-GHz modulation. The output is centered at a wavelength of 680 nm (visible red).<sup>8</sup> The peak pulse output power is  $\sim 5 \text{ mW}$ . The VCSEL output is coupled with a fiber-optic launcher to a  $100\text{-}\mu\text{m}$ -diam fiber. For streak-camera sweep calibration, the fiber output is imaged onto the photocathode.

In the communications integrated circuit (IC) industry, a variety of manufacturers provide high-bandwidth VCSEL drivers to modulate the light produced by a VCSEL in accordance to a digital data stream applied to the input of the driver. It was our experience, however, that commercially available IC drivers were better suited to continuous data streams than a burst of a microwave sinusoid needed for the fiducial comb

picket application. A burst of fiducial picket pulses, instead of a steady stream of pulses, is utilized to prevent excessive illumination and blooming of the streak-camera photocathode onto the imager, thereby obscuring desired diagnostic data or potentially damaging the streak camera. The comb fiducial burst is driven to be on only when the camera sweeps.

The block diagram of a fiducial comb generator is shown in Fig. 155.32. The main components of the fiducial comb generator are (1) the low-phase-noise, phase-locked loop (PLL) 5-GHz microwave modulation source; (2) the rate-selection frequency divider and filter network; (3) the microwave VCSEL driver amplifier; (4) the VCSEL bias driver/duty cycle switch; and (5) the fiber-coupled VCSEL. Additional functional blocks represent operational control, primary dc power, VCSEL temperature stabilization, output-pulse triggering, and an internal PLL reference frequency source.

The 5-GHz PLL microwave modulation source is a phase-locked dielectric resonator oscillator (PDRO).<sup>9</sup> This is a low-noise oscillator with phase-locked loop frequency control that locks the output frequency to an integer multiple of the

reference frequency input. The reference frequency used is 75.997870 MHz, twice the 37.998935-MHz reference frequency for LLE’s OMEGA and OMEGA EP Hardware Timing Systems. This reference frequency can be either externally sourced or internally sourced from a temperature-stabilized crystal oscillator. The phase-locked loop multiplier is  $N = 66$  to produce a PDRO output frequency of 5.0159 GHz. Table 155.III lists the manufacturer’s specified phase-noise characteristics of the PDRO when locked to a low-noise reference frequency source. Utilizing Eq. (1) from Ref. 10, phase-noise sideband energy can be converted to equivalent rms jitter assuming no amplitude modulation (AM) contribution to the sideband energy exists:

$$\sigma_{\text{jitter}} [\text{s}] = \frac{\sqrt{2 \cdot \int_0^{\infty} S(f) df}}{2\pi f_0} \quad (1)$$

In Eq. (1),  $S(f)$  is the phase-noise sideband power in W/Hz as a function of frequency separation from the center frequency,  $f_0$ .  $S(f)$  is integrated over the total single sideband frequency

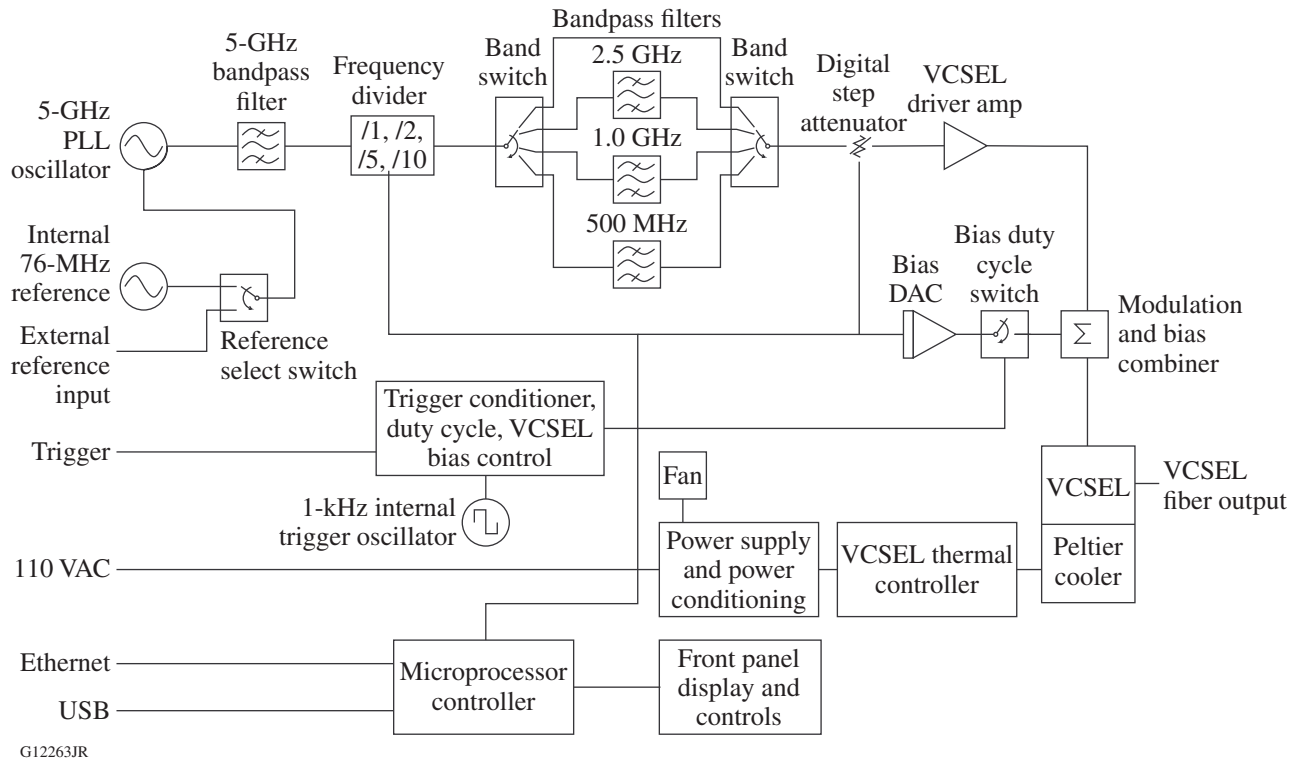


Figure 155.32 The main functional components of the comb generator are illustrated in this block diagram. DAC: digital-to-analog converter; PLL: phase-locked loop; VAC: volts ac; VCSEL: vertical-cavity, surface-emitting laser.

range. The square root of twice this value (to include both sidebands) is equal to the rms phase jitter in radians for small values of phase deviation. This result is converted to rms jitter in seconds by dividing by the radian center frequency of the signal source. Utilizing the values specified for phase noise for the phase-locked 5.0159-GHz oscillator from Table 155.III, the output jitter using a low-noise 76-MHz reference is  $\sim 0.1$ -ps rms. Future measurements on production comb generators will be performed to verify this result.

Table 155.III: Phase-noise specification of the phase-locked 5-GHz dielectric resonator oscillator (PDRO) with a low-noise, 76-MHz crystal oscillator reference source.

Distance from Center Frequency	Phase Noise (dBm/Hz)
100 Hz	-68
1 kHz	-98
10 kHz	-113
20 kHz	-113
100 kHz <sup>a</sup>	-113

<sup>a</sup>Above 100 kHz the contribution to the phase-noise power integral is insignificant.

### 1. VCSEL Source and Rate Divider

The phase-locked oscillator output passes through a selectable rate divider and corresponding filter network to provide four comb rates with lower rates to accommodate applications that require longer pulse spacing. The divider can be set to four values: 1 (5.0159 GHz), 2 (2.5079 GHz), 5 (1.0032 GHz), and 10 (501.59 MHz). These modulation frequencies produce comb light pulse spacings of 199.4 ps, 398.7 ps, 996.8 ps, and 1.994 ns, respectively. The filter network following the divider has selectable bandpass filters that are centered at the selected divider output rate to remove harmonics, subharmonics, and spurious products at the desired frequency. The filtered signal passes through a broadband VCSEL driver amplification stage. The driver amplifier produces a level sufficient to modulate the amplitude of the VCSEL from the “off” to the “on” state when a dc bias is applied that is just below the VCSEL on-state threshold current. A programmable attenuator is included preceding the VCSEL driver amplifier, which allows one to adjust the modulation level to the VCSEL. Modulating the VCSEL with a sine-wave drive produces a nearly Gaussian output light pulse shape.

### 2. VCSEL Bias

The VCSEL bias is a rectangular pulsed bias source that is combined with the microwave driver modulation signal through a microwave resistive combiner. The bias signal has two pur-

poses: (1) to bias the VCSEL just below the on-state threshold current to reduce modulation latency; and (2) to set a fixed pulse burst duration to limit the laser on time, preventing intensity edge blooming on the streak camera prior to and following the streak sweep. The modulation and bias pulses are set so that neither one alone will illuminate the VCSEL independently, but only when combined together will the VCSEL produce a modulated light output. Both the duration and amplitude of the bias pulse are adjustable. The bias pulse is initiated by selecting operation from an external trigger or internally by a continuous 1-kHz repetition-rate trigger.

To improve VCSEL output efficiency, a thermoelectric Peltier cooler is mechanically connected to the VCSEL, which stabilizes its temperature to 20°C. The 680-nm modulated output of the VCSEL is coupled into a 100- $\mu$ m-diam fiber. The fiber output is available at an SC connector on the front panel of the comb generator.

### 3. Control

Control of the comb generator is accomplished via the front panel (Fig. 155.31) or through a serial communications interface (Ethernet or USB). The front panel controls provide access to the settings required to monitor and optimize comb performance for each rate. Each output rate can have unique settings for modulation level, bias level, and burst duration. These are stored and automatically retrieved upon power up.

Remote control can be accomplished in two ways: An internal web page with setting-entry boxes and operation monitor displays is available through a unique URL address for the generator. The control page of the web interface is illustrated in Fig. 155.33. All operational controls can be accessed through this page including operation fault threshold settings. The comb generator can also be controlled by ASCII text string commands through the Ethernet or USB ports.

### 4. Output Rate-Doubling Option

An external optical pulse doubler can be added to the VCSEL output from the front panel to reduce the comb pulse spacing to 99.7 ps (Ref. 11). The optical ray trace in Fig. 155.34 illustrates the principle of operation. The  $f/2.5$  randomly polarized output of the fiber is collimated using a molded aspheric lens. A polarizing cube splits the collimated beam into equal-energy  $p$ - and  $s$ -polarization paths. Separation based on polarization provides high throughput when the beam paths recombine at the output cube splitter, which would not be the case with dichroic beam splitters. The  $p$ -polarization path is transmitted through the input and output polarizing cubes and

**Laboratory for Laser Energetics**

APP NAME: E-GS-F-039\_Mark-1.4, IP: 172.20.42.235, S/N: 0

[Refresh Page](#) | [Alarm Thresholds](#) | [Netburner Setup](#) | [Help](#)

Property	Setting	Update	Comment
VCSEL State	<input type="checkbox"/> OFF	Toggle	ON, OFF
VCSEL Frequency	1.0	Submit	0.5, 1.0, 2.5, 5.0
Modulation level	25	Submit	000 to 100, Stepsize = 1
Duration	100	Submit	20 to 510ns, Stepsize = 2ns
Bias Level	70	Submit	000 to 100, Stepsize = 1
Trigger	EXT	Submit	INT = Internal, EXT = External
Reference	INT	Submit	INT = Internal, EXT = External

Readings	
PCB Temp	21.6°C
VCSEL Temp	20.4°C
PDRO State	LOCKED

VCSEL Faults Monitor				
PWR SUP	REF LVL	TEMP	CONTROL	PDRO STATE
●	●	●	●	●

FAULT RESET

Runtime: 0d:00h:02m:04s

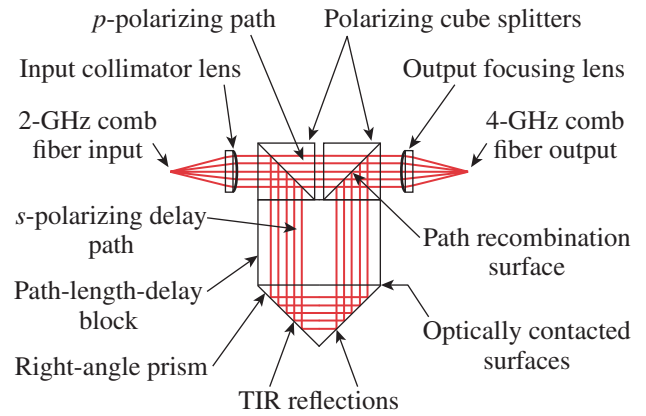
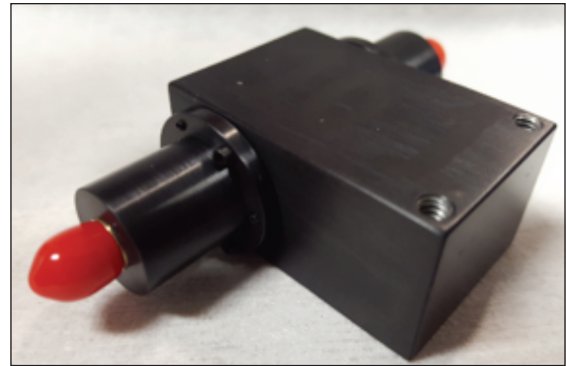
©2017 University of Rochester Laboratory for Laser Energetics, All Rights Reserved.

G12264JR

Figure 155.33

The comb generator web interface page allows one to remotely access all controls.

is focused into the output fiber via a matching aspheric lens; all surfaces are antireflection (AR) coated. The aspheric lens pair forms a diffraction-limited unity magnification  $f/2.5$  relay from the input fiber to the output fiber. The input cube reflects the  $s$ -polarization path at  $90^\circ$ . The exiting surface of the cube is bonded to the path-length-delay block using index-matching epoxy. The path-length-delay block is optically contacted to the hypotenuse of a right-angle prism used to transport the beam back through the glass delay block using total internal reflection (TIR) at the prism to air uncoated surface interfaces. The path-length-delay block is sized appropriately to retard the beam propagation time by half the 5-GHz rate  $\pm 0.5$  ps relative to the straight-through  $p$ -polarization path. The two beam paths are recombined at the output polarizing cube and focused into the output fiber. The use of AR coatings, optically contacted surfaces, and TIR minimizes throughput losses. The aspheric lenses, the polarization cube splitters, and the right-angle prism are off-the-shelf components. The path-length-delay block was custom fabricated to the required length and aperture. The resulting doubler output rate is 10.0318 GHz.



G12265JR

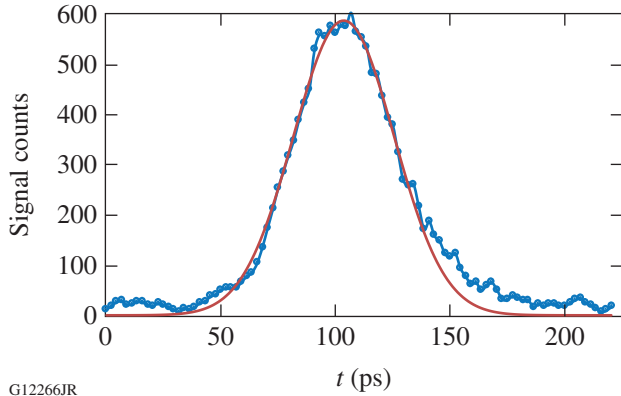
Figure 155.34

The 5-GHz input comb is split into  $p$ - and  $s$ -polarization paths. The  $s$ -polarization path is time delayed and recombined with the  $p$ -polarization path. The interleaved 10-GHz comb is focused into the output fiber. TIR: total internal reflection.

**Performance Results**

Tests of the 5-GHz comb generator on the ROSS streak camera have been performed. The light output pulse from the comb generator is nearly Gaussian with a full width at half maximum (FWHM) of  $\sim 48$  ps as illustrated in the lineout from the ROSS streak camera in Fig. 155.35. Figure 155.36 shows the streak-camera imager output with a 5.0159-GHz comb rate compared to a 1.976-GHz comb rate from a Sydor Technologies 2-GHz comb generator streaked simultaneously. Figure 155.37 shows the lineout of pixel counts versus time of the 5-GHz streak from Fig. 155.36. The output power of the 5.0159-GHz pulses was measured with an Ophir-Spiricon PD300 photodiode integrating power sensor over a 50-ns comb pulse burst. The total integrated energy over the burst was 65 pJ for 251 pulses, giving an average energy per pulse of 0.259 pJ. For a Gaussian-shaped energy profile with a FWHM of  $\sim 48$  ps, the peak power of an individual comb pulse is  $\sim 5.1$  mW.

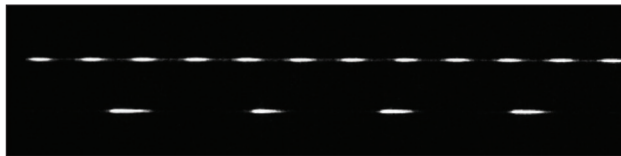
Figures 155.38–155.40 illustrate the measured ROSS streak-camera performance for the other three selectable comb generator rates: 2.5079 GHz, 1.0032 GHz, and 501.59 MHz. Figure 155.41 illustrates a measurement of the externally optical rate doubled output at 10.0318 GHz.



G12266JR

Figure 155.35

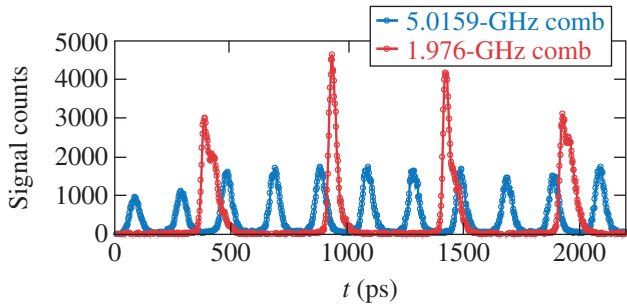
The 5.0159-GHz comb generator light pulse shape is nearly Gaussian. The horizontal axis is time, and the vertical axis is the relative pixel count from the imager. The red curve represents the measured lineout data, and the solid blue curve is a best-fit Gaussian profile.



G12267JR

Figure 155.36

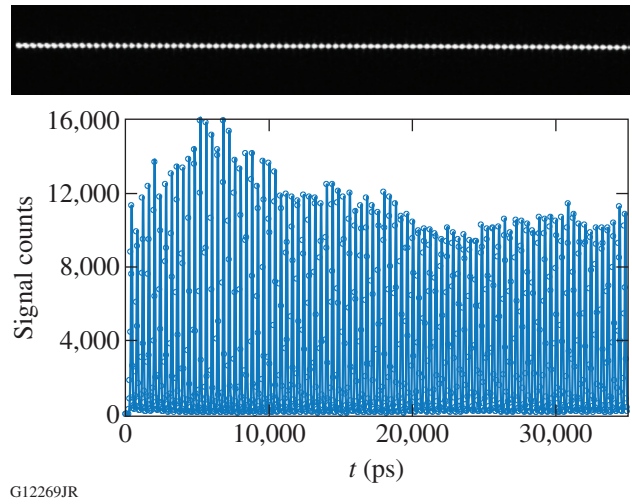
Imager display of the 5.0159-GHz comb (top trace) compared to the Sydor Technologies 1.976-GHz comb (bottom trace) on a 2.2-ns ROSS sweep.



G12268JR

Figure 155.37

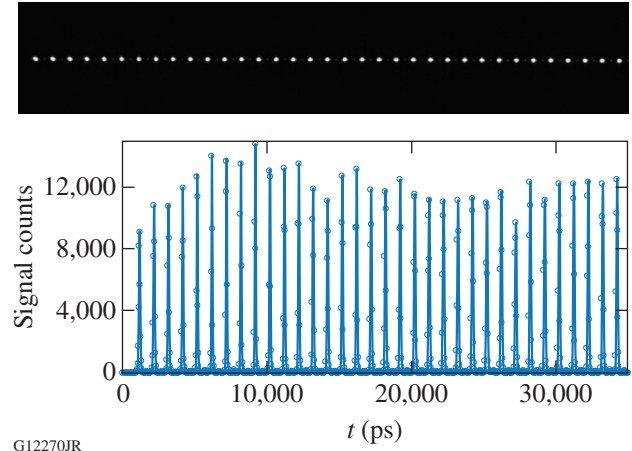
Pixel counts versus time for the 5.0159-GHz streak in Fig. 155.36.



G12269JR

Figure 155.38

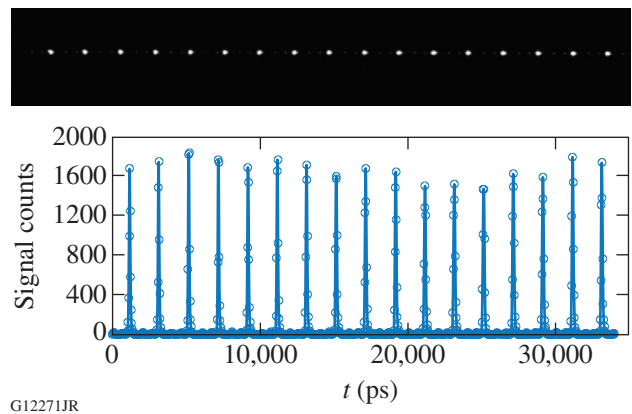
The 2.5079-GHz output on a 35-ns streak-camera sweep with lineout.



G12270JR

Figure 155.39

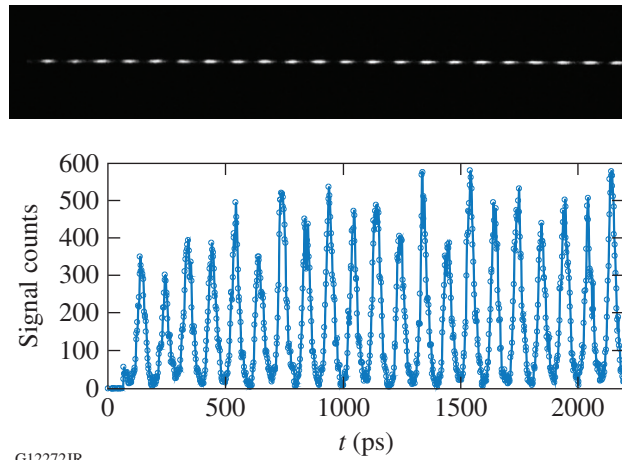
The 1.0032-GHz output on a 35-ns streak-camera sweep with lineout.



G12271JR

Figure 155.40

The 501.59-MHz output on a 35-ns streak-camera sweep with lineout.



G12272JR

Figure 155.41  
The 10.0318-GHz externally optical rate-doubled output.

### Conclusion

An optically rate-doubled 5-GHz fiducial comb generator was developed with a selectable maximum 10-GHz comb repetition rate utilizing an external fiber-optic doubler. This is a self-contained and portable generator that is useful for many optical timing calibration needs. Its primary use is for ultrafast streak-camera temporal calibration. The output is fiber optic coupled at a wavelength of 680 nm (visible red) with a nearly Gaussian pulse shape. The peak output power per comb pulse is  $\sim 5$  mW. The low phase noise of the internal microwave drive source provides low pulse-to-pulse jitter of less than 0.1-ps rms. An external reference frequency standard can be utilized to synchronize the output to external timing equipment. An internal reference frequency generator exists for stand-alone operation.

In the future as higher modulation bandwidth VCSEL's are developed and become commercially available, comb generators with higher rate comb outputs will be produced for enhanced timing needs. Microwave sources and drivers exist currently to support operation into the tens of GHz. It is also possible to consider incorporating the comb generator presented within a streak-camera calibration module internal to the camera itself. The remote control features of the comb generator can open up a means for developing software to perform streak-camera auto-calibration. Although the appli-

cation presented focused on streak-camera calibration, these frequency-stable, low-jitter optical comb generators can also be used as timing calibrators for other diagnostic and triggering needs where fiber-optic periodic light pickets are utilized as timing fiducials.

### ACKNOWLEDGMENT

This material is based upon work supported by the Department of Energy National Nuclear Security Administration under Award Number DE-NA0001944, the University of Rochester, and the New York State Energy Research and Development Authority. The support of DOE does not constitute an endorsement by DOE of the views expressed here.

### REFERENCES

1. J. M. Soures, R. L. McCrory, C. P. Verdon, A. Babushkin, R. E. Bahr, T. R. Boehly, R. Boni, D. K. Bradley, D. L. Brown, R. S. Craxton, J. A. Deletrez, W. R. Donaldson, R. Epstein, P. A. Jaanimagi, S. D. Jacobs, K. Kearney, R. L. Keck, J. H. Kelly, T. J. Kessler, R. L. Kremens, J. P. Knauer, S. A. Kumpan, S. A. Letzring, D. J. Lonobile, S. J. Loucks, L. D. Lund, F. J. Marshall, P. W. McKenty, D. D. Meyerhofer, S. F. B. Morse, A. Okishev, S. Papernov, G. Pien, W. Seka, R. Short, M. J. Shoup III, M. Skeldon, S. Skupsky, A. W. Schmid, D. J. Smith, S. Swales, M. Wittman, and B. Yaakobi, *Phys. Plasmas* **3**, 2108 (1996).
2. Sydor Technologies, Fairport, NY 14450.
3. W. R. Donaldson, R. Boni, R. L. Keck, and P. A. Jaanimagi, *Rev. Sci. Instrum.* **73**, 2606 (2002)
4. P. M. Celliers, D. K. Bradley, G. W. Collins, D. G. Hicks, T. R. Boehly, and W. J. Armstrong, *Rev. Sci. Instrum.* **75**, 4916 (2004).
5. *LLE Review Quarterly Report* **145**, 36, Laboratory for Laser Energetics, University of Rochester, Rochester (2015).
6. R. Betti and O. A. Hurricane, *Nat. Phys.* **12**, 435 (2016).
7. D. H. Froula, J. S. Ross, L. Divol, and S. H. Glenzer, *Rev. Sci. Instrum.* **77**, 10E522 (2006).
8. Communications Grade VCSEL (680 nm), part number code: 680C-0000-x002 (data sheet), Vixar, Plymouth, MN 55441, available online at <http://vixarinc.com>.
9. PLO-2000: Ext Ref Phase Locked Oscillator, Microwave Dynamics, Irvine, CA, 92618.
10. MT-008 Rev A. Analog Devices Inc., Norwood, MA 02062.
11. R. Boni, J. Kendrick, and C. Sorce, *Proc. SPIE* **10390**, 1039003 (2017).

---

# Investigation of Laser-Induced Damage in Hafnia/Silica Multilayer Dielectric Coatings Under 1053-nm, 600-fs to 100-ps Laser Irradiation

## Introduction

The limiting factor governing the output power in current-generation, large-aperture laser systems<sup>1,2</sup> is typically related to the resistance of its optical components to laser-induced damage.<sup>3,4</sup> The energy coupling is facilitated by the presence of defects related to fabrication-specific processes and operational environment-related parameters. The mechanisms of damage initiation with nanosecond pulses and associated material modification have been extensively studied in recent years. However, the processes involved in laser damage for pulse durations between about 0.5 and 100 ps remain poorly understood. Our research efforts have been focused on this intermediate temporal regime and are motivated by the need to improve the damage-performance characteristics and reduce the cost of operations of the OMEGA EP Laser System, operating at 1053-nm wavelength and with an adjustable pulse duration between 0.7 and 100 ps.

The morphology of the damage sites is governed by (a) the location of energy deposition; (b) the laser parameters (such as pulse length, spatial characteristics of the beam, and wavelength); and (c) the material thermodynamic properties that determine the material relaxation following laser-energy coupling and deposition. Consequently, the morphology of the damage sites provides signatures of the thermodynamic pathway of laser damage that can aid in understanding the origin and evolution of damage. This information, in turn, can be used for designing and fabricating next-generation optical components with higher damage thresholds.

Multilayer dielectric (MLD) coatings are widely used in large-aperture, short-pulse laser systems. MLD coatings typically involve alternating high- and low-refractive-index layers, where laser-induced damage can initiate in different layers within the MLD stack. The focus of the present work is to provide a more-detailed description of the damage morphology in MLD-coated high reflectors and to identify the underlying damage-initiation mechanism. Specifically, we investigate low-loss MLD SiO<sub>2</sub>/HfO<sub>2</sub> mirrors that were fabricated at LLE in order to have a precise knowledge of the design and, conse-

quently, the associated standing-wave electric-field intensities within the layer structure. Detailed imaging of the damage sites, typically obtained with scanning electron microscopy (SEM) and atomic force microscopy (AFM), is used to characterize their morphologies and directly correlate to the location of energy deposition and the corresponding electric-field distribution. The depth measurements are used as a diagnostic to identify the location of the initial energy deposition within the MLD stack. The results suggest that there are three distinct damage-initiation morphologies: the first prevailing at laser pulse lengths shorter than about 2.3 ps, while the other two are observed for longer pulses. Modeling of the processes involved for each type of damage morphology helps reveal the underlying mechanism of laser-induced damage.

## Experimental Details

The laser system used in this study operates at 1053 nm with an adjustable pulse duration between 600 fs and 100 ps. The laser beam is focused on the sample using a 200-cm-focal-length mirror providing a nearly circular, ~350- $\mu$ m-diam beam spot. Each tested site on the sample is exposed to a single pulse at a predetermined fluence in a vacuum chamber at a pressure of  $\sim 10^{-6}$  Torr. Various samples representing typical SiO<sub>2</sub>/HfO<sub>2</sub> MLD mirror designs fabricated via electron-beam deposition were used in this study. The distribution of electric-field intensity within the MLD stack was calculated using commercially available software (OptiLayer).

## Experimental Results

The results suggest that there are three general morphologies of damage sites observed with characteristic examples as shown in Figs. 155.42–155.44. These damage morphologies (denoted as type I, type II, and type III) are observed at different laser pulse durations, with type I observed for pulses between 0.6 ps (lower limit of our laser pulse tunability) and 2.3 ps, and types II and III observed for pulses between 2.3 ps and 100 ps (upper limit of our laser pulse tunability). The images in Fig. 155.42 demonstrate the key characteristics of type-I damage sites. Their morphology involves large shallow craters having a diameter of the order of 30  $\mu$ m, which corresponds to the diameter of the laser impinging

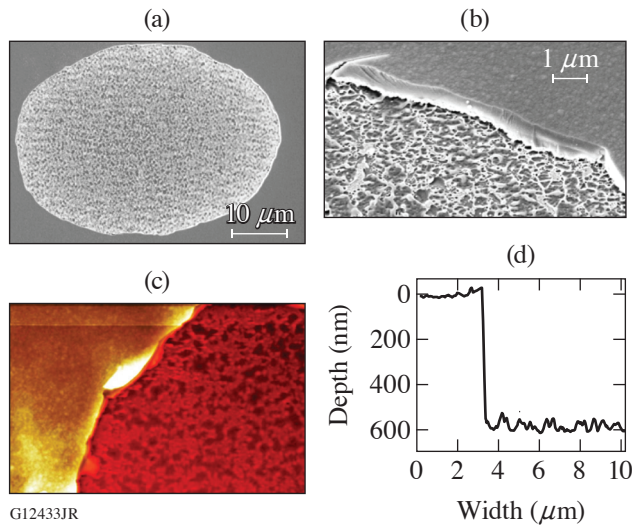


Figure 155.42 [(a),(b)] Scanning electron microscopy (SEM) and (c) atomic force microscopy (AFM) images of type-I damage sites. (d) AFM image cross section data make it possible to evaluate the crater depth and roughness.

on the sample having intensity above the damage threshold. The general morphology of a type-I damage site is best captured by the lower-resolution SEM image shown in Fig. 155.42(a). Typical characteristics include well-defined edges and a quasi-circular profile (affected by the beam shape and beam-incidence angle) that is centered at the location of peak intensity within the laser beam. The sidewalls are nearly vertical, while the bottom of the crater is rough, possibly associated with melted material remnants formed during the damage process. These features are captured in the higher-resolution SEM image shown in Fig. 155.43(b) and the AFM image shown in Fig. 155.43(c). The associated cross sections of AFM images [example shown in Fig. 155.43(d)] allow the depth of the crater to be measured, which is expected to be directly related to the depth of energy deposition (damage initiation and plasma formation). The roughness at the bottom of the crater can also be quantified and is found to typically be of the order of 50 nm (peak to valley). Depending on the coating design as well as the angle and polarization of incident light, the bottom of the crater is located either within the top  $\text{SiO}_2$  layer or at the interface between the first  $\text{HfO}_2$  and the second  $\text{SiO}_2$  layer. Comparison with the calculated electric-field distribution within the stack reveals that these positions correspond to a depth of the first or second electric-field-intensity (EFI) peak, respectively. The observed depths correlate very precisely (within less than 10 nm) to the location of damage initiation as predicted by the electric-field-limited model.<sup>5</sup>

Figure 155.43 captures the typical morphology of the second type of damage site (type II) observed under excitation with

pulses longer than  $\sim 2.5$  ps. Type-II damage sites are isolated, indicating that they originate from nanoscale defects. The diameter of these sites is of the order of a few hundred nanometers to a few micrometers, largely dependent on the laser pulse duration. The images of damage sites shown in Fig. 155.43 were generated at different pulse lengths, characterizing the damage in great detail. All SEM images shown in Fig. 155.43 are on the same spatial scale so that one can compare the change in morphology as a function of pulse duration. Specifically, Figs. 155.43(a)–155.43(d) show damage sites formed under irradiation with 4.6-, 10-, 20-, and 100-ps pulses, respectively. In general, the size of type-II damage sites is found to be proportional to the pulse length of the laser illumination.

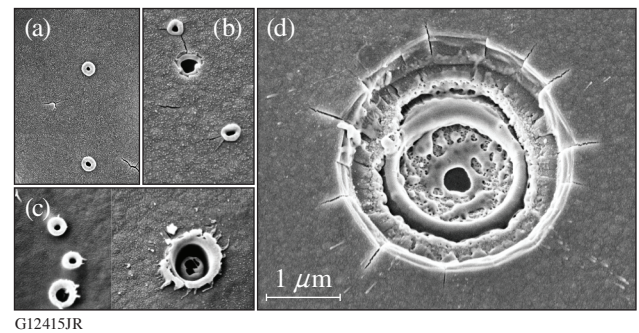


Figure 155.43 SEM images of type-II damage sites formed under exposure to 1064-nm, (a) 4.6-, (b) 10-, (c) 20-, and (d) 100-ps laser pulses.

The complex crater morphology contains a venting hole and one or more inner quasi-spherical shells. This elaborate structure is accompanied by the remnants of melted material, indicating a slow cooling process after the energy is deposited. In addition, the craters are surrounded by radial cracks of the order of  $0.5 \mu\text{m}$  to  $1 \mu\text{m}$  in length, indicating the presence of tensile hoop stresses surrounding the crater region. Frequently, some of the sites can be characterized by a set of concentric radial cracks with no well-defined venting holes [see examples in Fig. 155.43(a)]. AFM images indicate that the damage is initiated at locations of peak electric-field intensity near the first hafnia-silica interface. These features suggest that damage-precursor defects are located deep within the MLD structure, while damage initiates at sites of localized peak electric-field intensity.

Type-III damage morphology sites were also observed for pulse durations longer than  $\sim 2.3$  ps, consisting of isolated shallow craters having a diameter of  $\sim 2$  to  $3 \mu\text{m}$  and a depth smaller than about 150 nm. Figure 155.44(a) shows a Nomar-

ski microscope image of an area exposed to a single 10-ps pulse that generated both type-II and type-III damage sites, which appear as darker and brighter features, respectively. The type-III damage sites extend further from the center of the beam, indicating that their damage threshold is lower. Figures 155.44(b) and 155.44(c) show representative AFM and SEM images. Cross-section data obtained from AFM images reveal that type-III damage sites consist of quasi-conical pits. Higher-magnification SEM images from the middle (bottom) of the pit (see inset) reveal the presence of multiple features having diameters of the order of 10 nm. These features might be the signature of the material modification following plasma formation by damage-initiating defects located at the bottom of the pit having diameters of the order of 50 nm or less. It is important to note that the depth of type-III damage sites is not correlated with the electric-field-intensity peak, in contrast with observations for type-I and type-II damage sites.

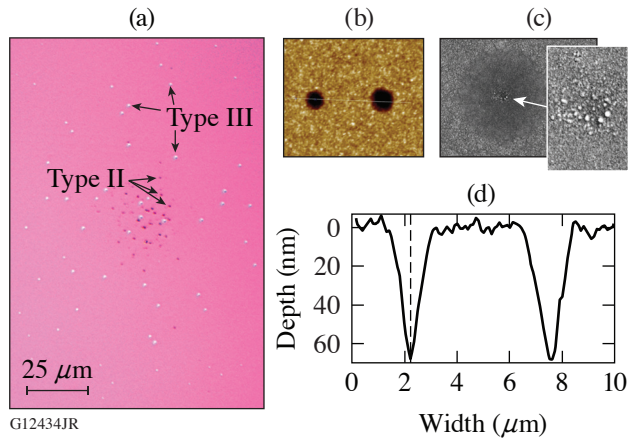


Figure 155.44

(a) Nomarski microscope image of a damage site generated with 10-ps pulses containing both type-II and -III damage sites. (b) AFM and (c) SEM of type-II damage sites. The inset shows the center of the damage site with higher magnification. (d) AFM image cross section data capture the spatial profile of the type-III damage sites.

## Modeling

To better understand the mechanisms associated with the experimentally observed damage morphologies, we explore micro- and nanomechanical models of the material's response to the generation of high pressure and temperature during laser-energy deposition. The observed morphology is initially used as a guide to develop a qualitative depiction of the processes involved, which is subsequently tested and refined using the modeling tools. The thermomechanical and thermodynamic properties of the constituent silica and hafnia layers of the MLD are governing the dynamic material response. Furthermore,

the mechanical properties of the MLD layers are affected by the microstructure of each layer (and therefore the deposition process), as well as the presence of multiple interfaces.<sup>6</sup> In this modeling effort we assume a uniaxial yield stress of 4 GPa based on previous work.<sup>7</sup> For the elastic properties, we assume bulk properties for Young's modulus (72 GPa for silica and 300 GPa for hafnia) and Poisson's ratio (0.17 for silica and 0.25 for hafnia). We also assume bulk values for thermal properties: thermal conductivities of 1 and 2 W/m.K, mass densities of 2200 and 9500 kg/m<sup>3</sup>, and heat capacities of 750 and 270 J/kg.K for silica and hafnia, respectively. Although the reported values for films can be different from bulk material values,<sup>8,9</sup> we consider the above values to be a good approximation to explore the development of sensible models of the mechanisms of damage formation in order to interpret the experimental observations.

The damage sites studied in this work were formed at near-damage-threshold conditions. Consequently, the modeling of the three different types of damage sites discussed next is focused on the threshold conditions for initiating damage. As a result, the damage morphology reflects the dominant mechanism involved in the damage-site-formation process.

### 1. Modeling Mechanism of Type-I Damage Sites

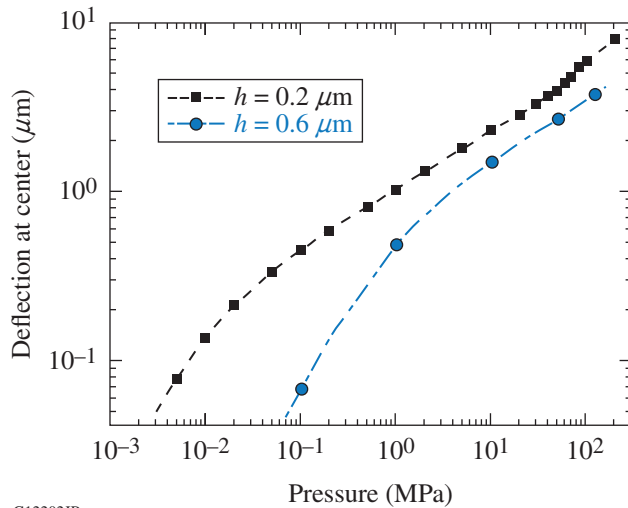
The morphology of a type-I damage site suggests that plasma is initiated within a narrow range of electric-field intensities about the location predicted by the electric-field-limited model. Assuming that this range of electric-field intensity (laterally) is required to support plasma formation (e.g., via multiphoton absorption), we can project the same range of electric-field intensities along the  $z$  axis (inside the coating). This enables one to estimate the thickness of the plasma, which is found to be 60 to 80 nm, depending on the irradiation conditions. The observed removal of the overlying layer implies that the generated pressure is sufficient to support its shear fracture and detachment followed by rapid cooling, resulting in remnants of transient liquid material.

Based on the above qualitative description, the model assumes plasma formation within a thin region at depth  $t_0$  below the surface, followed by evaporation and building of a pressure  $p$  that induces an inflation of the material above. This, in turn, gives rise to the formation of a circular membrane (blister) having radius  $a$ , thickness  $h$  (assumed to be the same as the depth of plasma formation from the surface), and center deflection height  $w_c$ . The center deflection ( $w_c$ ) scales with thickness  $h$  and material properties as<sup>10</sup>

$$(w_c/h) + A(w_c/h)^3 = B(p/e)(a/h)^4, \quad (1)$$

where  $E$  is the Young's modulus of the materials while  $A$  and  $B$  are constants that depend on the Poisson's ratio of the material.

Figure 155.45 shows the center deflection  $w_c$  as a function of initial pressure. Calculations were carried out for an array of relevant initial conditions to determine the center deflection  $w_c$  as a function of the initial pressure generated by the formed plasma. For example, inflation of an axisymmetric membrane at thickness  $h = 200$  nm under pressure  $p = 45$  MPa leads to a center deflection  $w_c = 3.81$   $\mu\text{m}$  accompanied by the formation of a plastic hinge near the support point of the membrane. For small center deflections, i.e.,  $w_c \ll h$ ,  $w_c$  scales linearly with pressure  $w_c \propto p$  since the material behaves in a linear elastic manner and the strains are small. For larger deflections, i.e.,  $w_c \gg h$ , the scaling is nonlinear and  $w_c \propto p^{1/3}$  since the strains (while still elastic) are nonlinear. Furthermore, for small pressures and deflections, the numerical results show that the overall shape of the deflected membrane is well approximated by  $w(r) = w_c(1 - r^2/a^2)^2$ ; i.e., the slope vanishes at the support point. On the other hand, for larger pressures, the shape is essentially spherical and given by  $w(r) = w_c(1 - r^2/a^2)$ .



G12202JR

Figure 155.45  
Model predictions of the center deflection of an inflated membrane for two depths of plasma initiation (membrane thicknesses) of  $h = 0.2$  and  $h = 0.6$  mm with damage site radius  $a = 15$   $\mu\text{m}$ .

The numerical simulations reveal that the stresses at the support point of the inflated membrane always exceed those at the apex; therefore, the failure is expected to initiate at the support point. Although the plastic hinge formation arises at a pressure that scales with the membrane thickness, our numerical simulations indicate that the center deflection is between 3 and 4  $\mu\text{m}$ . On the other hand, the pressure required for the

formation of the hinge scales with the membrane thickness (depth of damage initiation).

## 2. Modeling Mechanism of Type-II Damage Sites

The morphology of type-II damage sites suggests that a significant amount of melting was generated during the damage process. We therefore assume that the precursor defects (located below the surface) absorb a sufficient amount of energy to form plasma, but the pressure generated cannot support the fracture of the layer above, as in type-I damage sites. As a result, the absorbed energy is dissipated via heat diffusion, ultimately leading to softening of the top layer. The presence of radial cracks surrounding the damage site indicates that the generated gaseous material expands, producing swelling on the surface above the location of energy deposition. This, in turn, generates tensile hoop stresses and cracking of the still-cold top layer. Eventually, a venting path is formed where the gaseous and liquid material is released.

This qualitative description is explored using a thermal model of an absorbing defect located near the bottom of the first hafnia layer, where the defect absorbs the incident laser radiation and rapidly heats up followed by thermal diffusion at the end of the pulse.<sup>4,11-15</sup> For simplicity we assume that the defect absorbs laser energy proportionally to its cross-sectional area ( $\pi R_{\text{defect}}^2$ ) and distributes the thermal power over its volume ( $(4/3)\pi R_{\text{defect}}^3$ ), so that the power absorbed per unit volume has a Gaussian temporal dependence:

$$g(t) = g_{\text{max}} \exp\left[-2(t - t_{\text{peak}})/t_{\text{width}}\right]^2, \quad (2)$$

where  $t_{\text{peak}}$  is the time when the pulse is at its peak intensity and  $t_{\text{width}}$  is the pulse width.

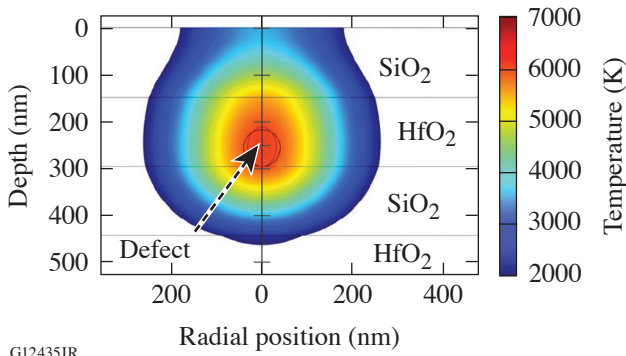
The maximum value ( $g_{\text{max}}$ ) is given by

$$g_{\text{max}} = (3/2\sqrt{\pi})F/(t_{\text{width}}R_{\text{defect}}), \quad (3)$$

where  $F$  is the laser fluence ( $\text{J}/\text{cm}^2$ ). Typical trials for our simulations used pulse widths of 10 to 50 ps and  $R_{\text{defect}} = 20, 40, \text{ and } 60$  nm with adaptation of the bulk properties for  $\text{SiO}_2$  and  $\text{HfO}_2$ .

The modeling results shown in Fig. 155.46 were obtained assuming a laser pulse duration and fluence of 50 ps and 15  $\text{J}/\text{cm}^2$ , respectively, depicting the temperature distribution resulting from absorption by a defect with a 40-nm radius, 18 ns after illumination. This laser fluence represents the experimentally measured damage threshold in this type of

MLD. The isotherms show that the surface temperature reaches well above the melting point of silica with the heating being asymmetric (higher temperature closer to the surface) because of the presence of the material-free surface where heat diffusion is halted. It must be noted that phase transitions and the temperature-dependent thermomechanical parameters were not considered in the models described above; arguably, it may be impossible with current computational capabilities to take into consideration all essential elements involved. The model provides an adequate description, however, of the key mechanism involved in type-II damage-site formation.



G12435JR

Figure 155.46

Model prediction of the temperature distribution 18 ns after illumination, assuming the defect has a radius of 40 nm and is located at the interface between the second and third layers. The fluence of the incident pulse is 15 J/cm<sup>2</sup> and the pulse duration is 50 ps.

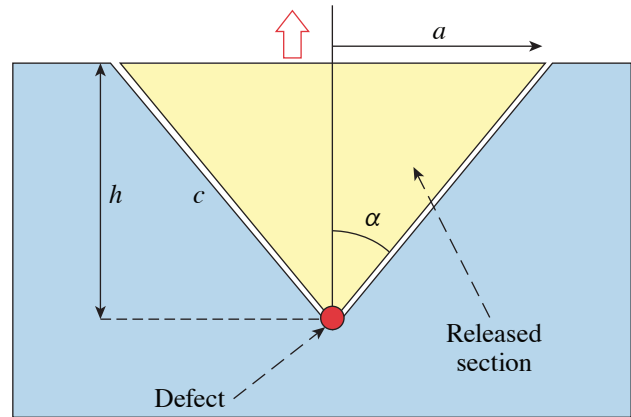
We attribute the complex morphology of the damage sites to the very different thermodynamic properties of SiO<sub>2</sub> and HfO<sub>2</sub> layers. Specifically, since the melting temperature of the hafnia is very close to the evaporation temperature of the silica, mixed-material phases can be simultaneously present such that heat diffusion can facilitate a melted hafnia layer to be accompanied by evaporation of the adjacent silica layer. As the pressure is released via the formed venting pit, subsequent ejection of hot (potentially a mixture of gas and liquid) material results in rapid cooling. We therefore postulate that the inner shell observed in the damage sites is the hafnia layer involved in the damage process with a venting path for release of the evaporated material of the underlying silica layer.

### 3. Modeling Mechanism of Type-III Damage Sites

The morphology of type-III damage sites consists of quasi-conical craters with a high aspect ratio and a central-region morphology suggestive of an explosive boiling process. We therefore assume that this type of morphology may be associated with pressure-driven material ejection. Although this

mechanism is similar to that involved in type-I damage sites, the volume of the plasma region depends on the size of the defects and is much smaller than that for type-I damage sites. As a result, the generated pressure energy is much smaller than that for the type-I damage sites. The generated pressure can still be sufficient, however, to remove material above a defect if it is located close to the surface. The AFM imaging results demonstrate that the depth of type-III damage sites is of the order of 150 nm or less, which is consistent with the hypothesis that absorbing defects located close to the surface can give rise to superheating of a small volume and a very localized high pressure.

Based on the above qualitative interpretation, the relevant geometrical parameters considered in modeling are depicted in Fig. 155.47, where the defect is located at a depth  $h$ ; i.e., a cone of inclined surface area with  $\alpha$  being the cone apex half-angle.



G12416JR

Figure 155.47

Geometrical parameters considered in the modeling of type-III damage sites.

The necessary surface energy is  $G_c A_{\text{cone}}$ , where  $G_c$  is the critical energy-release rate for silica and  $A_{\text{cone}}$  is the area of the cone representing the newly generated surface. These can be described by

$$A_{\text{cone}} = \pi \alpha (h^2 + a^2)^{1/2} = \pi h^2 / \Omega, \quad \Omega = \cos^2 \alpha / \sin \alpha \quad (4)$$

and

$$G_c = K_c^2 / E_Y, \quad (5)$$

where  $K_c$  is the fracture toughness and  $E_Y$  is the Young's modulus for silica. The critical energy release rate  $G_c$  includes the surface energy and the energy consumed by any irreversible

processes in surface creation (such as plasticity, dislocations, etc.). If the energy released by the superheated defect is  $E$ , the resulting crater will reach the surface when

$$E > G_c A_{\text{cone}}, \quad (6)$$

where the energy  $E$  absorbed by the defect is  $E = F_{\text{th}}(\pi^2 R)$ . This leads to a maximum depth  $h_{\text{max}}$  for the defect where the absorbed energy is sufficient to support the formation of a new surface and create the damage site as given by

$$h_{\text{max}} = R(F_{\text{th}}\Omega/G_c)^{1/2}. \quad (7)$$

The AFM images from Fig. 155.44 show that the angle  $\alpha$  is close to  $86.5^\circ$ , leading to  $\Omega = 0.004$ . Using the value  $0.7 \text{ MPa m}^{1/2}$  for the critical stress intensity  $K_c$  in fused silica<sup>16–18</sup> and Young's modulus  $E_Y = 70 \text{ GPa}$ , the critical energy release rate is  $G_c \sim 7 \text{ J/m}^2$ . For order-of-magnitude estimates, we use a laser-damage threshold value of  $\text{LDT} = 7.5 \text{ J/cm}^2$  yielding

$$h_{\text{max}} = 6.4R. \quad (8)$$

The above approach suggests that the observed maximum depth of  $\approx 150 \text{ nm}$  for the type-III damage sites implies that the corresponding maximum radius of the defects is  $\approx 24 \text{ nm}$ . This approach did not take into account, however, the transient processes that can increase the energy absorbed by the defect site such as absorption by the plasma and plasma expansion during the laser pulse, which would increase the effective radius of the absorbing region. In general, this model utilizes simple energy-balance considerations with reasonable energy-coupling factors. In this manner, it is possible to substantiate that type-III damage sites are superficial and originate from mechanical failure of the overlying material resulting from the energy absorbed by defects located at a maximum depth of the order of  $150 \text{ nm}$ . We therefore anticipate that such defects, when located deeper in the MLD structure, may create small voids containing melted and densified material without any observable modification on the surface.

### Discussion

The damage sites investigated in this work represent the typical morphologies at near-damage-threshold irradiation conditions. It was shown that type-I and type-III damage sites are governed by pressure-induced effects, namely the generation of sufficient pressure to remove an overlying layer of material. On the other hand, type-II damage sites result from heat diffusion, thereby creating a larger amount of melted material and a relatively smaller amount of pressure-induced modifications. In

all cases, however, the generated pressure is the driving mechanism for removing material and/or creating a damage crater.

To generate the required pressure, the material must absorb a sufficient amount of energy to reach evaporation conditions (superheating).<sup>19</sup> The pressure energy generated during the initial phase of the relaxation of the material will inevitably facilitate the formation of a blister or microscale bubble within the material. If this initial pressure-induced modification of the material is not sufficient to cause mechanical failure of the material and subsequent release of the vapor/liquid material (which can be in a superheated state), with a corresponding rapid release of energy, heat generation and diffusion will facilitate the gradual transport of the energy away from the absorbing site. The increase of the temperature of the surrounding material leads to modification of its mechanical properties, which can change the fundamental response of the material. For example, heating can introduce melting of the overlying layer and the formation of a blister that may not erupt. Such formation of unerupted blisters is observed in samples where the damage initiates deeper in the stack or at well above damage-threshold irradiation.

Damage can also be initiated at close proximity so that there is overlap between the affected volumes. For example, we have observed type-II damage sites formed within a distance similar to that of the diameter of the final damage site (of the order of a few microns). In such cases, the combined generated pressure can be sufficient to facilitate mechanical removal of the overlying material generating mixed-type morphologies. In particular, the appearance of side walls indicates that the failure (rupture and creation of a new surface) was from mechanical stress, while there are also visual indications that significant melting was involved. Such damage morphologies are rarely observed (according to our experience) at near-damage-threshold conditions but can be observed at higher fluences.

Damage can be initiated by extrinsic defects such as microscale nodules or flaws in the coating. We have not investigated these cases in the present work. It is expected, however, that the basic principles presented in this work might be applicable. Pressure- and heat-related effects will govern the material response along with field intensification, initiating damage mechanisms similar to that of type-I damage sites. Also, we have not considered the mechanisms of damage growth, which can be considerably different.

### Conclusions

This work explores the origins and mechanisms of damage site formation associated with three damage morphologies

observed in SiO<sub>2</sub>/HfO<sub>2</sub> multilayer coatings under laser irradiation at 1053 nm with laser pulses from 600 fs to 100 ps in duration. Type-I damage sites are observed for pulses shorter than about 2.5 ps (under the excitation conditions used in this work) and are governed by pressure-induced mechanical ejection of the overlying material following electric-field-induced plasma formation below the surface. Defect-driven damage initiation (type II and type III) is observed for pulse lengths from 2.5 ps to 100 ps. Type-II damage is initiated by defects of the order of 100 nm or less in diameter at a depth defined by the local electric-field-intensity peak. The initial subsurface explosion remains confined and evolves through melting and eventual venting of the evaporated material on a time scale of the order of 20 ns. Type-III damage is associated with the release of material overlying a precursor defect located at depths of less than  $\approx$ 150 nm and shows no correlation with the local electric-field intensity.

#### ACKNOWLEDGMENT

This material is based upon work supported by the Department of Energy National Nuclear Security Administration under Award Number DE-NA0001944, the University of Rochester, and the New York State Energy Research and Development Authority.

#### REFERENCES

1. E. Cartlidge, *Science* **359**, 382 (2018).
2. C. Danson *et al.*, *High Power Laser Sci. Eng.* **3**, e3 (2015).
3. L. Gallais, *Proc. SPIE* **9893**, 989305 (2016).
4. A. A. Manenkov, *Proc. SPIE* **53**, 010901 (2014).
5. A. Hervy *et al.*, *Opt. Eng.* **56**, 011001 (2016)
6. K. Mehrotra, J. B. Oliver, and J. C. Lambropoulos, *Appl. Opt.* **54**, 2435 (2015).
7. K. Mehrotra, H. P. Howard, S. D. Jacobs, and J. C. Lambropoulos, *AIP Adv.* **1**, 042179 (2011).
8. J. C. Lambropoulos, M. R. Jolly, C. A. Amsden, S. E. Gilman, M. J. Sinicropi, D. Diakomihalis, and S. D. Jacobs, *J. Appl. Phys.* **66**, 4230 (1989).
9. M. C. Wingert *et al.*, *Semicond. Sci. Technol.* **31**, 113003 (2016).
10. S. Timoshenko and S. Woinowsky-Krieger, *Theory of Plates and Shells*, 2nd ed. (McGraw-Hill, New York, 1987), Sec. 97.
11. B. C. Stuart *et al.*, *J. Opt. Soc. Am. B* **13**, 459 (1996).
12. R. W. Hopper and D. R. Uhlmann, *J. Appl. Phys.* **41**, 4023 (1970).
13. T. H. Walker, A. H. Guenther, and P. Nielsen, *IEEE J. Quantum Electron.* **QE-17**, 2053 (1981).
14. J. Yu *et al.*, *Adv. Cond. Matter Phys.* **2014**, 364627 (2014).
15. R. M. Wood, *Laser-Induced Damage of Optical Materials*, Series in Optics and Optoelectronics (Institute of Physics, Bristol, England, 2003).
16. S. M. Wiederhorn, in *Mechanical and Thermal Properties of Ceramics*, edited by J. B. Wachtman, Jr., NBS Special Publication 303 (National Bureau of Standards, Gaithersburg, MD, 1969), pp. 217–242.
17. M. M. Wood and J. E. Weidlich, *Am. Mineral.* **67**, 1065 (1982).
18. G. Žagar *et al.*, *Scr. Metall.* **112**, 132 (2016).
19. S. G. Demos, R. A. Negres, R. N. Raman, M. D. Feit, K. R. Manes, and A. M. Rubenchik, *Optica* **2**, 765 (2015).

---

## Publications and Conference Presentations

---

### Publications

---

- S.-W. Bahk, C. Dorrer, and J. Bromage, “Chromatic Diversity: A New Approach for Characterizing Spatiotemporal Coupling of Ultrashort Pulses,” *Opt. Express* **26**, 8767 (2018).
- I. A. Begishev, J. Bromage, S. T. Yang, P. S. Datte, S. Patankar, and J. D. Zuegel, “Record Fifth-Harmonic-Generation Efficiency Producing 211 nm, Joule-Level Pulses Using Cesium Lithium Borate,” *Opt. Lett.* **43**, 2462 (2018).
- A. Bose, R. Betti, D. Mangino, K. M. Woo, D. Patel, A. R. Christopherson, V. Gopalaswamy, O. M. Mannion, S. P. Regan, V. N. Goncharov, D. H. Edgell, C. J. Forrest, J. A. Frenje, M. Gatu Johnson, V. Yu. Glebov, I. V. Igumenshchev, J. P. Knauer, F. J. Marshall, P. B. Radha, R. Shah, C. Stoeckl, W. Theobald, T. C. Sangster, D. Shvarts, and E. M. Campbell, “Analysis of Trends in Experimental Observables: Reconstruction of the Implosion Dynamics and Implications for Fusion Yield Extrapolation for Direct-Drive Cryogenic Targets on OMEGA,” *Phys. Plasmas* **25**, 062701 (2018).
- D. Cao, T. R. Boehly, M. C. Gregor, D. N. Polsin, A. K. Davis, P. B. Radha, S. P. Regan, and V. N. Goncharov, “Theoretical Quantification of Shock-Timing Sensitivities for Direct-Drive Inertial Confinement Fusion Implosions on OMEGA,” *Phys. Plasmas* **25**, 052705 (2018).
- L. Ceurvorst, A. Savin, N. Ratan, M. F. Kasim, J. Sadler, P. A. Norreys, H. Habara, K. A. Tanaka, S. Zhang, M. S. Wei, S. Ivancic, D. H. Froula, and W. Theobald, “Channel Optimization of High-Intensity Laser Beams in Millimeter-Scale Plasmas,” *Phys. Rev. E* **97**, 043208 (2018).
- J. R. Davies, R. E. Bahr, D. H. Barnak, R. Betti, M. J. Bonino, E. M. Campbell, E. C. Hansen, D. R. Harding, J. L. Peebles, A. B. Sefkow, W. Seka, P.-Y. Chang, M. Geissel, and A. J. Harvey-Thompson, “Laser Entrance Window Transmission and Reflection Measurements for Preheating in Magnetized Liner Inertial Fusion,” *Phys. Plasmas* **25**, 062704 (2018).
- J. A. Fooks, L. C. Carlson, P. Fitzsimmons, E. Giraldez, D. N. Kaczala, M. Wei, N. Alexander, M. P. Farrell, J. Betcher, A. Harvey-Thompson, and T. Nagayama, “Evolution of Magnetized Liner Inertial Fusion (MagLIF) Targets,” *Fusion Sci. Technol.* **73**, 423 (2018).
- C. J. Forrest, J. P. Knauer, W. U. Schroeder, V. Yu. Glebov, P. B. Radha, S. P. Regan, T. C. Sangster, M. Sickles, C. Stoeckl, and J. Szczepanski, “Nuclear Science Experiments with a Bright Neutron Source from Fusion Reactions on the Omega Laser System,” *Nuclear Instrum. Methods Phys. Res. A* **888**, 169 (2018).
- D. E. Frantanduono, M. Millot, R. G. Kraus, D. K. Spaulding, G. W. Collins, P. M. Celliers, and J. H. Eggert, “Thermodynamic Properties of MgSiO<sub>3</sub> at Super-Earth Mantle Conditions,” *Phys. Rev. B* **97**, 214105 (2018).
- D. H. Froula, D. Turnbull, A. S. Davies, T. J. Kessler, D. Haberberger, J. P. Palastro, S.-W. Bahk, I. A. Begishev, R. Boni, S. Bucht, J. Katz, and J. L. Shaw, “Spatiotemporal Control of Laser Intensity,” *Nature Photon.* **12**, 262 (2018).
- M. Gatu Johnson, D. T. Casey, M. Hohenberger, A. B. Zylstra, A. Bacher, C. R. Brune, R. M. Bionta, R. S. Craxton, C. L. Ellison, M. Farrell, J. A. Frenje, W. Garbett, E. M. Garcia, G. P. Grim, E. Hartouni, R. Hatarik, H. W. Herrmann, M. Hohensee, D. M. Holunga, M. Hoppe, M. Jackson, N. Kabadi, S. F. Khan, J. D. Kilkenny, T. R. Kohut, B. Lahmann, H. P. Le, C. K. Li, L. Masse, P. W. McKenty, D. P. McNabb, A. Nikroo, T. G. Parham, C. E. Parker, R. D. Petrasso, J. Pino, B. Remington, N. G. Rice, H. G. Rinderknecht, M. J. Rosenberg, J. Sanchez, D. B. Sayre, M. E. Schoff, C. M. Shulberg, F. H. Séguin, H. Sio, Z. B. Walters, and H. D. Whitley, “Optimization of a High-Yield, Low-Areal-Density Fusion Product Source at the National Ignition Facility with Applications in Nucleosynthesis Experiments,” *Phys. Plasmas* **25**, 056303 (2018).
- E. C. Hansen, D. H. Barnak, R. Betti, E. M. Campbell, P.-Y. Chang, J. R. Davies, V. Yu. Glebov, J. P. Knauer, J. Peebles,

S. P. Regan, and A. B. Sefkow, “Measuring Implosion Velocities in Experiments and Simulations of Laser-Driven Cylindrical Implosions on the OMEGA Laser,” *Plasma Phys. Control Fusion* **60**, 054014 (2018).

D. R. Harding, J. Ulreich, M. D. Wittman, R. Chapman, C. Taylor, R. Taylor, N. P. Redden, J. C. Lambropoulos, R. Q. Gram, M. J. Bonino, and D. W. Turner, “Requirements and Capabilities for Fielding Cryogenic DT-Containing Fill-Tube Targets for Direct-Drive Experiments on OMEGA,” *Fusion Sci. Technol.* **73**, 324 (2018).

S. X. Hu, L. A. Collins, T. R. Boehly, Y. H. Ding, P. B. Radha, V. N. Goncharov, V. V. Karasiev, G. W. Collins, S. P. Regan, and E. M. Campbell, “A Review on *Ab-Initio* Studies of Static, Transport, and Optical Properties of Polystyrene Under Extreme Conditions for Inertial Confinement Fusion Applications,” *Phys. Plasmas* **25**, 056306 (2018).

S. Le Pape, L. F. Berzak Hopkins, L. Divol, A. Pak, E. L. Dewald, S. Bhandarkar, L. R. Benedetti, T. Bunn, J. Biener, J. Crippen, D. Casey, D. Edgell, D. N. Fittinghoff, M. Gatu-Johnson, C. Goyon, S. Haan, R. Hatarik, M. Havre, D. D-M. Ho, N. Izumi, J. Jaquez, S. F. Khan, G. A. Kyrala, T. Ma, A. J. Mackinnon, A. G. MacPhee, B. J. MacGowan, N. B. Meezan, J. Milovich, M. Millot, P. Michel, S. R. Nagel, A. Nikroo, P. Patel, J. Ralph, J. S. Ross, N. G. Rice, D. Strozzi, M. Stadermann, P. Volegov, C. Yeamans, C. Weber, C. Wild, D. Callahan, and O. A. Hurricane, “Fusion Energy Output Greater than the Kinetic Energy of an Imploding Shell at the National Ignition Facility,” *Phys. Rev. Lett.* **120**, 245003 (2018).

J. A. Marozas, M. Hohenberger, M. J. Rosenberg, D. Turnbull, T. J. B. Collins, P. B. Radha, P. W. McKenty, J. D. Zuegel, F. J. Marshall, S. P. Regan, T. C. Sangster, W. Seka, E. M. Campbell, V. N. Goncharov, M. W. Bowers, J.-M. G. Di Nicola, G. Erbert, B. J. MacGowan, L. J. Pelz, J. Moody, and S. T. Yang, “Wavelength-Detuning Cross-Beam Energy Transfer Mitigation Scheme for Direct Drive: Modeling and Evidence from National Ignition Facility Implosions,” *Phys. Plasmas* **25**, 056314 (2018) (invited).

S. A. Muller, D. N. Kaczala, H. M. Abu-Shawareb, E. L. Alfonso, L. C. Carlson, M. Mauldin, P. Fitzsimmons, D. Lamb, P. Tzeferacos, L. Chen, G. Gregori, A. Rigby, A. Bott, T. G. White, D. Froula, and J. Katz, “Evolution of the Design and Fabrication of Astrophysics Targets for Turbulent Dynamo (TDYNO) Experiments on OMEGA,” *Fusion Sci. Technol.* **73**, 434 (2018).

J. B. Oliver, S. MacNally, C. Smith, B. N. Hoffman, J. Spaulding, J. Foster, S. Papernov, and T. J. Kessler, “Fabrication of a Glancing-Angle-Deposited Distributed Polarization Rotator for Ultraviolet Applications,” *Proc. SPIE* **10691**, 106911C (2018).

S. Papernov, M. D. Brunzman, J. B. Oliver, B. N. Hoffman, A. A. Kozlov, S. G. Demos, A. Shvydky, F. H. M. Cavalcante, L. Yang, C. S. Menoni, B. Roshanzadeh, S. T. P. Boyd, L. A. Emmert, and W. Rudolph, “Optical Properties of Oxygen Vacancies in HfO<sub>2</sub> Thin Films Studied by Absorption and Luminescence Spectroscopy,” *Opt. Express* **26**, 17,608 (2018).

M. D. Sharpe, C. Fagan, W. T. Shmayda, and W. U. Schröder, “Partitioning of Tritium Between Surface and Bulk of 316 Stainless Steel at Room Temperature,” *Fusion Eng. Des.* **130**, 76 (2018).

R. F. Smith, D. E. Fratanduono, D. G. Braun, T. S. Duffy, J. K. Wicks, P. M. Celliers, S. J. Ali, A. Fernandez-Pañella, R. G. Kraus, D. C. Swift, G. W. Collins, and J. H. Eggert, “Equation of State of Iron Under Core Conditions of Large Rocky Exoplanets,” *Nat. Astron.* **2**, 452 (2018).

C. R. Stillman, P. M. Nilson, A. B. Sefkow, S. T. Ivancic, C. Mileham, I. A. Begishev, and D. H. Froula, “Energy Transfer Dynamics in Strongly Inhomogeneous Hot-Dense-Matter Systems,” *Phys. Rev. E* **97**, 063208 (2018).

M. Stoeckl, and A. A. Solodov, “Readout Models for BaFBr<sub>0.85</sub>I<sub>0.15</sub>:Eu Image Plates,” *Rev. Sci. Instrum.* **89**, 063101 (2018).

J. Trela, W. Theobald, K. S. Anderson, D. Batani, R. Betti, A. Casner, J. A. Delettrez, J. A. Frenje, V. Yu. Glebov, X. Ribeyre, A. A. Solodov, M. Stoeckl, and C. Stoeckl, “The Control of Hot-Electron Preheat in Shock-Ignition Implosions,” *Phys. Plasmas* **25**, 052707 (2018).

D. Turnbull, A. Colaïtis, R. K. Follett, J. P. Palastro, D. H. Froula, P. Michel, C. Goyon, T. Chapman, L. Divol, G. E. Kemp, D. Mariscal, S. Patankar, B. B. Pollock, J. S. Ross, J. D. Moody, E. R. Tubman, and N. C. Woolsey, “Cross-Beam Energy Transfer: Polarization Effects and Evidence of Saturation,” *Plasma Phys. Control. Fusion* **60**, 054017 (2018).

D. Turnbull, P. Franke, J. Katz, J. P. Palastro, I. A. Begishev, R. Boni, J. Bromage, A. L. Milder, J. L. Shaw, and D. H. Froula, “Ionization Waves of Arbitrary Velocity,” *Phys. Rev. Lett.* **120**, 225001 (2018).

P. Tzeferacos, A. Rigby, A. F. A. Bott, A. R. Bell, R. Bingham, A. Casner, F. Cattaneo, E. M. Churazov, J. Emig, F. Fiuza, C. B. Forest, J. Foster, C. Graziani, J. Katz, M. Koenig, C.-K. Li, J. Meinecke, R. Petrasso, H.-S. Park, B. A. Remington, J. S. Ross, D. Ryu, D. Ryutov, T. G. White, B. Reville, F. Miniati, A. A. Schekochihin, D. Q. Lamb, D. H. Froula, and G. Gregori, "Laboratory Evidence of Dynamo Amplification of Magnetic Fields in a Turbulent Plasma," *Nat. Commun.* **9**, 591 (2018).

F. Weilacher, P. B. Radha, and C. Forrest, "Three-Dimensional Modeling of the Neutron Spectrum to Infer Plasma Conditions in Cryogenic Inertial Confinement Fusion Implosions," *Phys. Plasmas* **25**, 042704 (2018).

M. D. Wittman, M. J. Bonino, D. H. Edgell, C. Fella, D. R. Harding, and J. Sanchez, "Effect of Tritium-Induced Damage on Plastic Targets from High-Density DT Permeation," *Fusion Sci. Technol.* **73**, 315 (2018).

K. M. Woo, R. Betti, D. Shvarts, A. Bose, D. Patel, R. Yan, P.-Y. Chang, O. M. Mannion, R. Epstein, J. A. Delettrez, M. Charissis, K. S. Anderson, P. B. Radha, A. Shvydky, I. V. Igumenshchev, V. Gopalaswamy, A. R. Christopherson, J. Sanz, and H. Aluie, "Effects of Residual Kinetic Energy on Yield Degradation and Ion Temperature Asymmetries in Inertial Confinement Fusion Implosions," *Phys. Plasmas* **25**, 052704 (2018).

M. Zaghoo, "Dynamic Conductivity and Partial Ionization in Dense Fluid Hydrogen," *Phys. Rev. E* **97**, 043205 (2018).

D. Zhao and H. Aluie, "Inviscid Criterion for Decomposing Scales," *Phys. Rev. Fluids* **3**, 054603 (2018).

A. B. Zylstra, N. M. Hoffman, H. W. Herrmann, M. J. Schmitt, Y. H. Kim, K. Meaney, A. Leatherland, S. Gales, C. Forrest, V. Yu. Glebov, M. Schoff, M. Hoppe, and N. Ravelo, "Diffusion-Dominated Mixing in Moderate Convergence Implosions," *Phys. Rev. E* **97**, 061201(R) (2018).

### Forthcoming Publications

F. Albert, N. Lemos, J. L. Shaw, P. M. King, B. B. Pollock, C. Goyon, W. Schumaker, A. M. Saunders, K. A. Marsh, A. Pak, J. E. Ralph, J. L. Martins, L. D. Amorim, R. W. Falcone, S. H. Glenzer, J. D. Moody, and C. Joshi, "Betatron X-Ray Radiation in the Self-Modulated Laser Wakefield Acceleration Regime: Prospects for a Novel Probe at Large Scale Laser Facilities," to be published in *Nuclear Fusion*.

P. M. Celliers, M. Millot, S. Brygoo, R. S. McWilliams, D. E. Fratanduono, J. R. Rygg, A. F. Goncharov, P. Loubeyre, J. H. Eggert, J. L. Peterson, N. B. Meezan, S. Le Pape, G. W. Collins, R. Jeanloz, and R. J. Hemley, "Insulator-Metal Transition in Dense Fluid Deuterium," to be published in *Science*.

A. R. Christopherson, R. Betti, J. Howard, K. M. Woo, A. Bose, E. M. Campbell and V. Gopalaswamy, "Theory of Alpha Heating in Inertial Fusion: Alpha-Heating Metrics and the Onset of the Burning-Plasma Regime," to be published in *Physics of Plasmas*.

A. Colaitis, J.-E. Ducret, M. Le Pennec, X. Ribeyre, and S. Turck-Chièze, "Towards a Novel Stellar Opacity Measurement Scheme Using Stability Properties of Double Ablation Front Structures," to be published in *Physics of Plasmas*.

T. J. B. Collins, and J. A. Marozas, "Mitigation of Cross-Beam Energy Transfer in Ignition-Scale Polar-Direct-Drive Target

Designs for the National Ignition Facility," to be published in *Physics of Plasmas*.

C. Dorrer and R. J. Brown, "A Stable, Low-Repetition-Rate Time-Lens Picosecond Seed Source," to be published in *IEEE Photonics Technology Letters*.

C. Dorrer, A. Kalb, P. Fiala, S.-W. Bahk, A. Sharma, and K. Gibney, "Investigation of an Apodized Imaged Hartmann Wavefront Sensor," to be published in *Applied Optics*.

D. H. Edgell, J. Katz, D. P. Turnbull, and D. H. Froula, "Unabsorbed Light Beamlets for Diagnosing Cross-Beam Energy Transfer," to be published in *Review of Scientific Instruments*.

C. L. Ellison, H. D. Whitley, C. R. D. Brown, S. R. Copeland, W. J. Garbett, H. P. Le, M. B. Schneider, Z. B. Walters, H. Chen, J. I. Castor, R. S. Craxton, M. Gatu Johnson, E. M. Garcia, F. R. Graziani, G. E. Kemp, C. M. Krauland, P. W. McKenty, B. Lahmann, J. E. Pino, M. S. Rubery, H. A. Scott, R. Shepherd, and H. Sio, "Development and Modeling of a Polar-Direct-Drive Exploding Pusher Platform at the National Ignition Facility," to be published in *Physics of Plasmas*.

M. Gatu Johnson, C. J. Forrest, D. B. Sayre, A. Bacher, J.-L. Bourgade, C. R. Brune, J. A. Caggiano, D. T. Casey, J. A.

Frenje, V. Yu. Glebov, G. M. Hale, R. Hatarik, H. W. Herrmann, R. Janezic, Y. H. Kim, J. P. Knauer, O. Landoas, D. P. McNabb, M. W. Paris, R. D. Petrasso, J. E. Pino, S. Quaglioni, B. Rosse, J. Sanchez, T. C. Sangster, H. Sio, W. Shmayda, C. Stoeckl, I. Thompson, and A. B. Zylstra, "Experimental Evidence of a Variant Neutron Spectrum from the  $T(t,2n)\alpha$  Reaction at Center-of-Mass Energies in the Range of 16–50 keV," to be published in *Physical Review Letters*.

S. M. Gracewski, S. Boylan, J. C. Lambropoulos, J. B. Oliver, T. J. Kessler, and S. G. Demos, "Simulation of Internal Stress Waves Generated by Laser-Induced Damage in Multilayer Dielectric Gratings," to be published in *Optics Express*.

W. Grimble, F. J. Marshall, and E. Lambrides, "Measurement of Cryogenic Target Position and Implosion Core Offsets on OMEGA," to be published in *Physics of Plasmas*.

A. M. Hansen, D. Haberberger, J. Katz, D. Mastro Simone, R. K. Follett, and D. H. Froula, "Supersonic Gas-Jet Characterization with Interferometry and Thomson Scattering on the OMEGA Laser System," to be published in *Review of Scientific Instruments*.

A. Howard, D. Haberberger, R. Boni, R. Brown, and D. H. Froula, "Implementation of a Wollaston Interferometry Diagnostic on OMEGA EP," to be published in *Review of Scientific Instruments*.

S. X. Hu, V. N. Goncharov, P. B. Radha, S. P. Regan, and E. M. Campbell, "Microphysics Studies for Direct-Drive Inertial Confinement Fusion," to be published in *Nuclear Fusion*.

S. X. Hu, W. Theobald, P. B. Radha, J. L. Peebles, S. P. Regan, A. Nikroo, M. J. Bonino, D. R. Harding, V. N. Goncharov, N. Petta, T. C. Sangster, and E. M. Campbell, "Mitigating Laser-Imprint Effects in Direct-Drive Inertial Confinement Fusion Implosions with an Above-Critical-Density Foam Layer," to be published in *Physics of Plasmas*.

C. Z. R. Huang, R. W. Wood, and S. G. Demos, "Adaptation of Microscopy with Ultraviolet Surface Excitation for Enhancing STEM and Undergraduate Education," to be published in the *Journal of Biomedical Optics*.

E. V. Ludeña, E. X. Salazar, M. H. Cornejo, D. E. Arroyo, and V. V. Karasiev, "The Liu–Parr Power Series Expansion of the

Pauli Kinetic Energy Functional with the Incorporation of the Shell-Inducing Traits: Atoms," to be published in the *International Journal of Quantum Chemistry*.

K. Luo, V. V. Karasiev, and S. B. Trickey, "A Simple Generalized Gradient Approximation for the Noninteracting Kinetic Energy Density Functional," to be published in *Physical Review B*.

O. M. Mannion, V. Yu. Glebov, C. J. Forrest, V. N. Goncharov, J. P. Knauer, S. P. Regan, T. C. Sangster, C. Stoeckl, and M. Gatu Johnson, "Calibration of a Neutron Time-of-Flight Detector with a Rapid Instrument Response Function for Measurements of Bulk Fluid Motion on OMEGA," to be published in *Review of Scientific Instruments*.

J. Matteucci, W. Fox, A. Bhattacharjee, D. B. Schaeffer, C. Moissard, K. Germaschewski, G. Fiksel, and S. X. Hu, "Biermann-Battery–Mediated Magnetic Reconnection in 3-D Colliding Plasmas," to be published in *Physical Review Letters*.

A. Rigby, J. Katz, A. F. A. Bott, T. G. White, P. Tzeferacos, D. Q. Lamb, D. H. Froula, and G. Gregori, "Implementation of a Faraday Rotation Diagnostic at the OMEGA Laser Facility," to be published in *High Power Laser Science and Engineering*.

R. Sobolewski, "Optical Sensors," to be published in the *Handbook of Superconducting Materials*.

C. Stoeckl, T. Filkins, R. Jungquist, C. Mileham, N. R. Pereira, S. P. Regan, M. J. Shoup III, and W. Theobald, "Characterization of Shaped Bragg Crystal Assemblies for Narrowband X-Ray Imaging," to be published in *Review of Scientific Instruments*.

R. Xin and J. D. Zuegel, "Chirped-Pulse–Amplification Seed Source Through Direct Phase Modulation," to be published in *Optics Express*.

R. P. Young, C. C. Kuranz, R. P. Drake, D. H. Froula, J. S. Ross, and S. Klein, "Observation of Collisionless-to-Collisional Transition in Colliding Plasma Jets with Optical Thomson Scattering," to be published in *Physics of Plasmas*.

M. Zaghoo and G. W. Collins, "Size and Strength of Self-Excited Dynamos in Jupiter-Like Extrasolar Planets," to be published in *Astrophysical Journal*.

---

**Conference Presentations**


---

J. Bromage, S.-W. Bahk, I. A. Begishev, C. Dorrer, M. J. Guardalben, B. N. Hoffman, J. B. Oliver, R. G. Roides, E. M. Schiesser, M. J. Shoup III, M. Spilatro, B. Webb, D. Weiner, and J. D. Zuegel, “Technology Development for Ultra-Intense All-OPCPA Systems,” presented at the 3rd International Symposium on High Power Laser Science and Engineering, Suzhou, China, 9–12 April 2018.

---

M. Singh, J. Cady, Y. Akbas, G. Chen, R. Sobolewski, and O. Mukhanov, “Superconducting Single-Photon Detectors as Smart Sensors,” presented at CEIS 2018, Rochester, NY, 12 April 2018.

---

The following presentations were made at the March for Science, Rochester, NY, 14 April 2018:

N. Bose, “Compensation for Self-Focusing on OMEGA EP by Use of Frequency Conversion of Light.”

R. S. Craxton, “University of Rochester, Laboratory for Laser Energetics.”

Y. Yang and R. S. Craxton, “Improving the Uniformity of *Revolver* Designs for the National Ignition Facility.”

---

The following presentations were made at the 22nd Topical Conference on High Temperature Plasma Diagnostics, San Diego, CA, 16–19 April 2018:

D. H. Edgell, J. Katz, D. Turnbull, and D. H. Froula, “Unabsorbed Light Beamlets for Diagnosing Cross-Beam Energy Transfer.”

V. Yu. Glebov, M. J. Eckart, C. J. Forrest, G. P. Grim, E. P. Hartouni, R. Hatarik, J. P. Knauer, A. S. Moore, S. P. Regan, T. C. Sangster, D. J. Schlossberg, and C. Stoeckl, “Testing a Cherenkov Neutron Time-of-Flight Detector on OMEGA.”

A. Hansen, D. Haberberger, J. Katz, R. K. Follett, and D. H. Froula, “Supersonic Gas-Jet Characterization with Interferometry and Thomson Scattering on the OMEGA Laser System.”

A. Howard, D. Haberberger, R. Boni, R. Brown, and D. H. Froula, “Implementation of a Wollaston Interferometry Diagnostic on OMEGA EP.”

J. Katz, R. Boni, A. Davies, and D. H. Froula, “A High-Throughput, Pulse-Front-Tilt-Compensated Streaked Spectrometer for Picosecond Optical Thomson Scattering.”

O. M. Mannion, C. J. Forrest, V. Yu. Glebov, V. N. Goncharov, J. P. Knauer, S. P. Regan, T. C. Sangster, C. Stoeckl, and M. Gatu Johnson, “Measurements of Bulk-Fluid Motion In Direct-Drive Implosions.”

A. L. Milder and D. H. Froula, “Measuring Electron Distribution Functions Using Collective Thomson Scattering.”

P. M. Nilson, F. Ehrne, C. Taylor, C. Mileham, D. Mastrosimone, R. K. Jungquist, R. Boni, J. Hassett, C. R. Stillman, S. T. Ivancic, D. J. Lonobile, R. W. Kidder, M. J. Shoup III, A. A. Solodov, A. B. Sefkow, C. Stoeckl, W. Theobald, D. H. Froula, K. W. Hill, L. Gao, M. Bitter, P. Efthimion, and D. D. Meyerhofer, “High-Resolving-Power, Streaked X-Ray Spectroscopy on the OMEGA EP Laser System.”

R. C. Shah, D. Cao, R. Epstein, S. P. Regan, W. Theobald, B. Kraus, L. Gao, K. Hill, B. Stratton, P. Efthimion, and B. Bachmann, “Multichannel X-Ray Hot-Spot Imager Operating in the 5- to 3-KeV Range on OMEGA.”

C. Stoeckl, T. Filkins, R. K. Jungquist, C. Mileham, S. P. Regan, M. J. Shoup III, and W. Theobald, “Characterization of Shaped Bragg Crystal Assemblies for Narrowband X-Ray Imaging.”

W. Theobald, C. Sorce, M. Bedzyk, S. T. Ivancic, F. J. Marshall, C. Stoeckl, R. Shah, M. Lawrie, S. P. Regan, T. C. Sangster, E. M. Campbell, T. Hilsabeck, K. Engelhorn, J. D. Kilkenny, D. Morris, M. Chung, J. D. Hares, A. K. L. Dymoke-Bradshaw, P. Bell, J. Celeste, A. Carpenter, M. Dayton, D. K. Bradley, M. C. Jackson, L. Pickworth, S. R. Nagel, G. Rochau, J. Porter, M. Sanchez, L. Claus, G. Robertson, and Q. Looker, “The Single Line-of-Sight, Time-Resolved X-Ray Imager Diagnostic on OMEGA.”

The following presentations were made at the Meeting on Magnetic Fields in Laser Plasmas, Rochester, NY, 23–24 April 2018:

D. H. Barnak, R. Betti, P.-Y. Chang, J. R. Davies, V. Yu. Glebov, E. C. Hansen, J. P. Knauer, J. Peebles, S. P. Regan, R. Epstein, A. B. Sefkow, E. M. Campbell, K. J. Peterson, D. B. Sinars, and S. A. Slutz, “Laser-Driven Magnetized Liner Inertial Fusion on OMEGA.”

J. Peebles, J. R. Davies, D. H. Barnak, G. Brent, D. Mastro Simone, D. W. Jacobs-Perkins, G. Fiksel, M. J. Shoup III, T. Lewis, G. Gates, P. A. Gourdain, R. Shapovalov, R. Moshier, T. Burgett, and R. Betti, “Current Capabilities of the MIFEDS System.”

J. Peebles, J. R. Davies, D. H. Barnak, A. B. Sefkow, P. A. Gourdain, R. Betti, and A. Arefiev, “Laser Driven Coils on OMEGA EP.”

---

S. G. Demos, A. A. Kozlov, K. Kafka, J. B. Oliver, S. Papernov, B. Hoffman, T. J. Kessler, S. M. Gracewski, and J. C. Lambropoulos, “Mechanisms of Laser Damage in Optical Components for Petawatt-Class Laser Systems,” presented at Pacific Rim Laser Damage 2018, Yokohama, Japan, 24–27 April 2018.

---

The following presentations were made at the Omega Laser Facility Users Group Workshop, Rochester, NY, 25–27 April 2018:

A. Bose, R. Betti, D. Mangino, K. M. Woo, D. Patel, A. R. Christopherson, V. Gopalaswamy, O. M. Mannion, S. P. Regan, V. N. Goncharov, C. J. Forrest, J. A. Frenje, M. Gatu Johnson, V. Yu. Glebov, J. P. Knauer, F. J. Marshall, R. Nora, P. B. Radha, R. C. Shah, C. Stoeckl, W. Theobald, T. C. Sangster, D. Shvarts, and E. M. Campbell, “Analysis of Trends in Experimental Observables for Direct-Drive Cryogenic Implosions on OMEGA, Reconstruction of the Implosion Core and Extrapolation to National Ignition Facility Energy.”

N. R. Bose, “Compensation for Self-Focusing on OMEGA EP by Use of Frequency Conversion.”

R. Brown, C. Dorrer, and E. M. Hill, “High-Stability Sub-10-ps Fourth-Harmonic Probe Seed Source.”

A. Consentino, C. Dorrer, R. Cuffney, I. A. Begishev, E. M. Hill, B. E. Kruschwitz, and A. Szydlowski, “A New Spectrally Tunable Narrowband Front-End Source for Cross-Beam Energy Transfer Mitigation Experiments.”

M. C. Cornelius, T. W. Walker, and G. A. Brent, “Characterization and Detection of the Deterioration of Electrical Connectors in a Flash-Lamp System.”

B. E. Kruschwitz, M. Barczys, A. Consentino, C. Dorrer, M. J. Guardalben, E. M. Hill, J. Kwiatkowski, D. Nelson, J. C. Puth, D. Turnbull, and L. J. Waxer, “Development of a Tunable UV Capability for Cross-Beam Energy Transfer Mitigation Studies in the OMEGA Target Chamber.”

D. Mastro Simone, G. Weselak, R. Mosier, C. Sorce, D. Haberberger, D. H. Froula, J. Katz, and A. Hansen, “Fielding a Gas Jet on OMEGA and OMEGA EP.”

S. F. B. Morse, “Omega Facility OLUG 2018 Update: Progress on Recommendations and Items of General Interest.”

G. Pien, W. J. Armstrong, and M. Krieger, “Use of CAD for Real-Time Target-Position Guidance and Geometry Validation.”

S. Sampat, J. H. Kelly, T. Z. Kosc, A. L. Rigatti, J. Kwiatkowski, W. R. Donaldson, M. H. Romanofsky, L. J. Waxer, R. Dean, and R. Moshier, “Power Balance on a Multibeam Laser.”

L. J. Waxer, M. Heimbueger, J. H. Kelly, S. F. B. Morse, D. Nelson, D. Weiner, and G. Weselak, “On-Shot Focal-Spot Characterization in the OMEGA Target Chamber.”

---

The following presentations were made at the 3rd International Conference on Matter and Radiation at Extremes, Qingdao, China, 6–11 May 2018:

E. M. Campbell, “Laser–Plasma Interaction Physics and Direct Drive: Challenges and Path Forward.”

J. A. Marozas, M. J. Rosenberg, D. Turnbull, T. J. B. Collins, D. Cao, P. W. McKenty, P. B. Radha, T. C. Sangster, S. P. Regan, V. N. Goncharov, E. M. Campbell, M. W. Bowers, J.-M. G. DiNicola, G. Erbert, M. Hohenberger, B. J. MacGowan, J. D. Moody, L. J. Pelz, and S. T. Yang, “Wavelength Detuning  $\Delta\lambda_0$

Cross-Beam Energy Transfer Mitigation for Polar Direct Drive on Shen Guang (SG)-III.”

S. P. Regan, V. N. Goncharov, T. C. Sangster, E. M. Campbell, R. Betti, T. R. Boehly, M. J. Bonino, A. Bose, D. Cao, R. Chapman, T. J. B. Collins, R. S. Craxton, A. K. Davis, J. A. Delettrez, D. H. Edgell, R. Epstein, C. J. Forrest, D. H. Froula, V. Yu. Glebov, D. R. Harding, S. X. Hu, I. V. Igumenshchev, D. W. Jacobs-Perkins, R. T. Janezic, J. H. Kelly, T. J. Kessler, J. P. Knauer, T. Z. Kosc, S. J. Loucks, J. A. Marozas, F. J. Marshall, R. L. McCrory, P. W. McKenty, D. T. Michel, J. F. Myatt, P. B. Radha, M. J. Rosenberg, W. Seka, R. W. Short, W. T. Shmayda, M. J. Shoup III, A. Shvydky, A. A. Solodov, C. Sorce, C. Stoeckl, C. Taylor, R. Taylor, W. Theobald, D. Turnbull, J. Ulreich, M. D. Wittman, K. M. Woo, J. D. Zuegel, M. A. Barrios, T. Chapman, C. Gibson, C. Goyon, M. Hohenberger, P. Michel, J. D. Moody, J. E. Ralph, J. W. Bates, M. Karasik, S. P. Obenschain, A. J. Schmitt, T. Bernat, J. Hund, N. Petta, M. Farrell, A. Greenwood, H. Huang, M. Schoff, W. Sweet, J. A. Frenje, M. Gatu Johnson, R. D. Petrasso, and M. J. Schmitt, “The U.S. National Direct-Drive Inertial Confinement Fusion Program.”

The following presentations were made at the 12th Department of Energy Laser Safety Officer Workshop, Rochester, NY, 8–10 May 2018:

J. Bromage, “Laser Science and Technology at LLE.”

G. W. Collins, “LLE: A Unique University-Based Research Center of Scale Supporting National Security and Extreme Science.”

K. R. P. Kafka, “Introduction to Optics.”

J. C. Puth, “Laser Safety at the Omega Laser Facilities.”

The following presentations were made at CLEO 2018, San Jose, CA, 13–18 May 2018:

S.-W. Bahk, B. E. Kruschwitz, A. L. Rigatti, J. B. Oliver, and J. Bromage, “Variable Astigmatism Corrector for High-Power Lasers.”

C. Dorrer, and S.-W. Bahk, “Characterization of Spatiotemporal Coupling with a Hyperspectral Hartmann Wavefront Sensor.”

C. Dorrer and R. J. Brown, “High-Stability Time-Lens-Based Picosecond Seed Source.”

C. Dorrer, A. Consentino, R. Cuffney, I. A. Begishev, E. M. Hill, and J. Bromage, “Spectrally Tunable, Temporally Shaped Parametric Front End to Seed High-Energy Laser Systems.”

C. Dorrer and J. Qiao, “Improved Spatially Dithered Beam Shapers Using Direct Binary Search.”

B. Webb, M. J. Guardalben, C. Dorrer, S. Bucht, and J. Bromage, “Pulse-Compressor Grating Alignment Tolerances for Varied Geometries and Bandwidths.”

J. B. Oliver, S. MacNally, C. Smith, B. N. Hoffman, J. Spaulding, J. Foster, S. Papernov, and T. J. Kessler, “Fabrication of a Glancing-Angle-Deposited Distributed Polarization Rotator for Ultraviolet Applications,” presented at SPIE Advances in Optical Thin Films, Frankfurt, Germany, 14–17 May 2018.

The following presentations were made at the Tritium Focus Group Meeting, Oak Ridge, TN, 15–17 May 2018:

D. Bassler, W. T. Shmayda, and W. U. Schröder, “The Effect of Surface Chemistry of ALD Films on Tritium Retention in Stainless Steel.”

C. Fagan, M. Sharpe, W. T. Shmayda, and W. U. Schröder, “Tritium Retention in Hexavalent Chromate-Conversion-Coated Aluminum Alloy.”

A. Schwemmlin, W. U. Schröder, and W. T. Shmayda, “Using the T-LIANS Platform to Explore Nuclear Reactions.”

M. Sharpe, C. Fagan, and W. T. Shmayda, “Distribution of Tritium in the Near Surface of Stainless-Steel 316.”

W. T. Shmayda and N. Redden, “Assaying Hydrogen Isotopes with Gas Chromatography.”

E. M. Campbell, "LLE: A Unique University-Based Research Center of Scale Supporting National Security and Extreme Science," presented at DOE OFES, Washington, DC, 30 May 2018.

---

C. J. Forrest, V. Yu. Glebov, J. P. Knauer, P. B. Radha, J. R. Rygg, W. U. Schröder, C. Stoeckl, J. A. Frenje, M. Gatu Johnson, F. H. Séguin, R. D. Petrasso, H. Sio, D. T. Casey, C. Cerjan, D. Dearborn, M. J. Edwards, G. Grim, R. Hatarik, S. P. Hatchett, O. S. Jones, O. L. Landen, A. J. Mackinnon, D. McNabb, S. Quaglioni, D. Sayre, S. Sepke, P. Springer, I. Thomson, R. E. Tipton, C. Brune, A. Vionov, J. D. Kilkenny, B. Appelbe, A. Crilly, G. Hale, H. W. Herrmann, Y. H. Kim, M. Paris, and A. B. Zylstra, "Nuclear Science Experiments at the University of Rochester's Omega Laser Facility," presented at Triangle University National Laboratory, Durham, NC, 31 May 2018.

---

R. Betti, J. P. Knauer, V. Gopalaswamy, D. Patel, K. M. Woo, A. Bose, N. Luciani, K. S. Anderson, T. J. B. Collins, V. Yu. Glebov, V. N. Goncharov, A. V. Maximov, F. J. Marshall, P. W. McKenty, P. B. Radha, S. P. Regan, T. C. Sangster, C. Stoeckl, and E. M. Campbell, "Progress in Direct-Drive Inertial Fusion," presented at the 19th International Congress on Plasma Physics, Vancouver, Canada, 4–8 June 2018.

---

D. H. Froula, M. Glinsky, P. Michel, J. F. Myatt, J. Weaver, and L. Yin, "Update on the National LPI Workshop," presented at the NNSA Update, Washington, DC, 12 June 2018.

---

E. M. Campbell, "LLE Program in 2019," presented at the ICF Executives Meeting, Washington, DC, 12–13 June 2018.

---

E. M. Campbell, "Overview of Inertial Fusion Energy Concepts Being Developed in the Private Sector," presented at the First IAEA Workshop on Fusion Enterprises, Santa Fe, NM, 13–15 June 2018.

C. R. Stillman, P. M. Nilson, S. T. Ivancic, A. B. Sefkow, C. Mileham, D. J. Nelson, I. A. Begishev, D. H. Froula, I. E. Golovkin, R. A. London, and M. E. Martin, "Ultrafast X-Ray Spectroscopy of Hot-Dense-Matter Systems," presented at the Stewardship Science Fellowship, San Francisco, CA, 18–21 June 2018.

---

S. P. Regan, "Laser-Direct-Drive Inertial Confinement Fusion Research on OMEGA," presented at Extreme Light Infrastructure Nuclear Physics, Bucharest, Romania, 22 June 2018.

---

D. H. Froula, J. S. Ross, B. Pollock, R. K. Follett, R. J. Henchen, A. Davies, A. M. Hansen, A. L. Milder, J. P. Palastro, J. Katz, and R. Boni, "Optical Thomson Scattering in High-Energy-Density Plasmas," presented at the 45th International Conference on Plasma Science, Denver, CO, 24–28 June 2018.

---

S. P. Regan, V. N. Goncharov, T. C. Sangster, E. M. Campbell, R. Betti, K. S. Anderson, J. W. Bates, K. Bauer, T. P. Bernat, S. D. Bhandarkar, T. R. Boehly, M. J. Bonino, A. Bose, D. Cao, T. Chapman, G. W. Collins, T. J. B. Collins, R. S. Craxton, J. A. Delettrez, D. H. Edgell, R. Epstein, M. Farrell, C. J. Forrest, J. A. Frenje, D. H. Froula, M. Gatu Johnson, C. Gibson, V. Gopalaswamy, V. Yu. Glebov, A. Greenwood, D. R. Harding, M. Hohenberger, S. X. Hu, H. Huang, J. Hund, I. V. Igumenshchev, D. W. Jacobs-Perkins, R. T. Janezic, M. Karasik, J. H. Kelly, T. J. Kessler, J. P. Knauer, T. Z. Kosc, J. A. Marozas, F. J. Marshall, P. W. McKenty, D. T. Michel, P. Michel, J. D. Moody, J. F. Myatt, A. Nikroo, S. P. Obenschain, J. P. Palastro, J. L. Peebles, R. D. Petrasso, N. Petta, P. B. Radha, J. E. Ralph, M. J. Rosenberg, S. Sampat, A. J. Schmitt, M. J. Schmitt, M. Schoff, W. Seka, R. Shah, R. W. Short, W. T. Shmayda, M. J. Shoup III, A. Shvydky, A. A. Solodov, C. Sorce, C. Stoeckl, W. Sweet, C. Taylor, R. Taylor, W. Theobald, D. Turnbull, J. Ulreich, M. D. Wittman, K. M. Woo, and J. D. Zuegel, "Laser-Direct-Drive Inertial Confinement Fusion Research on OMEGA," presented at Nuclear Photonics 2018, Brasov, Romania, 24–29 June 2018.

K. R. P. Kafka, "Optical Materials Research for 100-PW-Class Laser Systems," presented at Advanced Materials for Powerful Lasers, Rochester, NY, 25–26 June 2018.

E. M. Campbell, "Inertial Confinement Fusion (ICF) Overview; Status, Plans, and Future Prospects," presented at Laser Precision Microfabrication 2018, Edinburgh, UK, 25–28 June 2018.

---

S.-W. Bahk, and C. Dorrer, "Multispectral Wavefront Sensing for Characterizing Spatiotemporal Coupling in Ultrashort Pulses," presented at Computational Optical Sensing and Imaging, Orlando, FL, 25–28 June 2018.

---

C. Dorrer, B. E. Kruschwitz, S.-W. Bahk, J. Bromage, J. H. Kelly, and V. Bagnoud, "Adaptive Optics and Wavefront Metrology for High-Intensity Laser Systems," presented at Adaptive Optics: Methods, Analysis, and Applications, Orlando, FL, 25–28 June 2018.





